SPHERICAL AND CUBIC NANOPARTICLES: STRUCTURE-PROPERTY RELATIONSHIPS AND ENZYMATIC SYNTHESIS AND DEGRADATION

A Dissertation Presented to

the Faculty of the Department of Chemistry

University of Houston

In Partial Fulfillment

of the Requirements for the Degree

Doctor of Philosophy

By

Arati G. Kolhatkar

May 2014

SPHERICAL AND CUBIC NANOPARTICLES: STRUCTURE-PROPERTY RELATIONSHIPS AND ENZYMATIC SYNTHESIS AND DEGRADATION

_____

Arati G. Kolhatkar

APPROVED:

_____

Dr. T. Randall Lee, Chairman

_____

Dr. Richard C. Willson, Co-Chairman

_____

Dr. Dmitri Litvinov

_____

Dr. Chengzhi Cai

_____

Dr. Ognjen Š. Miljanić

_____

Dr. Shoujun Xu

_____

Dean, College of Natural Sciences and Mathematics

ACKNOWLEDGMENTS

The pursuit of a Ph.D. degree is a journey, not a destination. Although challenging at many points, this journey was made possible and proved very rewarding, thanks to all the folks with whom I interacted during this time. First and foremost, I offer my sincere gratitude to my advisors, Dr. T. Randall Lee and Dr. Richard Willson, for their guidance throughout my research. It has been a privilege to be a part of their groups; their dedication and stellar achievements have propelled me to set high standards in my research.

I would like to also thank my other committee members, Dr. Dmitri Litvinov, Dr. Chengzhi Cai, Dr. Ognjen Š. Miljanić, and Dr. Shoujun Xu, for agreeing to serve on my committee, and for their valuable input. I especially cannot thank Dr. Litvinov enough for his expertise and for our many "magnetic" discussions.

I also offer special thanks to Dr. Andrew C. Jamison for all his help in the last few years; his prompt editorial feedback and very useful comments have been very much appreciated. His kind words and encouragement always provide the extra pillar of support to the Lee group. In the parallel universe of the Willson group, I thoroughly enjoyed my interactions and discussions with Dr. Katerina Kourentzi. I am very grateful to her for her critical review of my 'enzymatic' manuscripts.

I very much appreciate the assistance that I have received from numerous colleagues; the magnetic analyses done by Ivan Nekrashevich, Dr. Yu-Chi Liang, and Dr. Pawilai Chinwangso in Dr. Litvinov's group, and by Dr. Karen Martirosyan's lab at University of Texas at Brownsville, high-resolution TEM done by Dr. Irene Rusakova

and SEM by Dr. Jim Meen – both at the Texas Center of Superconductivity, and the help in interpreting XPS data by Dr. Boris Macarenko at University of Houston. And a special thanks to Dr. Shoujun Xu for graciously allowing me to evaluate my samples using his very recently reported FIRMS technique and to his students, Lashan De Silva and Yi-ting Chen, for doing the measurements.

I am indebted to my colleagues-turned-friends for their support and assistance: Dr. Oussama Zenasni for his help with mechanisms/organic chemistry, Crystal Young for her perfect help and critiques of presentations, Henry Li for being with me on this expedition at the same time and providing "secrets" to make chemistries work, Yi-ting Chen for her FIRMS analysis and discussions, Orawan Khantamat for sharing her "know-how" of nanoshells, and overall both groups for making this a very enjoyable journey.

Most importantly, I thank my family and friends for being there for me. I am blessed to be surrounded by very loving friends throughout this journey. I do not have the words to describe the support of my mother, Alka. She believed in me even at times when I didn't believe in myself. I offer my deepest gratitude to my late father, Prafulla, and late grandparents, Sumati and Narhar, for their love and life-long blessings, and to uncle and aunt, Subhash and Jyoti, and grandparents, Raj and Tara, and for their strong support. Finally, I truly appreciate the love and patience of my husband, Ravi, and kids, Tejas and Rajasi, when I spent countless hours on my homework assignments and laboratory work. Their support meant the world to me. It wasn't easy balancing the pursuit of a Ph.D. degree with kids' piano, basketball, choir, and dance, not to mention other professional commitments - but we did it!

SPHERICAL AND CUBIC NANOPARTICLES: STRUCTURE-PROPERTY RELATIONSHIPS AND ENZYMATIC SYNTHESIS AND DEGRADATION

An Abstract of a Dissertation

Presented to

the Faculty of the Department of Chemistry

University of Houston

In Partial Fulfillment

of the Requirements for the Degree

Doctor of Philosophy

By

Arati G. Kolhatkar

May 2014

ABSTRACT

Defining the influence of the shape of magnetic nanoparticles (MNPs) on their magnetic properties continues to challenge the research community. There exists a small amount of comparative data for MNPs less than 25 nm, but data for larger sizes are sorely lacking. This gap in the available data motivated my pursuit of a comparison of the magnetic properties of larger cubic and spherical Fe_3O_4 MNPs (>100 nm), leading to a conclusion that such comparisons should consider the degree of crystallinity of the MNPs. For MNP applications involving sensing, geometries other than spherical are preferred, where large contact areas and the resulting stronger binding to the sensor platform should lead to enhanced sensitivity. Therefore, I initially focused my research on the synthesis of cubic magnetic FeCo nanocubes with high saturation magnetization. Finally, to functionalize these nanoparticles for use in sensing, it was necessary to coat them with a thin protective layer while retaining their cubic shape. This goal was accomplished by using a silica coating followed by amine functionalization for FeCo nanocubes.

Magnetic biosensing currently employs already-synthesized MNPs and giant magnetoresistive (GMR) sensors. The use of MNP labels in bioassays and diagnostics is attractive because it can overcome concerns associated with optical sensing, which relies on substrate modification to form a product that absorbs, fluoresces, luminesces, or transforms to an insoluble precipitate. The enzyme-mediated synthesis of MNPs is a new concept for magnetic sensing in which the magnetic reporter can be enzymatically synthesized *in situ*. The development of this project also encouraged the pursuit of a diametrically opposite system in which the magnetic component would lose its

magnetism through an enzymatically mediated reduction process. Both approaches show potential for structuring assays that use a magnetic signal that either appears or disappears in the presence of a specific enzyme.

To summarize, my research has focused on two primary goals: (1) the chemical synthesis and functionalization of spherical and cubic MNPs and (2) the enzymatically mediated synthesis or disappearance of MNPs that can be potentially used in a sensing assay.

TABLE OF CONTENTS

LIST OF FIGURES

LIST OF TABLES

LIST OF ABBREVIATIONS, SYMBOLS, AND UNITS

AP	Alkaline Phosphatase
EDS/EDX	Energy-Dispersive X-Ray Spectroscopy
ELISA	Enzyme-Linked Immunosorbent Assay
FIRMS	Force-Induced Remnant Magnetization Spectroscopy
GMR	Giant Magnetoresistive
MNP	Magnetic Nanoparticle
MRI	Magnetic Resonance Imaging
NP	Nanoparticle
SAM	Self-Assembled Monolayer
SAR	Specific Absorption Rate
SEM	Scanning Electron Microscope
SLP	Specific Loss Power
TEM	Transmission Electron Microscope
VSM	Vibrating Sample Magnetometer
XPS	X-Ray Photon Spectroscopy
XRD	X-Ray Diffractometer
bcc	Body-centered cubic
C	Concentration of nanoparticles
FC	Field Cooled
fcc	Face-centered cubic
Hc	Coercivity

K	Anisotropy constant
K'	Shape factor
k_B	Boltzmann constant
Mr	Remanent magnetization
Ms	Saturation magnetization
Ms_b	Magnetization of bulk
O_h	Octahedral sites
ro	Transition point from superparamagnetic to single domain
T_1	Longitudinal spin relaxation times in the presence of nanoparticles
T_1^0	Longitudinal spin relaxation times in pure water
T_2	Transverse spin relaxation times in the presence of nanoparticles
T_2^0	Transverse spin relaxation times in pure water
T_B	Blocking temperature
t_B	Brownian relaxation
Tc	Curie temperature
T_d	Tetrahedral sites
t_N	Neel relaxation
to	Relaxation time of non-interacting MNPs
V	Volume
V_B	Hydrodynamic volume
ZFC	Zero Field Cooled
ν_B	Frequency of heating due to t_B

ν_N	Frequency of heating due to t_N
emu/g	electromagnetic unit/gram
Oe	Oersted
G	Gauss
T	Tesla
mT	milliTesla
pT	picoTesla
nm	nanometer

Chapter 1

Magnetic Nanoparticles: Background and Research Motivation

1.1 Introduction

Magnetic nanoparticles (MNPs) have been extensively studied over the last half century and continue to sustain interest due to their potential use in fields ranging from high-density data storage[1] to biomedical applications.[2,3] The unique properties of MNPs derive from the fact that these nanoscale magnets differ from bulk materials due to their high surface-to-volume ratios. Owing to strong interest in their possible applications, several reviews of MNPs have been published[2,4] including those that focus on sensing,[1,5] drug delivery,[6-8] and hyperthermia.[9] Although there is a plethora of published information, a review that emphasizes the optimization of MNP properties to effectively target specific applications is lacking. The motivation for assembling this chapter was to provide a matrix of parameters to modulate and tune the properties of MNPs for a particular end-use. Recently, there has been substantial progress in the synthesis of MNPs of varying sizes, shapes, compositions, and shell-core designs.[10,11] This review will target the different factors that contribute to the control and optimization of the key magnetic properties of MNPs: saturation magnetization (Ms), coercivity (Hc), blocking temperature (T_B), and relaxation time (t_N and t_B).

MNPs have already been utilized in several biomedical applications.[6,7,12-14] To demonstrate how MNP structure and the resulting properties are intertwined, we can use a specific application to identify the parameters that tune crucial magnetic properties. In

biosensing, for example, nanoparticles with higher saturation magnetization are preferred because they provide higher sensitivity and efficiency.[2] It has been demonstrated in several studies (*vide infra*)[15] that saturation magnetization increases linearly with size until it reaches the bulk value. While the correlation between magnetization and shape is not as direct, the effect of geometry on magnetic properties continues to be evaluated for biosensing applications.[16,17] A recent report pointed out the increased sensitivity of cubic MNPs for a biosensing platform owing to the increase in contact area for a cube in comparison to a sphere.[18] Composition also plays a significant role in influencing magnetic properties. However, due to concerns about the toxicity of the elements or compounds involved, the effect of the variation of composition has generally only been examined for *ex vivo* applications; consequently, data related to applications involving biological contact reflect these limitations. For implantable biosensors such as glucose monitoring systems, biocompatibility has been a significant challenge. These concerns also exist for the various magnetic materials used in research and have frequently been addressed by encapsulating the MNP in an appropriate coating.[19] The nature of the coating is an important consideration in such shell-core MNP designs since the coating might enhance or significantly reduce the magnetic properties of the core based on the interaction between the ligand and the nanoparticle surface,[7] the relative thickness of the shell, and the size of the nanoparticle being coated.[20,21]

From this initial example, it is apparent that an understanding of the effectiveness of the various types of MNPs from a specific application-based perspective fails to provide the full picture of how to optimize an MNP system. For this reason, the bulk of the text that follows will focus on the influence of specific parameters on magnetic

properties. Although we are aware that a combination of parameters might be involved in determining the effectiveness of a MNP for a specific application, for simplicity, we have listed tunable magnetic properties of fundamental importance for several applications in Table 1.1.

Table 1.1 Tunable Magnetic Properties Important for Biomedical Applications

Tunable Property	***Application***
Saturation magnetization (Ms)	Biosensing,[5] Drug Delivery,[7,8] Magnetic Resonance Imaging (MRI)[22]
Coercivity (Hc)	Biosensing,[5] Hyperthermia[9]
Blocking temperature (T_B)	Biosensing, Drug Delivery,[7,8] Hyperthermia[9]
Neel and Brownian relaxation time of nanoparticles (t_N & t_B)	Biosensing,[5] Hyperthermia[9]

These properties will be defined in the following section. We have also provided a brief list of published research focused on the key MNP parameters in Table 1.2. To maintain the practical utility of this chapter, we have focused on the following parameters that can be easily manipulated to tune the magnetic properties of the MNPs (Figure 1.1) using appropriate synthesis methods: (1) size, (2) shape, (3) composition, and (4) shell-core design. However, to provide context, the section that follows briefly outlines the fundamentals of nanomagnetism.

Table 1.2 Parameters Influencing Tunable Magnetic Properties

Influencing Parameters	***Partial List of References***

Size	23-30
Shape	31-40
Composition (changing elements, doping, cation changing distribution in the crystal)	41-48
Shell-core design	21, 22, 31, 49-54

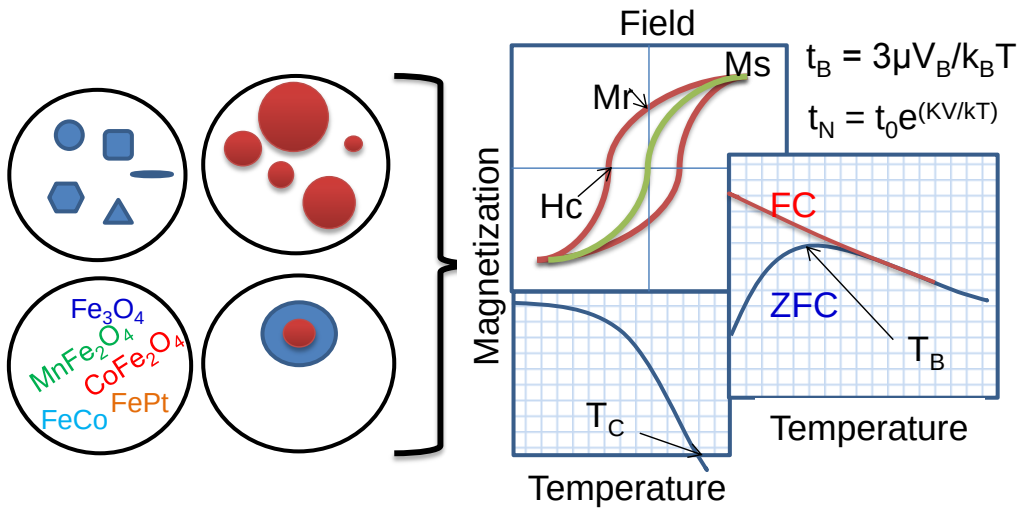

Figure 1.1 Effects of various parameters (e.g., shape, size, composition, architecture) on the magnetic properties of MNPs. (Abbreviations and magnetic property-based nomenclature has been defined and discussed in the following sections)

1.2 Nanomagnetism

The design of MNPs with tailored properties depends on the fundamental concepts of nanomagnetism (i.e., magnetism observed in nanoparticles). A review of what produces magnetization, including the relationship between various extrinsic and intrinsic parameters, will enable us to better evaluate the underlying factors that influence magnetism at the nanoscale. Explanations about the role of atomic and molecular structure upon magnetization are readily available.[55] However, from a practical

perspective, most of what we need to know to manipulate the effectiveness of these nanoscale magnets can be derived from prior experimental observations and an understanding of the role of MNP magnetic domain structure.

Based on the response of the intrinsic MNP magnetic dipole and the net magnetization in the presence and absence of an applied magnetic field, MNPs are typically classified as being either diamagnetic, paramagnetic, ferromagnetic, ferrimagnetic, and antiferromagnetic.[56,57] Figure 1.2 shows the net magnetic dipole arrangement for each of these types of magnetic materials. For diamagnetic materials in the absence of a magnetic field, magnetic dipoles are not present. However, upon application of a field, the material produces a magnetic dipole that is oriented opposite to that of the applied field; thus, a material that has strong diamagnetic character is repelled by a magnetic field. For paramagnetic materials, there exist magnetic dipoles as illustrated in Figure 1.2, but these dipoles are aligned only upon application of an external magnetic field. For the balance of the magnetic properties illustrated in Figure 1.2, the magnetization in the absence of an applied field reveals their fundamental character. Ferromagnetic materials have net magnetic dipole moments in the absence of an external magnetic field. In antiferromagnetic and ferrimagnetic materials, the atomic level magnetic dipole moments are similar to those of ferromagnetic materials, however, adjacent dipole moments exist that are not oriented in parallel and do not effectively cancel or reduce, respectively, the impact of neighboring magnetic dipoles within the material.

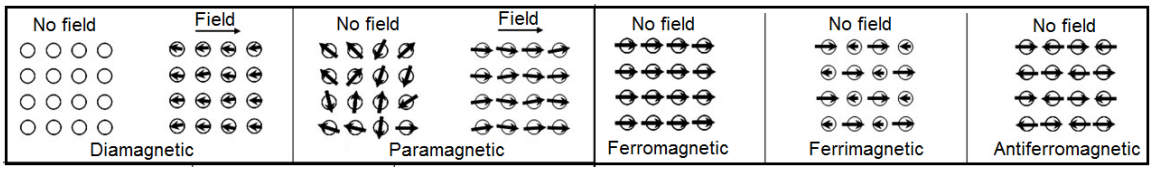

Figure 1.2 Magnetic dipoles and behavior in the presence and absence of an external magnetic field. Based on the alignment and response of magnetic dipoles, materials are classified as diamagnetic, paramagnetic, ferromagnetic, ferrimagnetic, antiferromagnetic. Reproduced with permission from 57.

Research in magnetic nanoparticles typically focuses on developing an optimal response for MNPs to an external magnetic field, and the majority of the published research has involved MNPs that are typically classified as either ferrimagnetic, ferromagnetic, or superparamagnetic particles, which are a special case of ferro- or ferri-magnetic particles. Below certain critical dimensions (that vary with the material parameters), MNPs exhibit magnetic responses reminiscent of those of paramagnetic materials, which is a zero average magnetic moment in the absence of an external field and a rapidly increasing (as compared to paramagnetic materials) magnetic moment under application of an external field in the direction of the field. This phenomenon, observed at temperatures above the so-called blocking temperature (see below), arises from the thermal fluctuations within the nanoparticles being comparable to or greater than the energy barrier for moment reversal, allowing rapid random flipping of the nanoparticle magnetic moments. In the case where the magnetization of the MNP over the measurement/observation interval is equal to zero in the absence of an external field, such nanoparticles are referred to as *superparamagnetic*. Superparamagnetism is especially important in applications such as drug delivery or MRI, where the nanoparticles exhibit no magnetic properties upon removal of the external field and

therefore have no attraction for each other, eliminating the major driving force for aggregation. More importantly, superparamagnetic nanoparticles allow better control over the application of their magnetic properties because they provide a strong response to an external magnetic field.

For MNPs, the maximum magnetization possible is called the saturation magnetization, and it arises when all the magnetic dipoles are aligned in an external magnetic field. Figure 1.3 shows a typical magnetization curve for ferromagnetic or ferrimagnetic nanoparticles showing the characteristic positions on the curve associated with *saturation magnetization* (Ms, maximum induced magnetization), *remanent magnetization* (Mr, induced magnetization remaining after an applied field is removed), and *coercivity* (Hc, the intensity of an external coercive field needed to force the magnetization to zero). In the same figure, in contrast to the hysteresis observed in the case of ferromagnetic nanoparticles (red loop), the response of superparamagnetic nanoparticles to an external field also follows a sigmoidal curve but shows no hysteresis (green line). The response of paramagnetic (blue line) and diamagnetic (black line) nanoparticles is also shown in the schematic. The Ms shown in Figure 1.3 depends on temperature and is at a maximum at 0 K when the thermal vibrations (and thus randomization of aligned moments) is reduced.

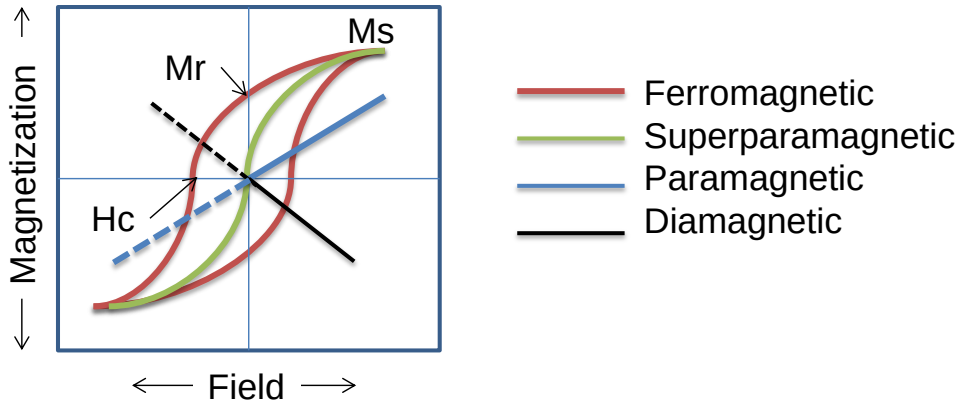

Figure 1.3 Magnetic behavior under the influence of an applied field, as further described in the text. The X-axis is the applied field (Oe), and the Y-axis is the induced magnetization (emu/g). Reproduced with permission from reference 6.

Above the temperature known as the blocking temperature (T_B), both ferromagnetic and ferrimagnetic nanoparticles exhibit superparamagnetic behavior manifested by rapid random MNP magnetization reversals leading to a zero time-average magnetic moment. $T_{B,}$ associated with the energy barrier, depends on the characteristic measuring time (which can vary from 100 to 10^{-8} s).[58] The magnetic behavior arises from the relative difference between the measuring time and the relaxation time. If the measuring time is greater than the relaxation time, the nanoparticles are considered to be in the superparagmagnetic regime; if the measuring time is less than the relaxation time, the nanoparticles are in a "blocked" (ferromagnetic) regime.[58] Experimentally, the value of T_B corresponds to the "merging point" of zero-field-cooled (ZFC) and field-cooled (FC) magnetization curves.[59] In ZFC measurements, a sample is first cooled to low temperature (e.g., 2 to 10 K) in the absence of an external field (zero-field). At this point, a small external field is applied, and the temperature is gradually increased while measuring the sample magnetization as a function of temperature. In FC measurements, the process is repeated, but the sample is cooled in the presence of an external field (~50

Oe), and the same external field is applied as the temperature is increased. As shown in Figure 4, the point where the two curves merge is the irreversibility temperature, T_{irr}, and the maximum on the ZFC curve is the blocking temperature, T_B (Figure 1.4).

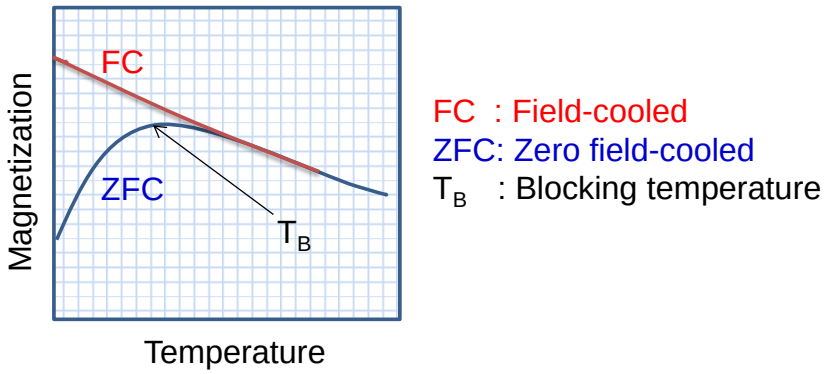

Figure 1.4 Experimental strategy for estimating the blocking temperature of magnetic nanoparticles.

The value of T_B can also be estimated using Equation 1.1 if the values of magnetic anisotropy and the size of the MNPs are known, and the particles have a single magnetic domain structure:[58]

$$T_B = KV/25k_B = K(4\pi r_o^3/3)/25k_B \quad (1.1)$$

where k_B is the Boltzmann constant, T is the temperature, K is an anisotropy constant, and V is the volume of one MNP. From Equation 1.1, we can see that blocking temperatures rapidly increase with particle size. However, this equation is not necessarily applicable for larger MNPs, where regions of uniform magnetization are separated by domain boundaries that develop during the process of MNP nucleation and growth.[4] If the MNP size is maintained below a critical volume/size during nanoparticle synthesis, the MNPs tend to develop as single magnetic domain structures, and at the

smallest sizes, they exhibit superparamagnetic behavior under standard conditions. These size regimes are illustrated in Figure 1.2.

The critical size (r_c), that corresponds with a transition from the single domain to the multi-domain regime, is complex.[60] One definition indicates that this size is associated with the point where it is energetically favorable for the magnetic grain (or particle) to exist without a domain wall.[61,62] This might be interpreted as a maximum size for such single-domained structures, as illustrated in Figure 1.5a. But with the broad array of magnetic materials in use in MNP research, it is challenging to define a discrete transition point for r_c and the term "pseudo-single domain" has been used for structures that fall in the overlap between nanoparticles that are well defined as being either single-domain or multi-domain structures.[56] A domain wall is a transition region between the different magnetic domains of uniform magnetization that develops when a magnetic material forms domains to minimize the magnetostatic energy; wall energy is the energy required to maintain this wall. When domains form, the magnetostatic energy decreases, and the wall energy and the magnetocrystalline anisotropy energy increases. For a nanoparticle to split into domains, its size should be greater than the thickness of the domain wall. Therefore, the domain wall thickness, and thus the critical size (r_c), is a function of the exchange energy (which is the energy required to keep the spins parallel and is low in the case of a thick wall), magnetization, and anisotropy of the nanoparticle.

(a)

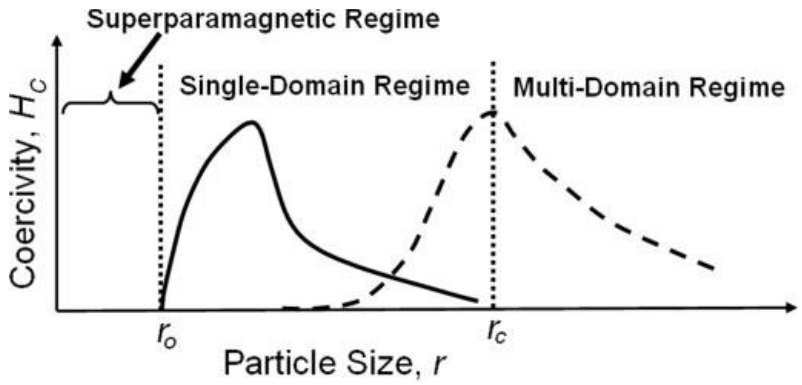

(b)

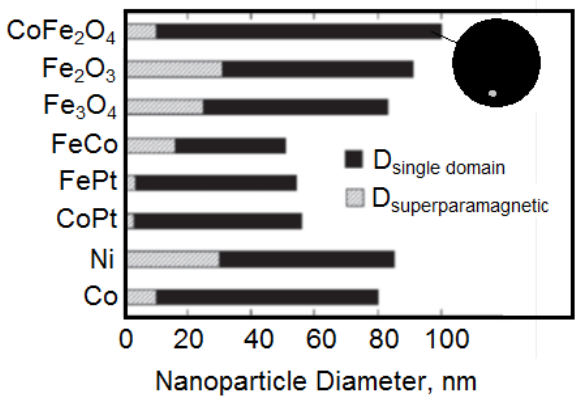

Figure 1.5 (a) Transition from superparamagnetic to single- to multi-domain regimes. Reproduced with permission from reference 57. (b) Maximum diameters for superparamagnetic and single domain nanoparticles of different compositions. Reproduced with permission from reference 63.

The transition point from superparamagnetic to single-domain to multi-domain for each type of MNP depends upon the size and/or geometry of the nanoparticles, as shown in Figure 1.5a, and upon the intrinsic material parameters such as Ms and K as is illustrated in Figure 1.5b for MNPs having different compositions.[2] From Equation 1.1 above, we can estimate the size at which spherical nanoparticles transition from superparamagnetic to single domain character as shown in Equation 1.2.

$$r_o = (6k_BT_B/K)^{1/3} \quad (1.2)$$

where r_o is transition point from superparamagnetic to single-domain (also illustrated in Figure 1.5a), k_B is the Boltzmann constant, T_B is the blocking temperature, and K is an anisotropy constant.

Nanomagnetism, which is responsible for superparamagnetic behavior and/or single/multi-domain behavior, is a vast topic, and the above discussion is a good starting point. It is important to understand the fundamental magnetic properties and their interdependence to be able to optimize them for a particular application. Application-specific concepts (like specific absorption rate (SAR)/specific loss power (SLP) for hyperthermia, proton relaxation, and contrast-enhancing efficiency in MRI applications) are included in the following sections as needed to describe the influence of various parameters on the magnetic properties of nanoparticles.

1.3 Effect of Different Parameters on Magnetic Properties: Tuning the Magnetic Properties of MNPs

Although there is a strong and relatively well-established dependence of magnetic properties on the size of the nanoparticles, magnetic behavior is complicated and cannot be defined with respect to one parameter. Peddis *et al.* described examples of anomalous behaviors (e.g., where large nanoparticles exhibit superparamagnetic behavior or lower coercivity than that found in smaller particles), which suggest that other factors also influence key magnetic properties.[26] In the subsection that follows, we review the important role of size upon the magnetic character of MNPs, and will follow this discussion with subsections describing how shape, composition, and shell-core design can be utilized as parameters to optimize magnetic properties.

1.3.1 Effect of Size on Magnetic Properties

It has been shown that many of the unique magnetic properties of nanoparticles can be attributed to their high surface-to-volume ratio.[1,3] Ms varies with size until it reaches a threshold size beyond which magnetization is constant and is close to the bulk value. The linear dependence of Ms on size has been demonstrated in several studies, and several examples are provided in Table 1.3. However, the tunable property of size is subtractive with respect to Ms and superparamagnetism: for example, when the size decreases, the nanoparticle moves toward superparamagnetism but may have a reduced Ms. Depending on the targeted application, we might choose to tailor the size of the nanoparticles to tune these parameters (e.g., to favor superparamagnetism or high Ms).

As illustrated in Figure 1.5a, the size of the nanoparticle helps define the nanoparticle regime and hence its magnetic behavior. As the size of the MNP decreases, the magnetic anisotropy energy per nanoparticle decreases. Magnetic anisotropy energy is the energy that keeps the magnetic moment in a particular orientation. At a characteristic size for each type of MNP, the anisotropy energy becomes equal to the thermal energy, which allows the random flipping of the magnetic moment.[64] The flipping occurs at sizes below r_o, and the nanoparticle is then defined as being superparamagnetic. The magnitude of Ms also strongly depends on the size of the nanoparticle and is described by Equation 1.3.[65] MNPs possess a disordered spin layer at their surfaces, and when the size of the nanoparticle is small (< 5 nm), the ratio of disordered layer to the radius of the MNP is significant. Surface spin disorder thus leads to reduced Ms for smaller nanoparticles:

$$Ms = Ms_b[(r - d)/r]^3 \quad (1.3)$$

where r is the radius, d is the thickness of the MNP surface exhibiting disordered spins, and Ms_b is the bulk Ms. Recent studies have demonstrated that the surface functionalization of MNPs can reduce the level of surface spin disorder observed in small nanoparticles, thus increasing their measured Ms.[66,67] Guardia *et al*. compared the magnetic properties of iron oxide (Fe_3O_4) MNPs of diameters 6, 10, and 17 nm and observed that the Ms of each unexpectedly reached the bulk value. They attributed this decrease in surface spin disorder (and hence increased magnetization) to covalent bonding of oleic acid to the nanoparticles. However, Nagesha *et al.* observed no such phenomenon when they examined 10 nm Fe_3O_4 MNPs that were dopamine-stabilized and oleic acid-stabilized. The Ms and T_B increased from 38 emu/g Fe and 30 K for oleic acid functionalization to 60 emu/g Fe and 50 K for dopamine functionalization. The authors observed a significant improvement in magnetic properties after dopamine functionalization, but unlike the previous study, the Ms of the 10 nm oleic acid-functionalized nanoparticles was only a fraction of the bulk value.

Due to their facile synthesis and potential for use in biomedical applications, Fe_3O_4 MNPs are commonly the focus of studies that evaluate the effect of various nanoparticle parameters on magnetic properties.[10,68] However, there is also substantial research regarding other types of nanoparticles tailored for specific applications. In Table 1.3, we have summarized recent studies that evaluated the effect of size upon the magnetic properties of different types of MNPs.

Table 1.3 Magnetic Properties of a Variety of Types of MNPs of Varying Sizes

Reference	**MNP**	**Size (nm)**	**Ms (emu/g)**	**Coercivity (G)**	**Blocking Temperature (T_B, K) or Neel Temperature (T_N, K)**
Caruntu, D. *et al.*[24]	Fe_3O_4	6.6	71	16	203
		11.6	77	15	264
		17.8	83	3	>300
Peddis, D. *et al.*[26]	$CoFe_2O_4$	2.8	109	-	51
		2.9	89	-	80
		6.7	78	-	126
Guardia, P. *et al.*[32]	Fe_3O_4	4.2	75	318	19
		7.4	70	270	28
		8.1	65	70	49
		17	82	364	>275
		45	92	340	>275
Han, T. *et al.*[27]	$HoMnO_3$	30	0.3 (5K)	382	50 (T_N)
		200	0.1 (5K)	~0	70 (T_N)
Markovich, V. *et al.*[28]	$Sm_{0.8}Ca_{0.2}MnO_3$	23	-	-	53.8
		100	-	-	58.5
Pereira, C. *et al.*[23]	Fe_3O_4	4.9	60.4		33.9
		6.3	64.8		56.2
		8.6	58.0		96.0
	$CoFe_2O_4$	4.2	30.6		89.4
		4.8	46.0		149.2
		18.6	48.8		286.4
	$MnFe_2O_4$	9.3	57.1		397.7
		11.7	54.6		91.0
		59.5	35.2		96.6
He, X. *et al.*[34]	Ni	24	25.3	120	-
		50	32.3	79	-
		96	40.6	18	-
		165	46.7	146	-
		200	52.0	158	-
Noh, S. *et al.*[31]	$Zn_{0.4}Fe_{2.6}O_4$	18	165	60	320
		60	190	140	-
		120	200	60	-

In most of the studies listed here, the value of Ms increases with size until it reaches a maximum that is close to the bulk magnetization value; this trend appears to be independent of the synthetic route. Three studies by independent research groups using

distinct methods of synthesis effectively demonstrated this assertion for Fe_3O_4 nanoparticles.[23,24,32] Additionally, in most of the studies shown in Table 1.3, the coercivity follows a similar trend, but after reaching a maximum, the coercivity decreases with size. The latter phenomenon occurs because as the size of the MNPs increases, the nanoparticles become pseudo-single-domain and then multi-domain structures in which the moment of each domain may not be oriented in the same direction. On application of a magnetic field, some of the non-parallel moments cancel (vector addition of forces), leading to a reduced level of coercive field (coercivity) required to force the magnetization to zero. Although Guardia *et al.* have reported one of the highest Ms values found in the literature, they did not provide an explanation for the sinusoidal trends of coercivity of the Fe_3O_4 nanoparticles observed in the size range of 7.4 nm to 45 nm.[32] A similar trend was observed in the case of Ni nanoparticles.[34] Figure 1.5a shows that coercivity depends on the size of the nanoparticles involved, and that for a series of MNPs over a range of sizes, MNPs go through two maxima in the 2 separate regimes (single-domain and multi-domain). Based on the coercivity values observed by Guardia *et al.*, we can conclude that the Fe_3O_4 MNPs synthesized by them are multi-domain MNPs above 17 nm. In the case of the Fe_3O_4 MNPs that are less than 20 nm in size, the presence of an oxidized layer of Fe_2O_3 on the surface of the Fe_3O_4 MNPs becomes significant, and the nanoparticles can no longer be classified as Fe_3O_4 MNPs.[69] We emphasize that this effect is in addition to the spin-disorder effect described earlier; consequently, the reduced Ms values might also arise from a higher ratio of low-magnetization maghemite (Fe_2O_3) to the high-magnetization magnetite (Fe_3O_4). Regardless of the composition, the size-dependence of MNP-properties is consistent.

This was demonstrated by Demortiere *et al.*, who studied the magnetic behavior of $Fe_{2.66}O_4$, a structure between Fe_3O_4 and Fe_2O_3, and observed that saturation magnetization increased from 29 emu/g to 77 emu/g and blocking temperature increased from 10 K to 100 K as the nanoparticle size was increased from 2.5 nm to 14 nm.[70]

MNPs are also used in hyperthermia therapies, which involve increasing the temperature of an *in vivo* MNP-based therapeutic system to a level that either stimulates the immune system and potentiates other therapies (up to ~46°C) or causes targeted ablation (above 46°C).[71] In this application, size becomes a critical tuning parameter since the application of an alternating current (AC) magnetic field will lead to heating that arises from either Neel or Brownian relaxation processes or hysteresis losses. Within the alternating magnetic field, either the magnetic moments rotate or the nanoparticle itself rotates, and when these MNPs relax back to their original magnetic field orientation (Neel relaxation time, t_N and Brownian relaxation time, t_B, respectively), heat is released. The efficiency of heating for a magnetic material is described by the specific absorption rate (SAR), which is equal to the rate at which energy is absorbed per unit mass of the nanoparticles at a specific frequency[72] and is described as shown in Equation 1.4. Since the absorption of heat absorption arises from processes associated with relaxation and hysteresis losses and since it is defined on a per gram basis, it is also described as "specific loss" power (SLP).

$$\text{SAR (or SLP), W/g} = C(\Delta T/\Delta t) = (\text{Area of the hysteresis loop}) \times (\text{Frequency, f}) \qquad (1.4)$$

where C is the specific heat capacity of water, and $\Delta T/\Delta t$ is the rate of change of temperature. The SAR/SLP values that result from the relaxation processes are roughly

proportional to the Ms and magnetocrystalline anisotropy constant (K), and are inversely proportional to the size distribution of the nanoparticles.[73] In this review, we use both SLP and specific absorption rate (SAR) to align with the nomenclature chosen by the authors to describe their results.

Mornet *et al.* showed that the SARs of MNPs were influenced by the composition, core diameter, coating, and frequency of the AC magnetic field.[71] In the case of large, ferromagnetic nanoparticles, heating occurs due to hysteresis losses and Brownian relaxation. For small nanoparticles in the single-domain or superparamagnetic range, hysteresis losses are negligible or absent, and heating arises from Neel and Brownian relaxation. The extent of the contribution of each mechanism is difficult to distinguish, but the dominant mechanism can be elucidated by determining the faster relaxation time.[67] In general, Neel relaxation dominates when nanoparticles are less than 20 nm, and Brownian relaxation dominates when the nanoparticles are larger than 20 nm.[74] Fortin *et al.* carried out a comprehensive study to distinguish between the contributions of Neel and Brownian relaxations to heat generation and SLP[75] as discussed further later in this section. A useful study by Jeun *et al.* established a threshold size (~9.8 nm) below which the measured SLP is insufficient for hyperthermia applications.[76] These researchers evaluated Fe_3O_4 MNPs of sizes in the range of 4.2 nm to 22.5 nm and determined that the SLP was insignificant (< 45 W/g) at sizes < 9.8 nm, but was greater by an order of magnitude in the size range of 11.8 to 22.5 nm. Lartigue *et al.* also observed a size threshold of 7 nm below which significant heating was not produced.[77] The SAR values jumped from almost zero for 4.1 and 6.7 nm MNPs to ~76 W/g for 35 nm rhamnose-coated Fe_3O_4 MNPs. In another study of magnetic nanoparticles having

diameters of 5, 10, 12.8, 14 nm, measurements at 400 kHz and 24.5 kA/m amplitude showed a maximum SLP of 447 W/g for the 14 nm Fe_3O_4 MNPs.[78] These data are important because a high SLP is necessary for efficient hyperthermia therapy with a minimal dose of MNPs in the body. Table 1.4 provides a summary of studies that have attempted to correlate size with SLP. A recent study presented and validated (with both commercial and in-house-synthesized Fe_3O_4 nanoparticles) an analytical model in which SLP is directly proportional to the AC magnetization for nanoparticles ranging in size from 5 nm to 600 nm; in contrast, there was no dependence on DC magnetization (Ms).[79]

To optimize the effectiveness of hyperthermia treatment using MNPs, Khandhar *et al.* tailored the nanoparticle size to the applied frequency.[25] Recent research indicates that SAR/SLP can be maximized if the total relaxation time matches the applied frequency,[80] which along with the applied field has a FDA-regulated upper limit.[79] The total relaxation time is the sum of t_N and t_B. Four equations correlate the relevant factors:

$$t_N = t_0 e^{(KV/kT)} \tag{1.5}$$

$$t_B = 3\mu V_B/k_B T \tag{1.6}$$

$$\nu_N = 1/(2\pi\, t_N) \tag{1.7}$$

$$\nu_B = 1/(2\pi\, t_B) \tag{1.8}$$

where t_0 is the relaxation time of non-interacting MNPs (~10^{-9} to 10^{-12} s), K is the anisotropy constant, k_B is the Boltzmann constant, V is the volume of nanoparticle, μ is the viscosity of the medium, V_B is the hydrodynamic volume, T is the temperature, ν_N is the frequency for maximum heating due to t_N, and ν_B is the frequency for maximum heating due to t_B.

Table 1.4 SLP of MNPs of Varying Sizes

Reference	MNP	Size (nm)	SAR/SLP (W/g)	Frequency/Amplitude
Mornet, S. *et al.*[71]	Single domain Fe_3O_4 coated with dextran	10–12	210	At 880 kHz and 7.2 kA/m
	Single domain Fe_3O_4 coated with carboxymethyl dextran	6–12	90	At 880 kHz and 7.2 kA/m
	Multi-domain Fe_3O_4	150–200	45	At 880 kHz and 7.2 kA/m
	Single domain Fe_3O_4	8	21	At 300 kHz and 6.5 kA/m
	Single domain γ-Fe_2O_3	5	524	At 500 kHz and 12.5 kA/m
	Single domain γ-Fe_2O_3	7	626	At 500 kHz and 12.5 kA/m
Jeun, M. *et al.*[76]	Fe_3O_4	4.2	45	At 110 kHz and 140 Oe
		5.8	30	
		7.9	28	
		9.8	28	
		11.8	150	
		14.0	201	
		16.5	249	
		20.0	309	
		22.5	322	
Mueller, R. *et al.*[30]	Fe_3O_4	10.9	216	At 210 kHz and 30 kA/m
		15.2	702	
Fortin *et al.*[75]	γ-Fe_2O_3	5.3	4	
		6.7	14	
		8.0	37	
		10.2	275	
		16.5	1650	
	$CoFe_2O_4$	3.9	40	
		9.1	360	At 700 kHZ and 24.8 kA/m
	γ-Fe_2O_3 in 95% water 5% glycerol	7.1	135	
	γ-Fe_2O_3 in 40% water 60% glycerol	7.1	125	
	γ-Fe_2O_3 in 0% water 100% glycerol	7.1	100	
	$CoFe_2O_4$ in 95% water 5% glycerol	9.7	420	
	$CoFe_2O_4$ in 40% water 60% glycerol	9.7	145	
	$CoFe_2O_4$ in 0% water 100% glycerol	9.7	90	
Lartigue *et al.*[77]	Fe_3O_4 coated with rhamnose	4.1	0	At 168 kHz and 21 kA/m
		6.7	0	
		10.0	30	
		16.2	61	
		35.2	76	

Equipped with these equations, we can tailor the sizes of the nanoparticles for maximum heating. The above equations show how t_B depends directly on V_B and μ, and inversely on T; t_N varies exponentially with KV. We can also quantify the influence of size, viscosity of the suspension medium, anisotropy constant, and temperature, on the relaxation time and the heat output. Fortin *et al.* optimized the SLP by tuning the Brownian and the Neel relaxation time by varying the viscosity of the suspension medium (lower Brownian relaxation time for higher viscosity) and sizes and composition of nanoparticles (exponentially higher Neel relaxation time for MNPs with higher volume and higher anisotropy constant which is a function of the MNP composition).[75] The significant reduction in SLP for $CoFe_2O_4$ MNPs and the only-slight decrease in SLP for γ-Fe_2O_3 MNPs when suspended in high-viscosity glycerol, confirmed the dominance of Brownian and Neel for $CoFe_2O_4$ and γ-Fe_2O_3 MNPs, respectively. Below 10 nm, $CoFe_2O_4$ MNPs had a higher SLP as compared to γ-Fe_2O_3 MNPs of the same size and appeared to be better candidates for hyperthermia applications.

As expected from Equation 1.1, the blocking temperature is generally found to be directly proportional to the nanoparticle volume/size. This relationship is in complete agreement with Monte Caro simulations demonstrating that the blocking temperature varied linearly with nanoparticle size.[81] Additionally the simulations also predicted a dependence of blocking temperature on the nanoparticle concentration, which has yet to be established experimentally. Rosenweig *et al.* computed the effect of different parameters on the heating rate of different superparamagnetic nanoparticles suspended in tetradecane when subjected to alternating DC current.[82] In another simulation study, Carrey *et al.* evaluated the various theories describing relaxation losses and hysteresis

losses.[80,83] They concluded that the anisotropy of the MNPs is the critical parameter to tune SAR and they proposed formulae to estimate optimum volume for that anisotropy.

Barring a few examples, all of the nanoparticles in Table 1.3 exhibit blocking temperatures that are much lower than room temperature, which means that these nanoparticles are superparamagnetic at room temperature. Also, when the nanoparticles are small, the surface effects dominate (as expected from Equation 1.3), giving rise to disordered spins of surface cations. Koseoglu *et al*. determined that the anisotropy constant stemming from this high anisotropy layer was inversely proportional to the size of Fe_3O_4 MNPs in the 1–11 nm range.[84]

Given that magnetic behavior is strongly size-dependent, size can serve as a design parameter that can be readily manipulated to tune the magnetic properties of Ms, coercivity, blocking temperature, and SLP for increased efficiency in MNP applications. However, size manipulation alone might sometimes fail to produce the desired results.

1.3.2 Effect of Shape on Magnetic Properties

As we have seen in the previous subsection, substantial efforts have been dedicated toward understanding the relationships between nanoparticle size and magnetic properties. In comparison, there is remarkably little research on the effect of shape on the magnetic properties of nanoparticles having the same volume or related size parameter. There are many studies on the synthesis of unique shapes of MNPs: for example, ferrite nanocubes,[37,85] maghemite nanorods,[86] NiFe nanowires,[87] cobalt nanodiscs,[39,88] magnetite tetrapods,[89] and Au-MnO nanoflowers.[90] Table 1.5 lists studies that have compared various shapes and reported comparisons on the basis of their magnetic properties.

Among the properties evaluated, comparison of a set of $CoFe_2O_4$ cubes and spheres by Song *et al.* in 2004 found a large difference only in the coercivity.[35] The researchers attributed this difference to surface pinning that arises due to missing coordinating oxygen atoms. Unlike the curved topography in spherical $CoFe_2O_4$ MNPs, in the case of cubic $CoFe_2O_4$ MNPs, they hypothesized that fewer missing oxygen atoms and thus less surface pinning might have led to lower coercivity for the cubic structures. In two studies that compared cubic and spherical Fe_3O_4 MNPs, both Salazar-Alvarez *et al.* and Zhen *et al.* observed a higher blocking temperature for the spherical Fe_3O_4 MNPs[36,38] Noh *et al.* corroborated this observation of high T_B for spherical nanoparticles in a comparison of cubic and spherical $Zn_{0.4}Fe_{2.6}O_4$ MNPs.[31] These observations, and the explanation given above, are in accord with Equation 1.1; hence, the anisotropy constant for spherical nanoparticles is higher than cubic nanoparticles of the same volume.

Zhen *et al.* also observed that cubic MNPs had a higher Ms as compared to spherical MNPs of the same volume.[38] To explain the higher Ms in cubic nanoparticles as compared to spherical nanoparticles of the same volume, Noh *et al.* simulated the orientations of the magnetic spin structures in both a cube and a sphere using an object-oriented micromagnetic framework program (OOMMF) and found that the disordered spins were 4% in cubic MNPs and 8% in spherical MNPs.[31] Based on these simulations, lower disordered spins in cubes should give rise to a higher Ms for cubic MNPs. However, a higher Ms for cubic nanoparticles as compared to spherical nanoparticles of the same volume appears not to be a universal observation. It becomes especially challenging to draw a correlation between shape and Ms for nanoparticles of dissimilar volumes in Table 1.5. A high Ms is expected for lower-volume nanoparticles due to its

per-gram definition; however, a high Ms might be observed for a higher-volume cube due to lower disordered spins. Table 1.5 thus shows no unifying trend for any of the listed properties as a function of shape and volume. Likewise, since most of the shape-comparative studies have been performed for MNP sizes in the superparamagnetic regime or at least in the single-domain regime, it would be useful to the scientific community if future research focused on collecting magnetic data for varying shapes of nanoparticles spanning a larger range of sizes.

Table 1.5 Comparison of Magnetic Properties of Various Shapes of Nanoparticles

Reference	**MNP**	**Shape**	**Size (nm) Volume comparison**	**Ms (emu/g)**	**Coercivity (G)**	**T_B (K)**
Song, Q. *et al.*[35]	$CoFe_2O_4$	Sphere Cube	10 8 $V_{sphere} = V_{cube}$	80 80	16000 Oe 9500 Oe	275 275
Salazar-Alvarez, G. *et al.*[36]	γFe_2O_3	Sphere Cube	14.5 12 Side $V_{sphere} = V_{cube}$	75 75	30 mT 33 mT	235 190
Chou, S. *et al.*[40]	FePt	Cube Octapod Cuboctahedron	11.8 12 body dia 6.8 dia $V_{cube} > V_{octapod} > V_{octahedron}$	2.5 2.0 0.1	164 Oe 1461 Oe 11 Oe	50 95 20
Zhen, G. *et al.*[38]	Fe_3O_4	Cube Sphere	8.0 Side 8.5 $V_{cube} > V_{sphere}$	40 31	0 0	60 100
Montferrand, C. *et al.*[33]	Fe_3O_4 (includes γFe_2O_3)	Cube Rod Sphere Octahedron	12 Side 12 Width 12 12 Width $V_{cube} > V_{rod} > V_{sphere} > V_{octahedron}$	40 18 80 80	0 4.4 kA/m 0 0	
Noh, S. *et al.*[31]	$Zn_{0.4}Fe_{2.6}O_4$	Sphere Cube	22 18 $V_{sphere} = V_{cube}$	145 165	0 0	360 320

*$G = 10^{-1}$ mT, $G = (1/4\pi)$ kA/m

For the last couple of decades, MNPs have also been evaluated for their use as contrast agents in magnetic resonance imaging (MRI). MRI is a powerful diagnostic technique in which a magnetic field is applied to a sample, and a magnetic dipole is induced in the nanoparticles used as contrast agents, which then affects the magnetic relaxation processes of the protons present in the surrounding fluid. On application of an external magnetic field, protons in the absence of MNPs experience a relaxation process that differs in the presence of MNPs and occurs by 2 pathways (longitudinal and transverse). The parameter T_2 reflects the attenuation of the induced perpendicular magnetization, and T_1 reflects attenuation back to the initial state. The decrease in the relaxation times (T_1 or T_2) under a local field variation (presence of MNPs) leads to enhanced image contrast. A reduction in T_1 provides a positive contrast and a reduction in T_2 provides a negative contrast. Thus, if MNPs accumulate in the tissue to be imaged, they can provide high-resolution MRI images. An example would be the use of magnetic iron oxide nanoparticles as contrast agents to image the liver, spleen, and bone marrow due to their ability to reduce T_2 in these tissues.[91] The contrast enhancement effects have been shown to be directly related to the Ms value of the nanoparticles.[73] Therefore, what is crucial in an MRI application is the relative strength of the magnetic field of the MNPs (indicated by their saturation magnetization) and their impact upon the spin-spin relaxation time (T_2) of the surrounding protons.

The contrast-enhancing efficiency is described using relaxivity coefficients (r_1, r_2)[92,93] and these parameters are correlated using the Equation 1.9:

$$1/T_i = 1/T_i^0 + r_iC \quad i=1,2 \tag{1.9}$$

where T_1, T_2 are the longitudinal and transverse spin relaxation times in the presence of nanoparticles, T_1^0, T_2^0 are the relaxation times in pure water, r_1, r_2 are the relaxivity constants, and C is the concentration of the nanoparticles (contrast agent).

Experimentally, we can obtain $r_{i\ (i=1,2)}$ from a plot of $1/T_{i\ (i=1,2)}$ versus C. For example, in Equation 1.9, r_2 is a constant, independent of concentration, and having a value associated with each contrast agent, reflecting the relative strength of the magnetic field surrounding the individual MNPs. To obtain enhanced negative contrast, T_2 must be lowered, which requires either the use an agent having a high r_2 value or the use of a higher concentration of agent. Examples of agents with high r_2 values are superparamagnetic nanoparticles with high saturation magnetization. To obtain enhanced positive contrast, T_1 must be lowered, which requires the use of agents having a high r_1 value. T_1 agents to obtain enhanced positive contrast generally include gadolinium-based materials.[93]

The use of superparamagnetic iron oxide nanoparticles as contrast agents has been approved clinically[2,94] and recent research involving a greater variety of superparamagnetic MNPs has been pursued, providing additional insight into the parameters that have an impact upon r_2. Zhen *et al.* observed that, due to their higher crystallinity, cubic Fe_3O_4 MNPs showed four times smaller relaxation time and thus better image contrast when compared to spherical Fe_3O_4 MNPs.[38] On comparing faceted irregular (FI) $CoFe_2O_4$ with spherical $CoFe_2O_4$ MNPs, Joshi *et al.* observed a higher r_2 (with respect to Ms) for the FI MNPs and a lower T_2.[92] In addition to the unique morphology-generated gradient for the magnetic field, the researchers attributed this variance to the higher surface-area-to-volume ratio for the FI MNPs as compared to the

spherical MNPs, where more protons were present in the vicinity of this magnetic field, leading to faster relaxation (T_2). The delivery of such nanoparticles to the tumor site takes place due to the phenomena of enhanced permeation and retention.[95] However, large aggregates may be eliminated from the body instead of being accumulated in the tumor. The 22-nm edge length Fe_3O_4 nanocubes provided this MNP colloidal stability and a high r_2 relaxivity that enabled its successful use for *in vivo* MRI using a 3-T MR scanner.[95]

We have seen that the SAR values increase with nanoparticle size. However, the effect of the shape on SAR results has not yet been established. Guardia *et al.* reported the highest SAR of 2452 W/g Fe at 520 kHz and 29 kA/m for cubic Fe_3O_4 with an edge length of 19±3 nm.[72] Additionally, Noh *et al.* have reported a maximum SLP of 4060 W/g for higher-sized 40 nm (edge length) $Zn_{0.4}Fe_{2.6}O_4$ nanocubes in the size range 20 to 140 nm.[31]

Based on the limited studies currently available in the literature, we can draw no broad conclusions in favor of a particular shape. However, MNPs with flat surfaces show promise for use in biomedical applications (e.g., biosensing, hyperthermia, and MRI), and warrant the pursuit of more shape-effect studies. Further, it is clear from the most recent MNP research that the impact of MNP shape on magnetic properties can be used as a powerful tool for modifying these properties to enhance the effectiveness of MNPs in a particular application.

1.3.3 Effect of Composition on Magnetic Properties

Composition is the most commonly cited parameter responsible for determining the specific magnetic properties of a material. In the previous section, we classified all

materials (without regard to their specific atomic content) based on their magnetic properties (i.e., diamagnetic, paramagnetic, ferromagnetic, ferrimagnetic, and antiferromagnetic). These magnetic properties arise in the presence or absence of unpaired valence electrons located on the metal atoms or metal ions found in MNPs.[96,97] The orientation of the magnetic moment, μ, associated with the electrons defines the magnetic behavior. Using the magnetic moment of a single electron, 1.73 Bohr magnetons (BM), we can estimate the magnetic moment in a MNP. For example, with 5 unpaired electrons, Fe^{+3} has a moment of ~8.5 BM, which underlines the strong dependence of the composition (atomic state) on the magnetic behavior of a specific element. Additionally, the distribution of cations within the octahedral (O_h) and tetrahedral sites (T_d) of the commonly-found spinel or inverse spinel crystal structures, is another critical determinate of μ. For example, in the crystal structure of Fe_3O_4 (which is actually $FeFe_2O_4$), Fe^{+2} and half of Fe^{+3} occupy octahedral sites, and the remaining half of the Fe^{+3} cation occupies a tetrahedral site in a face-centered cubic (*fcc*) lattice structure.

As shown in Figure 1.6, the magnetic moments of the cations in the octahedral sites are aligned parallel to the magnetic field, and the ones in the tetrahedral sites are antiparallel, leading to a decrease in μ. Therefore, the net change in moment depends on the nature of the cations present in specific sites, such as the tetrahedral site for ferrites. Several research groups have investigated this structure by examining the effects of dopants (M cation) on the magnetic properties of ferrites (MFe_2O_4). The results from these studies are summarized of Table 1.6. Importantly, the properties of doped MNPs depend on the effectiveness of the synthetic procedure for consistently producing MNPs

with crystal structures that are unvarying in their composition. Without a reliable basis for comparison, it can be challenging to compare the magnetic properties of MNPs synthesized by a variety of research groups using distinct synthetic routes. In Table 1.6, we highlight studies that have compared properties as a function of the relative ratio of cations, or the position and distribution of the cations, or otherwise systematically varying the composition of the MNPs.

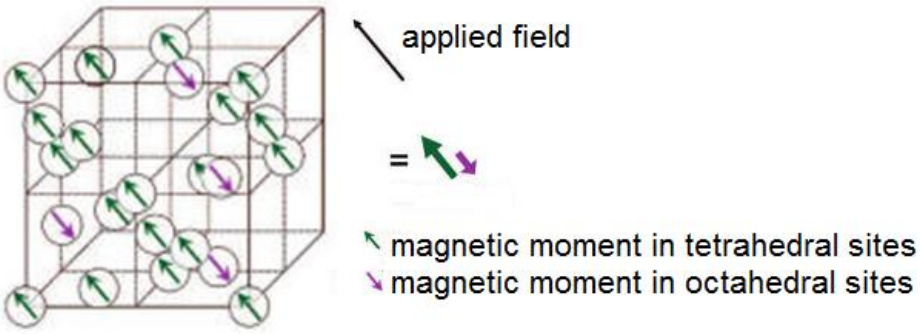

Figure 1.6 Tetrahedral and octahedral sites in an inverse spinel structure of ferrites. Reproduced with permission from reference 98.

The impact of the composition of the MNPs on magnetic properties has been studied by varying the precursor concentration, the method of synthesis, and the nature of the dopant, and by controlling post-synthetic cation exchanges. Based upon the presence of unpaired electrons, it is now possible to rationalize the magnetic behavior observed by Pereira *et al.* (Table 1.1) for Fe_3O_4 and $MnFe_2O_4$ MNPs as compared to $CoFe_2O_4$.[23] As expected from the number of unpaired electrons for the substitutions made in these spinels, Deng *et al.* observed the highest magnetization for Fe_3O_4, but obtained a measurement that was anomalously low for $MnFe_2O_4$.[48] In another study that compared $MnFe_2O_4$, $FeFe_2O_4$, $CoFe_2O_4$, and $NiFe_2O_4$ MNPs of the same 12-nm size, $MnFe_2O_4$ showed the highest

magnetization.[98] The authors rationalized this result by comparing the crystal structure of each of the MNPs. The $MnFe_2O_4$ MNPs had a mixed spinel structure (Mn^{+2} and Fe^{+3} occupying both O_h and T_d sites), and the rest had an inverse spinel structure (Mn^{+2} and Fe^{+3} occupying O_h sites but only Fe^{+3} occupying the T_d sites).

Table 1.6 Effect of Composition on Magnetic Properties

Reference	**Nanoparticle**	**Size (nm)**	**Method of changing composition**	**Ms (emu/g)**	**Coercivity (G)**
Deng, H. *et al.*[48]	$FeFe_2O_4$	200	Varying precursors	81.9	
	$MnFe_2O_4$	200		53.2	
	$CoFe_2O_4$	200		61.6	
	$ZnFe_2O_4$	200		60.0	
Lee, J. *et al.*[98]	$FeFe_2O_4$	12	Varying precursors	101	
	$MnFe_2O_4$	12		110	
	$CoFe_2O_4$	12		99	
	$NiFe_2O_4$	12		85	
Gabal, M. *et al.*[99]	$Ni_{0.8-x}Zn_{0.2}Mg_xFe_2O_4$		Varying precursor ratios		
	x=0	36		43.1	65.8 G
	0.2	41		41.7	57.0 G
	0.4	45		41.0	35.0 G
	0.6	35		30.4	17.4 G
	0.8	59		36.1	11.9 G
Larumbe, S. *et al.*[44]	$FeFe_2O_4$	8	Varying precursor ratios	80.1	153 Oe
	$Ni_{0.04}Fe_{2.96}O_4$	8		84.2	180 Oe
	$Ni_{0.06}Fe_{2.94}O_4$	10		80.5	250 Oe
	$Ni_{0.11}Fe_{0.89}O_4$	8		82.8	190 Oe
Turtelli, R. *et al.*[45]	$CoFe_2O_4$ – different cation distribution		Varying synthesis methods		
	Ball milling	200		80.9	1750 Oe
	Sol gel	200		83.1	500 Oe

Spinel ferrites have continued to be widely investigated, including recent detailed studies of the impact of cation placement on MNP magnetic field strength. Gabal *et al.* examined a series of $Ni_{0.8-x}Zn_{0.2}Mg_xFe_2O_4$ ($x \leq 0.8$) ferrites and found that increasing the Mg^{+2} content during synthesis led to the replacement of the higher magnetic moment Ni^{+2} by the zero magnetic moment Mg^{+2}, which led to decreases in the Ms and coercivity of

the nanoparticles.[99] The same research group observed a similar reduction in the value of Ms when Ni^{+2} cations were replaced by Cu^{+2} cations in studies of MNPs having the form $Ni_{1-x}Cu_xFe_2O_4$ $(0 \leq x \leq 1)$.[43] In addition to the nature of the cation itself, its relative distribution in the crystal structure is equally important, particularly in the case of spinel structures, where the distribution of cations in octahedral and tetrahedral sites defines the type of magnetic behavior. Turtelli *et al.* studied the magnetic properties of $CoFe_2O_4$ MNPs synthesized by sol-gel and ball milling methods and ascribed the difference in properties to dissimilar cation distributions formed by the two different synthetic methods.[45]

While varying precursor ratios and synthesis methods offers one way of introducing a composition change to MNPs, cationic exchange is another attractive technique for varying the cationic composition to tailor the magnetic properties of the resulting nanoparticles. Cationic exchange is especially attractive in the case of ferrite nanoparticles where physical and magnetic properties can be tuned by replacing a cation, without affecting its crystal structure.[100] Larumbe *et al.* studied the effect of nickel doping on Fe_3O_4 MNPs, where Ni^{+2} partially displaced Fe^{+2} from the octahedral sites.[44] Although there was no substantial change in the value of Ms, the blocking temperature for MNPs of the form $Ni_xFe_{3-x}O_4$ reached a maximum for $Ni_{0.06}Fe_{2.94}O_4$ MNPs (i.e., higher than that for Fe_3O_4 MNPs). As indicated by Equation 1.1, the blocking temperature is expected to vary linearly with volume, and the authors attributed the increase in blocking temperature to an increase in grain size. In addition to cationic exchange, Jang *et al.* demonstrated the importance of the proper replacement of Zn^{+2} dopants in Td sites[73] for optimum tuning of nanomagnetism. They observed a maxima in

Ms at x=0.4 for 15 nm Zn-doped nanoparticles of $Zn_xMn_{1-x}Fe_2O_4$ and $Zn_xFe_{1-x}Fe_2O_4$ that resulted in an eight- to fourteen-fold increase in MRI contrast and a four-fold enhancement in hyperthermic effects compared to conventional iron oxide nanoparticles. Fantechi *et al.* reported a detailed investigation on the effect of Co doping on 5 nm Co-doped nanoparticles where Ms and K showed maximum values at intermediate compositions of $0.5<x<1$ in $Co_xFe_{(8/3-2x/3)}O_4$.[100] In another post-synthesis cationic exchange of Co^{+2} for Fe^{+2} in Fe_3O_4 ($FeFe_2O_4$) MNPs, the blocking temperature and the coercivity of the resulting $CoFe_2O_4$ MNPs increased significantly;[47] that is, the blocking temperature after Co^{+2} treatment of these 21-nm Fe_3O_4 MNPs increased to 310 K from 250 K, and the coercivity doubled. The authors suggested that a higher spin-orbit coupling at Co^{+2} sites led to an increased magnetic anisotropy and thus higher blocking temperature and coercivity. Cationic exchange is thus an effective tool for introducing alternative cations to produce various ferrite structures from Fe_3O_4 MNPs to develop properties geared for particular applications.

In some cases, the magnetic behavior of the nanoparticles can depend on the solvent used during their synthesis. Clavel *et al.* observed that Mn-doped ZnO MNPs were paramagnetic from both solvent systems used (benzyl alcohol or anisole/benzyl alcohol at 95/5%); however, Co-doped MNPs were ferromagnetic when benzyl alcohol was used, and antiferromagnetic when the anisole/benzyl alcohol solvent system was used.[101]

With only a few exceptions (e.g., $Zn_{0.4}Fe_{2.6}O_4$ MNPs), alloy nanoparticles such as FeCo generally exhibit high Ms values (e.g., 150–200 emu/g).[102,103] The enhancement

has been attributed to the absence of the non-ferromagnetic "oxygen" component found in many of the alternative structures. Therefore, numerous recent studies focused on such alloy-based MNPs. For example, FeCo nanocubes of body diagonal 175, 350, and 450 nm synthesized by liquid-phase reduction reaction showed an average Ms of 167 ± 4 emu/g.[18] Further, a reductive thermal decomposition method employed by Chaubey *et al.* afforded FeCo spheres having 10 and 20 nm diameters with a size-dependent Ms of 129 emu/g and 207 emu/g, respectively.[102] These authors also found an optimum molar ratio of Fe:Co (1.5:1) for which the Ms was at a maximum. In a separate study of MNPs having the form $Fe_{100-x}Co_x$, Chinnasamy *et al.* also observed a higher Ms for Fe-rich nanoparticles as compared to Co-rich nanoparticles.[42] Rellinghaus *et al.* found that upon annealing, the face-centered tetragonal-(*fct*) structured FePt MNPs exhibited a high coercivity (5000–7000 kOe).[104] The enhanced coercivity was attributed to the *fct* structure, while an also observed high blocking temperature was attributed to the high anisotropy constant, making FePt MNPs uniquely suitable for high-density data storage and hyperthermia applications.[105] Nanoparticles having the composition Fe_xPt_{100-x} (x = 70, 52, 48) synthesized by thermal decomposition and reduction exhibited blocking temperatures of 12 K for $Fe_{70}Pt_{30}$, 16.5 K for $Fe_{52}Pt_{48}$, and 30 K for $Fe_{48}Pt_{52}$ with diameters of 3.6, 3.1, and 3.8 nm, respectively. In evaluating the magnetic properties of FePt MNPs, Rellinghaus co-workers examined how the difference in atomic volumes between Fe and Pt causes a distortion of the *fcc* structure when it transforms to the *fct* structure.[104] The distortion in symmetry of the Fe_xPt_{100-x} MNPs varies with the Fe:Pt ratio and is responsible for the variance in magnetocrystalline anisotropy as a function of

composition. This variance in anisotropy then translates to the observed variance in blocking temperature in accord with Equation 1.1.

Another important MNP parameter that can be modulated by changes in composition is the Curie temperature (Tc), which is the temperature above which MNPs show zero magnetization. Overheating in hyperthermia applications can be avoided by using MNPs with a Curie temperature sufficiently low that they operate, not only as heating agents, but also as fuses.[71] During the past decade, several reports have focused on this aspect of "self-controlled" hyperthermia.[106] For example, when the aluminum content in MNPs having the formula $Y_3Fe_{5-x}Al_xO_{12}$ ($0 \leq x \leq 2$) was varied, the Curie temperature ranged from -40 to 280 °C. The composition was adjusted through cationic exchange, where the Fe^{+3} cations occupying the tetrahedral and octahedral sites were replaced by non-magnetic Al^{+3} cations, leading to a reduction in the saturation magnetization as the MNPs gained Al^{+3} content. The Tc for these MNPs reached room temperature when the Al^{+3} content was $1.5 < x < 1.8$.[107] A similar exchange of Sr^{+2} or Ti^{+4} in $La_{1-x}Sr_xMn_{1-y}Ti_yO_3$ MNPs led to a decrease in Tc from ~90 °C to ~20 °C; the Ti^{+4}-substituted $La_{1-x}Sr_xMn_{1-y}Ti_yO_3$ MNPs had higher values of Ms and sharper Tc transitions when compared to the Sr^{+2}-substituted $La_{1-x}Sr_xMn_{1-y}Ti_yO_3$ MNPs.[108] Another study by Miller *et al*. showed the importance of the phase of the material: variation in the composition of FeNi MNPs gave reduced values of Tc only for the γ-phase.[109] The $Fe_{73}Ni_{27}$ MNPs exhibited a Curie temperature of 550 °C in the bcc α-Fe phase and 120 °C in the γ-phase.

While composition provides an underlying definition of the magnetic behavior for these MNPs and directly affects the Ms and coercivity as shown in Table 1.6, the

underlying phenomena that allows for the compositional tuning of MNPs to modulate Tc are not as well understood and require additional research. The strategy described above for applying compositional optimization to help restrict the upper heating limit for hyperthermia treatments might also lead to additional applications for remotely initiated self-regulated heating by MNPs.

1.3.4 Effect of Shell-Core Architecture on Magnetic Properties

Nanoparticles are often coated with a selected material either (i) to make them biocompatible and stable in physiological fluids or (ii) to provide a modified surface that can be used for further functionalization, or (iii) to alter the magnetic properties of the core nanoparticle in a favorable manner.[110,111] The coating can be either non-magnetic or magnetic (antiferromagnetic or ferromagnetic or ferrimagnetic).[112] Regardless of the type of coating, there is usually some effect on the magnetic properties of the core. One effect is akin to the disordered spin layer that reduces the Ms of small nanoparticles (vide supra); since saturation magnetization is defined on a per gram basis, a non-magnetic coating (shell) will necessarily decrease its value. In the case of a magnetic coating, the core-shell interface interaction might lead to a change in anisotropy and a shift in the hysteresis loop. The shift of the hysteresis loop is "exchange bias" and it mainly arises due to interface coupling between two different types of layers (e.g., ferromagnetic and ferrimagnetic).[113,114] The discussion that follows focuses on the impact of various types of coatings on the magnetic properties of surface-modified MNPs.

A coating of silica (SiO_2) can transform a MNP by reducing problems associated with biocompatibility and offering the capacity to functionalize the surface of these nanomagnets.[19] Larumbe *et al.* evaluated the effect of SiO_2 coating on Fe_3O_4 MNPs and

found a reduced Ms and a lower coercivity, hence a lower specific absorption rate (SAR) for SiO_2-coated Fe_3O_4 MNPs as compared to analogous uncoated Fe_3O_4 nanoparticles.[21] The authors attributed this decrease in both magnetization and SAR to surface spin effects. Moreover, they found that the blocking temperature was diminished for the SiO_2-coated Fe_3O_4 MNPs. For thicker shells, the surface spin effects and the associated anisotropy constant were accentuated and led to a further reduction in magnetization and SAR. Other silica-coated ferrite nanoparticles ($MnFe_2O_4$, $CoFe_2O_4$, $NiFe_2O_4$) showed similar results, with a reduced Ms after coating with silica; however, the decrease in the coercivity varied with the composition of the core.[115,116] For example, for the same size and coating, Vestal *et al.* showed that the Ms decreased as expected, but the coercivity decreased by 10% for silica-coated $MnFe_2O_4$ MNPs and 1% for silica-coated $CoFe_2O_4$ MNPs. This difference is likely due to the difference in magnetocrystalline anisotropy of $MnFe_2O_4$ (0.056 J/cm^3) and $CoFe_2O_4$ (0.22 J/cm^3). The change in anisotropy, and thus coercivity, is more marked in the case of composites with a lesser core anisotropy. In contrast to most studies that show a reduced magnetization for nanoparticles coated with a non-magnetic layer, Woo *et al.* demonstrated a higher Ms for silica-coated and amine-functionalized Fe_3O_4 MNPs.[117] Although some of the results obtained in core-shell MNP research might seem counterintuitive, it is clear from the results obtained from MNPs with a ferrite core that this aspect of MNP design is an important parameter that can be used to tailor the magnetic properties of MNPs.

Noting the discussion above regarding hyperthermia, in the case of larger nanoparticles, a higher value of SAR (better MNP heating) depends on coercivity and Brownian losses. Consequently, although there may be no suitable alternative to coating

an MNP system with a magnetization-reducing coating for a specific application, we can nevertheless choose the core-coating combination with the highest coercivity (composite with the lowest coercivity reduction after coating). Like silica coatings, a diamagnetic/nonmagnetic polymer layer offers similar advantages and disadvantages: enhanced biocompatibility and functionality but reduced magnetic properties. The effect of an N-isopropylacrylamide (NIPAM) coating on the magnetic properties of Fe_3O_4 MNPs is listed as an example in Table 1.7.[52]

In the subsection above describing the influence of shape on magnetic properties, we examined how diverse shapes affect the relaxation of the protons surrounding them, leading to changes in the imaging contrast. MNPs coated with water-stable and biocompatible materials have excellent qualities for MRI applications, and efforts to synthesize a broad variety of core-shell MNPs and to optimize their effectiveness as contrast agents are ongoing.[118,119] The past decade has seen numerous studies evaluating the effect of the core as well as the coating on the relaxation of the surrounding protons for their use as MRI contrast agents.[120,121] Although the magnetic core provides the field that alters the relaxation of the surrounding protons, the thickness and chemical composition of the coating influences the relative distance and general strength of the MNP magnetic field with regard to these protons. As the thickness of the coating (e.g., silica or polyethylene glycol) increases, the relaxivity (r_2) decreases.[122,123] As we saw in the preceding subsection, core-shell composites that give reduced transverse relaxation times (T_2) or increased relaxivities (r_2) are more effective; therefore, the use of a thin coating will, in general, give a more effective contrast agent. However, in the case of a silica-coated Fe_3O_4 MNPs, Ye *et al.* noted that, due to their permeability to water, the

silica-coated Fe_3O_4 MNPs in their study exhibited a decreased longitudinal relaxivity (r_1), leading to a net increase in the r_2/r_1 ratio, an indicator of MRI efficiency.[123] For this experiment, their silica-coated Fe_3O_4 nanocomposite was ~21 and ~14 times more efficient than the commercially available iron oxide contrast agents, Feridex and Resovist, respectively. Thus, the nature of the magnetic core, the composition of the coating (and its permeability and hydrophilicity), and the thickness of the coating can be used to enhance the efficiency of MNPs in MRI applications.

The influence of the shell on the magnetic properties is more interesting and provides us a higher tuning opportunity when both the core and the shell are magnetic, and also when the shell is metallic and the core is magnetic. Choo *et al.* observed an interesting interfacial effect at 20 K when hexagonal close packed (*hcp*) Ni nanoparticles that were antiferromagnetic below 12 K were coated with a *fcc* Ni shell that was superparamagnetic up to 360 K.[49] The magnetization peaked at this temperature regardless of the external magnetic field. In the case of Cu-capped (1.5 nm thick) Co nanoparticles, the surface anisotropy was higher than that for uncapped Co nanoparticle cores 1.1–4.5 nm in diameter.[50] When 2.7 nm Co nanoparticles were coated with varying thicknesses of Pt (up to 0.7 nm), the blocking temperature increased dramatically from 16 K to 108 K.[50] The conclusion from this research is that capping MNP cores with a metal can increase the anisotropy and give a higher blocking temperature for core-shell MNPs. Such enhanced anisotropy characteristics have been attributed to the bonding of the d electrons of the core to the conduction band orbitals of the capping layer.[50]

Enhancing the coercivity and remanent magnetization by exchange coupling a hard phase (high coercivity) with a soft phase (low coercivity) has been successfully used

in multi-phase permanent magnets.[124,125] This basic idea, combined with pioneering research efforts, has paved the way for more recent studies focused on controlling the magnetic properties by varying the core-shell composition, shape, and dimensions. Zeng *et al.* synthesized an MNP designed with a hard FePt core (high coercivity) and a softer Fe_3O_4 shell (lower coercivity) and tuned the magnetic properties of the core-shell composite by varying the thickness of the shell.[112] Tailoring the magnetic properties by varying the thickness of the shell is experimentally simpler than modulating the MNP core phases.[126] For example, a prior study aimed at tuning the magnetic properties of MNPs was based on a combination of FePt and Fe_3Pt in the core and required the separate syntheses of FePt and Fe_3O_4 MNPs followed by annealing the defined mixture of MNPs with precise control. The same research group demonstrated that tailoring the magnetic properties of MNPs could be accomplished by varying the composition of the shell.[112] The researchers examined both the softer-than-FePt Fe_3O_4 shell and the harder-than-FePt $CoFe_2O_4$ shell. In addition to a smooth hysteresis curve that demonstrated effective exchange coupling between the core and the shell, the coercivity varied inversely as the volume ratio of shell/core in the case of Fe_3O_4 shell/FePt core NMPs and varied inversely with the thickness of the $CoFe_2O_4$ shell for the other set of NMPs.

As noted above, Fe_3O_4 MNPs hold promise for their use in biomedical applications. However, if the standard Ms of ~100 emu/g for these MNPs can be further enhanced, they would find use in an even broader array of applications. Considering that iron metal has a higher magnetization than Fe_2O_3 or Fe_3O_4, it would appear that this element might also have significant potential for MNP applications. Unfortunately, iron is highly susceptible to oxidation, which severely limits the use of metallic Fe

nanoparticles. However, Qiang *et al.* recently described the synthesis of a series of iron oxide-coated Fe core MNPs with coatings 2.5 nm thick and core diameters 2–100 nm; these oxidatively stable MNPs gave Ms values on the order of ~200 emu/g.[127] Furthermore, these unique MNPs are promising from an applications perspective because efficient and effective MRI contrast agents must have both high magnetization and elements that enhance the relaxation times of the protons in the surrounding environment.[22] Importantly, these Fe core-iron oxide shell nanoparticles, which consist of α-Fe at the core and γ-Fe_2O_3 or Fe_3O_4 as the shell, possesses both characteristics.[20]

We also noted in a preceding subsection that exchange bias (measured as a shifting of the hysteresis curve) occurs in the coupling of ferromagnetic and ferrimagnetic layers; this bias can also exist in ferrimagnetic layers and disordered spin layers.[53] Ong *et al.* compared Fe-Fe_3O_4 core-shell MNPs and Fe_3O_4 hollow-shell MNPs and found that because of interfacial spin interactions, there was a much higher exchange bias (1190 Oe) in the Fe-Fe_3O_4 core-shell MNP as compared to that observed in the hollow-shell MNP (133 Oe).[53] In case of hollow-shell MNP, the broken bonds on the inner surface induced a surface-spin disorder, giving a core-shell structure of disordered spins and Fe_3O_4 shell. Their studies demonstrated that the effect of the interfacial spin interactions was amplified in the case of a ferromagnetic core and ferrimagnetic shell when compared to a disordered spin core and Fe_3O_4 shell (ferrimagnetic shell alone). In contrast, Khurshid *et al.* reported an approximately 7-fold enhancement of exchange bias (~96 mT) in 18.7 nm hollow maghemite nanoparticles as compared to that (~17 mT) observed in 18.5 nm solid γ-Fe_2O_3 [[128]]. Additionally, the researchers attributed the higher T_B for the hollow γ-Fe_2O_3 (as compared to solid γ-Fe_2O_3) to the spin disorder enhancing the surface

anisotropy. This increase in surface anisotropy leading to higher blocking temperatures for hollow nanoparticles has been also illustrated for $NiFe_2O_4$ (solid $Ni_{33}Fe_{67}$ core/$NiFe_2O_4$ shell and $NiFe_2O_4$ shell only).[129] These studies highlight the importance of surface spin disorder, and hollow nanoparticles provide another tool for tuning the magnetic properties.

The interplay of the saturation magnetization, coercivity, magnetic anisotropy energy barrier (reflected in the anisotropy constant, K), and viscosity of the suspension medium is critical for MRI and hyperthermia applications.[61] Since the anisotropy constant reflects an intrinsic property of the material used to produce the nanoparticle, composition is also a known parameter that can be used to tune the SAR/SLP. However, as further discussed in this section, tuning K by varying the composition is challenging and an exchange-coupled magnet has proven more effective for developing tunable magnetic properties and optimizing application efficiency. For hyperthermia applications, an SAR of 1 kW/g is necessary at 100 kHz and 20 mT (human-compatible conditions). Meffre *et al.* have reported a high SAR of 415 W/g at 96 kHz and 20 mT for 13.6 nm iron carbide@iron nanoparticles.[62] After confirming the presence of exchange-coupling between the shell and the core of their core-shell nanoparticles by a smooth hysteresis curve, Lee *et al.*[130] demonstrated that their composite particles exhibited a significant enhancement in SLP (1000 to 4000 W/g) as compared to single-component MNPs (100 to 450 W/g) and commercial Ferridex nanoparticles (115 W/g). A variety of distinct combinations for the assembly of core-shell MNPs continue to be synthesized and characterized; these studies highlight the experimental capacity to optimize magnetic properties such as magnetization and coercivity by fine-tuning the composition and

thickness of the core-shell architectures. Some of these studies are summarized in Table 1.7. Recently, Noh *et al.* synthesized cubes of $CoFe_2O_4$-coated $Zn_{0.4}Fe_{2.6}O_4$ cores and observed a smooth hysteresis curve and a 14-fold increase in coercivity as compared to the core alone.[31] This increase translated into a dramatically higher SAR for the shell-core MNPs (10600 W/g) when compared to that of MNPs composed of just the core (4060 W/g).

Table 1.7 Influence of Various Types of Coatings on the Properties of Magnetic Nanoparticles

Reference	**Nanoparticle (Shell@Core)**	**Size (nm)**	**Ms (emu/g)**	**Coercivity (Oe)**	**T_B (K)**	**SAR/SLP (W/g)**
Larumbe, S. *et al.*[21]	Fe_3O_4 SiO_2@Fe_3O_4	5 7.5	72 37	0 0	160 120	1.5 1.08 At 340 kHz and 170–340 Oe
Shamim, N. *et al.*[52]	Fe_3O_4 PNIPAM@ Fe_3O_4	9.3 12	75.7 51.6	1.1 5		
Ebbing, S. *et al.*[46]	Co Pt@Co	2.7 3.0			16 108	
Yang, S. . *et al.*[131]	$MnFe_2O_4$ Ni@$MnFe_2O_4$	200 202	74 30	89 89		
Zeng, H. *et al.*[54]	FePt Fe_3O_4@FePt	4 6	1040 950	5500 13500		
Lee, J. *et al.*[130]	$CoFe_2O_4$ $MnFe_2O_4$ $MnFe_2O_4$@ $CoFe_2O_4$	9 15 12				450 450 2250At 500 kHz and 37.3 kA/m
Noh, S. *et al.*[31]	$Zn_{0.4}Fe_{2.6}O_4$ $CoFe_2O_4$shell@ $Zn_{0.4}Fe_{2.6}O_4$	50 60	190 130	140 1900	320	4060 10600 At 500 kHz and 37.4 kA/m

As we have discussed earlier, a "domain wall" separates the domains, and its thickness depends on the anisotropy of the material. Recent reports have noted that the transition between the hard and soft phases is most effective (i.e., characterized by a smooth transition curve) when the shell thickness is about twice the width of the domain

wall (e.g., ~20 nm).[31,126] A single, smooth hysteresis curve for a multi-layered nanocomposite system is thus an indication of a near-perfect coupling at the interface. As we remarked earlier, for MNP interactions within an alternating magnetic field, magnetic nanoparticles store and dissipate energy via t_N, t_B, and hysteresis losses. The shell-core architecture (composition and dimensions) therefore provides yet another avenue for maximizing coercivity (and thus SAR/SLP), providing a route for developing even more effective hyperthermia treatments.

In this review, we have focused on the parameters that define and hence create possibilities of tuning and optimizing magnetic behavior of MNPs. Additionally, there are numerous reports of research that can harness the collective properties of nanoparticles[132] including the effect of multi-core assembly[133] concentration/dipolar interactions,[134] and clustering[132,135] and may provide alternatives for tuning the magnetic properties for more effective applications. These, however, warrant a separate review in itself.

1.4. Conclusion

The various studies summarized in this brief review collectively illustrate the challenges facing efforts to provide a single algorithm for optimizing the properties of MNPs for selected applications.

1.5. Motivation for My Research

We have seen how the broad dependence of the magnetic properties on multiple interlinked factors is especially daunting. Nevertheless, from this complex network of parameters, we can highlight several important correlations between certain magnetic

properties of MNPs (saturation magnetization, coercivity, blocking temperature, and relaxation time) and physical parameters (size, shape, composition, and shell-core architecture) that can be selectively and judiciously modulated.

As we have seen above, the effect of shape on the magnetic properties of the nanoparticles continues to challenge the research community. For applications such as sensing, geometries other than spherical are preferred; for example, a cubic shape offers a higher contact area and might lead to higher sensitivity. When the research endeavors outlined in this dissertation were initiated, there existed a limited amount of comparison data for MNPs less than 25 nm, but the data for sizes higher than 100 nm were sorely lacking. This gap in the available data motivated a comparison of the magnetic properties of nanoparticles of different shapes at same volume and same diameter. To address this concern, I chose to focus on spherical and cubic MNPs of Fe_3O_4. Additionally, to functionalize the nanoparticles for their use in sensing, it was necessary to coat them with a thin protective layer, retaining the cubic shape so as to maintain the structural advantage of higher contact area. This objective was accomplished using a silica coating and amine functionalization for FeCo nanocubes of high saturation magnetization, while retaining their cubic shape.

To broaden my research portfolio, I also pursued a set of projects that involved the blending of MNP synthesis with biosensing. Research in magnetic biosensing is mainly focused on the use of already-synthesized MNPs in sample capture, cleanup, and concentration, and as labels for sensitive biomolecule detection.[136] The application of giant magnetoresistive (GMR) sensors and MNP labels to bioassays and diagnostics was first suggested by Baselt *et al.* in 1998,[137] and then Shieh & Ackley in 2000.[138] This

approach is attractive because of the solid-state and potentially low-cost nature of the sensors, and the absence of concerns associated with photobleaching, scattering, and fouling. Research groups at the University of Minnesota[139-141] and at Stanford University[142-144] have recently reported micrometer-scale magnetic sensors for ultrasensitive protein detection in complex samples.

Conventional enzyme-linked immunosorbent assays (ELISAs) rely on modification of the substrate to form a detectable product that absorbs, fluorescences, or luminescences or enzymatically forms an insoluble precipitate.[145,146] Similar to the redox chemistry upon which black and white photography has been based, enzyme-mediated formation of silver nanoparticles has been demonstrated.[147-148] Several studies have shown that alkaline phosphatase (AP) can produce metallic silver by dephosphorylation of a substrate (e.g., L-ascorbic-2-phosphate,[148] p-aminophenyl phosphate,[149] and 3-indoxyl phosphate[150]) that then acts as a reducing agent. When this process was first brought to my attention, this conversion appeared to be a potential method of using the enzyme-mediated synthesis of nanoparticles to form magnetic nanoparticles in a sensing application. This new concept and its success could offer a useful approach to magnetic sensing in which the magnetic reporter can be enzymatically synthesized *in situ*. This approach is inexpensive and would circumvent the substantial mass-transfer concerns associated with pre-synthesized magnetic reporter particles while preserving the advantages of magnetic sensing, including the use of inexpensive solid-state detectors and the elimination of optical challenges such as turbidity and photobleaching.

Both *in situ* and *ex situ* synthesized MNPs demonstrate the potential for structuring assays that produce a magnetic signal in response to the presence of a specific

enzymatic response. Conversely, these phenomena point to the possible development of a diametrically opposite system in which the magnetic component loses its magnetism through an enzymatically-mediated reduction process. We therefore also focused on the reduction of magnetic Fe_3O_4 nanoparticles to yield a non-magnetic precipitate.

Therefore, the research presented in my dissertation has been focused on two primary goals: (1) to evaluate and compare the effect of shape and shape-related factors on the magnetic properties of MNPs and (2) to develop the enzymatically-mediated synthesis or disappearance of MNPs that can be potentially used in a sensing assay.

1.6 Research Outline

This dissertation is organized into six chapters. The present chapter presents an overview of the magnetic properties that are important and tunable in most circumstances. The chapter then outlines the motivation for my research.

Each subsequent chapter is an independent project in which I have provided background information, experimental details, results/discussion, and conclusions. Chapter 2 describes the synthesis, silica-coating, and amine-functionalization of FeCo nanocubes of high saturation magnetization, with these modifications being made while retaining the cubic shape. Chapter 3 describes the synthesis, characterization, and comparison of spherical and cubic Fe_3O_4 MNPs of varying diameters to create sphere-cube pairs of matching volumes and diameters. Chapter 4 focuses on the enzymatic conversion of MNPs to a non-magnetic precipitate, and in the process providing an indication of a "loss of signal" in a sensing device as a means of determining the presence of an analyte. Chapter 5 describes the enzymatic synthesis of MNPs of $Fe_xGd_yO_z$ and

$Fe_xHo_yO_z$, which is a novel approach to magnetic sensing in which the magnetic reporter is enzymatically synthesized *in situ* during part of the assay. Alkaline phosphatase is the enzyme used in both conversion and synthesis of MNPs in Chapters 4 and 5. Chapter 6 summarizes the major conclusions of each chapter.

1.7 References

(1) Frey, N. A.; Peng, S.; Cheng, K.; Sun, S. *Chem. Soc. Rev.* **2009**, *38*, 2532–2542.

(2) Colombo, M.; Carregal-Romero, S.; Casula, M. F.; Gutierez, L.; Morales, M. P.; Bohm, I. B.; Heverhagen, J. T.; D., P.; Parak, W. J. *Chem. Soc. Rev.* **2012**, *41*, 4306–4334.

(3) Singamaneni, S.; Bliznyuk, V. N.; Binek, C.; Tsymbal, E. Y. *J. Mater. Chem.* **2011**, *21*, 16819–16845.

(4) Lu, A. H.; Salabas, E. L.; Schuth, F. *Angew. Chem. Int. Ed.* **2007**, *46*, 1222–1244.

(5) Koh, I.; Josephson, L. **2009**, *9*, 8130–8145.

(6) Arruebo, M.; Fernandez-Pacheco, R.; Ibarra, M.; Santamaria, J. *Nanotoday* **2007**, *2*, 22-32.

(7) Kami, D.; Takeda, S.; Itakura, Y.; Gojo, S.; Watanabe, M.; Toyoda, M. *Int. J. Mol. Sci.* **2011**, *12*, 3705–3722.

(8) Dobson, J. *Drug Dev. Res.* **2006**, *67*, 55–60.

(9) Gazeau, F.; Levy, M.; Wilhelm, C. *Nanomed.* **2008**, *3*, 831–844.

(10) Gupta, A. K. G., M. *Biomater.* **2005**, *26*, 3995–4021.

(11) Willard, M. A.; Kurihara, L. K.; Carpenter, E. E.; Calvin, S.; Harris, V. G. *Int. Mater. Rev.* **2004**, *49*, 124–170.

(12) Thiesen, B.; Jordan, A. *Int. J. Hyperthermia* **2008**, *24*, 467–474.

(13) Neuberger, T.; Schopf, B.; Hofmann, H.; Hofmann, M.; Rechenberg, B. *J. Magn. Magn. Mater.* **2005**, *293*, 483–496.

(14) Huang, S.; Juang, R. *J. Nanopart. Res.* **2011**, *13*, 4411–4430.

(15) Lin, C.-R. C., R-K.; Wang, J-S.; Sung, T-W. *J. Appl. Phys.* **2006**, *99*, 08N710/711–714.

(16) Decuzzi, P.; Ferrari, M. *Biomater.* **2006**, *27*, 5307–5317.

(17) Decuzzi, P.; Pasqualini, R.; Arap, W.; Ferrari, M. *Pharm. Res.* **2009**, *26*, 235–243.

(18) Kolhatkar, A. G.; Nekrashevich, I.; Litvinov, D.; Willson, R. C.; Lee, T. R. *Chem. Mater.* **2013**, *25*, 1092–1097.

(19) Rittikulsittichai, S.; Singhana, B.; Bryan, W. W.; Sarangi, S.; Jamison, A. C.; Brazdeikis, A.; Lee, T. R. *RSC Adv.* 2013, 3, 7838–7849.

(20) Kuhn, L.; Bojesen, A.; Timmermann, L.; Fauth, K.; Goering, E.; Johnson, E.; Nielson, M. M.; Morup, S. *J. Magn Magn. Mater.* **2004**, *272*, 1485–1486 .

(21) Larumbe, S.; Gomez-Polo, C.; Perez-Landazabal, J.; Pastor, J. M. J. *Phys.:Condens. Matter* **2012**, *24*, 1–6.

(22) Maity, D.; Zoppellaro, G.; Sedenkova, V.; Tucek, J.; Safarova, K.; Polakova, K.; Tomankova, K.; Diwoky, C.; Stollberger, R.; Machala, L.; Zboril, R. *Chem. Commun.* **2012**, *48*, 11398–11400.

(23) Pereira, C.; Pereira, A. M.; Fernandes, C.; Rocha, M.; Mendes, R.; Fernandez-Garcia, M.; Guedes, A.; Tavares, P. B.; Greneche, J.-M.; Araujo, J. P.; Freire, C. *Chem. Mater.* **2012**, *24*, 1496–1504.

(24) Caruntu, D.; Caruntu, G.; O'Connor, C. J. J. *Phys. D: Appl. Phys.* **2007**, *40*, 5801–5809.

(25) Khandhar, A. P.; Ferguson, M. R.; Simon, J. A.; Krishnan, K. M. *J. Biomed. Mater. Res. A* **2011**, *100A*, 728–737.

(26) Peddis, D.; Mansilla, M. V.; Morup, S.; Cannas, C.; Musinu, A.; Piccaluga, G.; D'Orazio, F.; Lucari, F.; Fiorani, D. *J. Phys. Chem. B* **2008**, *112*, 5807–8513.

(27) Han, T. C.; Tsai, M. R.; Wei, C. Y. *J. Appl. Phys.* **2011**, *109*, 07B517/511–513.

(28) Markovich, V.; Fita, I.; Wisniewski, A.; Puzniak, R.; Mogilyansky, D.; Iwanowski, P.; Dluzewski, P.; Gorodetsky, G. *J. Phys. Chem. C* **2012**, *116*, 435–447.

(29) Markovich, V.; Fita, I.; Wisniewski, A.; Mogilyansky, D.; Puzniak, R.; Titelman, L.; Martin, C.; Gorodetsky, G. *Phys. Rev. B* **2010**, *81*, 094428-094421–094428-094411.

(30) Muller, R.; Dutz, S.; Neeb, A.; Cato, A.; Zeisberger, M. *J. Magn Magn. Mater.* **2013**, *328*, 80–85.

(31) Noh, S. H.; Na, W.; Jang, J. T.; Lee, J. H.; Lee, E. J.; Moon, S. H.; Lim, Y.; Shin, J. S.; Cheon, J. *Nano Lett.* **2012**, *12*, 3716–3721.

(32) Guardia, P.; Labarta, A.; Battle, X. *J. Phys. Chem. C* **2011**, *115*, 390–396.

(33) Montferrand, C.; Hu, L.; Milosevic, I.; Russier, V.; Bonnin, D.; Motte, L.; Brioude, A.; Lalatonne, Y. *Acta Biomater.* **2013**, *9*, 6150–6157.

(34) He, X.; Shi, H. *Particuology* **2012**, *10*, 497–502.

(35) Song, Q.; Zhang, Z. J. *J. Am. Chem. Soc.* **2004**, *126*, 6164–6168.

(36) Salazar-Alvarez, G.; Qin, J.; Sepelak, V.; Bergmann, I.; Vasilakaki, M.; Trohidou, K. N.; Ardisson, J. D.; Macedo, W. A. A.; Mikhaylova, M.; Muhammed, M.; Baro, M. D.; Nogues, J. *J. Am. Chem. Soc.* **2008**, *130*, 13234–13239.

(37) Leem, G.; Sarangi, S.; Zhang, S.; Rusakova, I.; Brazdeikis, A.; Litvinov, D.; Lee, T. R. *Cryst. Growth Des.* **2009**, *9*, 32–34.

(38) Zhen, G.; Muir, B. W.; Moffat, B. A.; Harbour, P.; Murray, K. S.; Moubaraki, B.; Suzuki, K.; Madsen, I.; Agron-Olshina, N.; Waddington, L.; Mulvaney, P.; Hartley, P. G. *J. Phys. Chem. C* **2011**, *115*, 327–334.

(39) Comesana-Hermo, M.; Ciuculescu, D.; Li, Z.; Stienen, S.; Spasova, M.; Farle, M.; Amiens, C. *J. Mater. Chem.* **2012**, *22*, 8043–8047.

(40) Chou, S.-W.; Zhu, C.-L.; Neeleshwar, S.; Chen, C.-L.; Chen, Y.-Y.; Chen, C.-C. *Chem. Mater.* **2009**, *21*, 4955–4961.

(41) Lu, H. M.; Zheng, W. T.; Jiang, Q. J. *Phys. D: Appl. Phys.* **2007**, *40*, 320–325.

(42) Chinnasamy, C.; Herr, J.; Pai, R.; Cui, B.; Li, W.; Liu, J. *J. Appl. Phys.* **2012**, *111*, 07B539/531–533.

(43) Gabal, M. A.; Angari, A. Y. M.; Kadi, M. W. *Polyhedron* **2011**, *30*, 1185–1190.

(44) Larumbe, S.; Gomez-Polo, C.; Perez-Landazabal, J.; Garcia-Prieto, A.; Alonso, J.; Fdez-Gubieda, L.; Cordero, D. G., J. *J. Nanosci. Nanotech.* **2012**, *12*, 2652–2660.

(45) Turtelli, R. S.; Atif, M.; Mehmood, N.; Kubel, F.; Biernacka, K.; Linert, W.; Grossinger, R.; Kapusta, C.; Sikora, M. *Mater. Chem. Phys.* **2012**, *132*, 832–838.

(46) Ebbing, A.; Hellwig, O.; Agudo, L.; Eggeler, G.; Petracic, O. *Phys. Rev. B* **2011**, *84*, 012405/012401–012404.

(47) Sytnyk, M.; Kirchschlager, R.; Bodnarchuk, M. I.; Primetzhofer, D.; Kriegner, D.; Enser, H.; Stangl, J.; Bauer, P.; Voith, M.; Hassel, A. W.; Krumeich, F.; Ludwig, F.; Meingast, A.; Kothleitner, G.; Kovalenko, M.; Heiss, W. *Nano. Lett.* **2013**, *13*, 586–593.

(48) Deng, H.; Li, X.; Peng, Q.; Wang, X.; Chen, J.; Li, Y. *Angew. Chem. Int. Ed.* **2005**, *44*, 2782–2785.

(49) Choo, S.; Lee, K.; Jo, Y.; Yoon, S.; Choi, J.; Kim, J.; Park, J.; Lee, J.; Jung, M. J. *Nanosci. Nanotech.* **2011**, *11*, 6126–6130.

(50) Luis, F.; Bartolome, F.; Petroff, F.; Bartolome, J.; Garcia, M.; Deranlot, C.; Jaffres, H.; Martinez, M.; Bencok, P.; Wilhelm, F.; Rogalev, A.; Brookes, N. *Europhys. Lett.* **2006**, *76*, 142–148.

(51) Singh, V.; Srinivas, V.; Ranot, M.; Angappane, S.; Park, J.-G. *Phys. Rev. B* **2010**, *82*, 054417/054411–054419.

(52) Shamim, N.; Hong, L.; Hidajat, K.; Uddin, M. *Colloids Surf. B* **2007**, *55*, 51–58.

(53) Ong, Q. K.; Wei, A.; Lin, X.-M. *Phys. Rev. B* **2009**, *80*, 134418/134411–134416.

(54) Zeng, H.; Li, J.; Wang, Z. L.; Liu, J. P.; Sun, S. *Nano Lett.* **2004**, *4*, 187–190.

(55) Atkins, P. W. *Physical Chemistry*; W. H. Freeman and Company: New York, NY, USA, 1994.

(56) Gignoux, D. *Phenomenology of Magnetism at the Macroscopic Scale;* Springer: New York, NY, USA, 2005.

(57) Jeong, U.; Teng, X.; Wang, Y.; Yang, H.; Xia, Y. *Adv. Mater.* **2007**, *19*, 33–60.

(58) Knobel, M.; Nunes, W. C.; Socolovsky, L. M.; Biasi, E.; Vargas, J. M.; Denardin, J. C. J. *Nanosci. Nanotech.* **2008**, *8*, 2836–2857.

(59) Hansen, M. F.; Morup, S. *J. Magn Magn. Mater.* **1999**, *203*, 214–216.

(60) Hubert, A.; Schafer, R. *Magnetic domains: The analysis of magnetic microstructures* Springer-Verlag Berlin Heidelberg: New York, NY, USA, 2000.

(61) Kittel, C. *Reviews of Modern Physics* **1949**, *21*, 541–583.

(62) Craik, D. J.; McIntyre, D. A. *Proc. R. Soc. A, Mathematical and Physical Sciences* **1967**, *302*, 99–112.

(63) Krishnan, K. M. *IEEE Trans. Magn.* **2010**, *46*, 2523–2558.

(64) Skumeyev, V.; Stoyanov, S.; Zhang, Y.; Hadjipanayis, G.; Givord, D.; Nogues, J. *Nature* **2003**, *423*, 850–853.

(65) Jun, Y. W.; Seo, J. W.; Cheon, J. *Acc. Chem. Res.* **2008**, *41*, 179–189.

(66) Guardia, P.; Batlle-Brugal, B.; Roca, A.; Iglesias, O.; Morales, M.; Serna, C. J.; Labarta, A.; Batlle, X. *J. Magn. Magn. Mater.* **2007**, *316*, e756–758.

(67) Nagesha, D. K.; Plouffe, B. D.; Phan, M.; Lewis, L. H.; Sridhar, S.; Murthy, S. *J. Appl. Phys.* **2009**, *105*, 07B317/311–313.

(68) Laurent, S.; Dutz, S.; Hafeli, U. O.; Mahmoudi, M. *Adv. Coll. Interface Sci.* **2011**, *166*, 8–23.

(69) Salazar, J. S.; Perez, L.; Abril, O.; Phuoc, L. T.; Ihiawakrim, D.; Vazquez, M.; Greneche, J.; Begin-Colin, S.; Pourroy, G. *Chem. Mater.* **2011**, *23*, 1379–1386.

(70) Demortiere, A.; Panissod, P.; Pichon, B. P.; Pourroy, G.; Guillon, D.; Donnio, B.; Begin-Colin, S. *Nanoscale* **2011**, *3*, 225–232.

(71) Mornet, S.; Vasseur, S.; Grasset, F.; Duguet, E. *J. Mater. Chem.* **2004**, *14*, 2161–2175.

(72) Guardia, P.; Corato, R.; Lartigue, L.; Wilhelm, C.; Espinosa, A.; Garcia-Hernandez, M.; Gazeau, F.; Manna, L.; Pellegrino, T. *ACS Nano* **2012**, *6*, 3080–3091.

(73) Jang, J.-t.; Nah, H.; Lee, J.-H.; Moon, S. H.; Kim, M. G.; Cheon, J. *Angew. Chem. Int. Ed.* **2009**, *48*, 1234 –1238.

(74) Chung, S. H.; Hoffmann, A.; Bader, S. D.; Liu, C.; Kay, B.; Makowski, L.; Chen, L. *Appl. Phys. Lett.* **2004**, *85*, 2971–2973.

(75) Fortin, J.-P.; Wilhelm, C.; Servais, J.; Menager, C.; Bacri, J.-C.; Gazeau, F. *J. Am. Chem. Soc.* **2007**, *129*, 2628–2635.

(76) Jeun, M.; Lee, S.; Kang, J.; Tomitaka, A.; Kang, K.; Kim, Y.; Takemura, Y.; Chung, K.; Kwak, J.; Bae, S. *Appl. Phys. Lett.* **2012**, *100*, 092406/092401–092404.

(77) Lartigue, L.; Innocenti, C.; Kalaivani, T.; Awwad, A.; Sanchez, D. M. d. M.; Guari, Y.; Larionova, J.; Guerin, C.; Montero, J.-L. G.; Barragan-Montero, V.; Arosio, P.; Lascialfari, A.; Gatteschi, D.; Sangregorio, C. *J. Am. Chem. Soc.* **2011**, *133*, 10459–10472.

(78) Gonzales-Weimuller, M.; Zaisberger, M.; Krishnan, K. M. *J. Magn. Magn. Mater.* **2009**, *321*, 1847–1950.

(79) Sarangi, S.; Rittikulsittichai, S.; Cervadoro, A.; Jamison, A. C.; Decuzzi, P.; Lee, T. R.; Brazdeikis, A. J. In *Appl. Phys. Lett.* (Submitted).

(80) Carrey, J. M., B.; Respaud, M. *J. Appl. Phys.* **2011**, *109*, 083917–083921.

(81) Bujan-Nunez, M. C.; Fontaina-Troitino, N.; Vazquez-Vazquez, C.; Lopez-Quintela, M. A.; Pineiro, Y.; Serantes, D.; Baldomir, D.; Rivas, J. *J. Non-Cryst. Solids* **2008**, *354*, 5222–5223.

(82) Rosensweig, R. E. *J. Magn. Magn. Mater.* **2002**, *252*, 370–374.

(83) Carrey, J.; Mehdaoui, B.; Respaud, M. *J. Appl. Phys.* **2011**, *109*, 083917–083921.

(84) Koseoglu, Y.; Kavas, H. *J. Nanosci. Nanotech.* **2008**, *8*, 584–590.

(85) Gao, G.; Liu, X.; Shi, R.; Zhou, K.; Shi, Y.; Ma, R.; Takayama-Muromachi, E.; Qiu, G. *Cryst. Growth Des.* **2010**, *10*, 2888–2894.

(86) Yan, M.; Fresnais, J.; Berret, J. F. *Soft Matter* **2010**, *6*, 1997–2005.

(87) Wu, C.-G.; Lin, H. L.; Shau, N.-L. *J. Solid State Electrochem.* **2006**, *10*, 198–202.

(88) Srikala, D.; Singh, V. N.; Banerjee, A.; Mehta, B. R.; Patnaik, S. *J. Nanosci. Nanotechnol.* **2009**, *9*, 5627–5632.

(89) Roca, A. G.; Costo, R.; Rebolledo, A. F.; Veintemillas, S.; Tartaj, P.; Gonzalez-Carreno, T.; Morales, M. P.; Serna, C. J. *J. Phys. D: Appl. Phys.* **2009**, *42*, 1–11.

(90) Schladt, T. D.; Ibrahim, S.; Schneider, K.; Tahir, M. N.; Natalio, F.; Ament, I.; Becker, J.; Jochum, F. D.; Weber, S.; Kohler, O.; Theato, P.; Schreiber, L. M.; Sonnichsen, C.; Schroder, H. C.; Muller, W. E. G.; Tremel, W. *Angew. Chem. Int. Ed.* **2010**, *49*, 3976–3980.

(91) Na, H. B.; Song, I. C.; Hyeon, T. *Adv. Mater.* **2009**, *21*, 2133–2148.

(92) Joshi, H. M.; Lin, Y. P.; Aslam, M.; Prasad, P. V.; Schultz-Sikma, E.; Edelman, R.; Meade, T.; Dravid, V. P. *J. Phys. Chem. C* **2009**, *113*, 17761–17767.

(93) Caravan, P.; Farrar, C. T.; Frullano, L.; Uppal, R. *Contrast Media Mol. Imaging* **2009**, *4*, 89–100.

(94) Jun, Y. W.; Lee, J. H.; Cheon, J. *Angew. Chem. Int. Ed.* **2008**, *47*, 5122–5135.

(95) Lee, N.; Choi, Y.; Lee, Y.; Park, M.; Moon, W. K.; Choi, S. H.; Hyeon, T. *Nano Lett.* **2012**, *12*, 3127–3131.

(96) Williams, A. R.; Moruzzi, V. L.; Gelatt, C. D.; Kubler, J.; Schwarz, K. *J. Appl. Phys.* **1982**, *53*, 2019–2023.

(97) West, A. *Basic Solid State Chemistry*; John Wiley & Sons, Ltd.: Chichester, West Sussex, UK, 1999.

(98) Lee, J.H.; Huh, Y.-M.; Jun, Y.-W.; Seo, J.-W.; Jang, J.-T.; Song, H.-T.; Kim, S.; Cho, E.-J.; Yoon, H.G.; Suh, J.-S.; Cheon, J. *Nat. Med.* **2006**, *13*, 95–99.

(99) Gabal, M. A.; Bayoumy, W. A. *Polyhedron* **2010**, *29*, 2569–2573.

(100) Fantechi, E.; Campo, G.; Carta, D.; Corrias, A.; Fernandez, C.; Gatteschi, D.; Innocenti, C.; Pineider, F.; Rugi, F.; Sangregorio, C. *J. Phys. Chem. C* **2012**, *116*, 8261–8270.

(101) Clavel, G.; Willinger, M.; Zitoun, D.; Pinna, N. *Adv. Funct. Mater.* **2007**, *17*, 3159–3169.

(102) Chaubey, G. S.; Barcena, C.; Poudyal, N.; Rong, C.; Gao, J.; Sun, S.; Liu, J. P. *J. Am. Chem. Soc.* **2007**, *129*, 7214–7215.

(103) Zhang, K.; Amponsah, O.; Arslan, M.; Holloway, T.; Cao, W.; Pradhan, A. K. *J. Appl. Phys.* **2012**, *111*, 07B525/521–523.

(104) Rellinghaus, B.; Stappert, S.; Acet, M.; Wassermann, E. *J. Magn. Magn. Mater.* **2003**, *266*, 142–154.

(105) Iwamoto, T.; Matsumoto, K.; Matsushita, T.; Inokuchi, M.; Toshima, N. *J. Colloid Interface Sci.* **2009**, *336*, 879–888.

(106) Pollert, E.; Knizek, K.; Marysko, M.; Kaspar, P.; Vasseur, S.; Duguet, E. *J. Magn. Magn. Mater.* **2007**, *316*, 122–125.

(107) Grasset, F.; Mornet, S.; Demourgues, A.; Portier, J.; Bonnet, J.; Vekris, A.; Duguet, E. *J. Magn. Magn. Mater.* **2001**, *234*, 409–418.

(108) Phuc, N. X.; Hieu, N. T.; Le, N. T. H.; Manh, D. H.; Tuan, N. A.; Hong, L. V.; Tuong, L. T. C. J. *Korean Phys. Soc.* **2008**, *52*, 1492–1495.

(109) Miller, K. J.; Sofman, M.; McNerny, K.; McHenry, M. E. *J. Appl. Phys.* **2010**, *107*, 09A305/301–303.

(110) Berry, C.C. *J. Phys. D: Appl. Phys.* **2009**, *42*, 1–9.

(111) Cole, A.J.; Yang, V. C.; David, A. E. *Trends Biotechnol.* **2011**, *29*, 323–332.

(112) Zeng, H.; Sun, S. *Appl. Phys. Lett.* **2004**, *85*, 792–794.

(113) Iglesias, O.; Labarta, A.; Battle, X. *J. Nanosci. Nanotech.* **2008**, *8*, 2761–2780.

(114) Hudak, O.; Hudak, M. *Adv. Mater. Sci. Eng.* **2010**, *2010*, 1–6.

(115) Larumbe, S.; Perez-Landazabal, J. I.; Pastor, J. M.; Gomez-Polo, C. *J. Appl. Phys.* **2012**, *111*, 103911/103911–103918.

(116) Vestal, C. R.; Zhang, J. Z. *Nano Lett.* **2003**, *3*, 1739–1743.

(117) Woo, K.; Hong, J.; Ahn, J.-P. *J. Magn. Magn. Mater.* **2005**, *293*, 177–181.

(118) Feng, B.; Hong, R. Y.; Wang, L. S.; Guo, L.; Li, H. Z.; Ding, J.; Zheng, Y.; Wei, D. G. *Coll. Surf. A* **2008**, *328*, 52–59.

(119) Hong, R. Y.; Feng, B.; Chen, L. L.; Liu, G. H.; Li, H. Z.; Zheng, Y.; Wei, D. G. *Biochem. Eng. J.* **2008**, *42*, 290–300.

(120) Bulte, J. W.; Kraitchman, D. L. *NMR Biomed.* **2004**, *17*, 484–499.

(121) Wang, J. X.; Hussain, S.; Krestin, G. *Eur. Radiol.* **2001**, *11*, 2319–2331.

(122) LaConte, L. E.; Nitin, N.; Zurkiya, O.; Caruntu, D.; O'Connor, C.; Hu, X.; Bao, G. J. *Magn. Reson. Imaging* **2007**, *26*, 1634–1641.

(123) Ye, F.; Laurent, S.; Fornara, A.; Astolfi, L.; Qin, J.; Roch, A.; Martini, A.; Toprak, M. S.; Muller, R. N.; Muhammed, M. *Contrast Media Mol. Imaging* **2012**, *7*, 460–468.

(124) Skomski, R.; Coey, J. M. D. *Phys. Rev. B* **1993**, *48*, 15812–15816.

(125) Fullerton, E. E.; Jiang, J. S.; Bader, S. D. *J. Magn. Magn. Mater.* **1999**, *200*, 392–404.

(126) Zeng, H.; Li, J.; Liu, J. P.; Wang, Z. L.; Sun, S. *Nature* **2002**, *420*, 395–398.

(127) Qiang, Y.; Antony, J.; Sharma, A.; Nutting, J.; Sikes, D.; Meyer, D. *J. Nanopart. Res.* **2006**, *8*, 489–496.

(128) Khurshid, H.; Li, W.; Phan, M.-H.; Mukherjee, P.; Hadjipanayis, G. C.; Srikanth, H. *Appl. Phys. Lett.* **2012**, *101*, 022401–022405.

(129) Jaffari, G.H.; Ceylan, A.; Ni, C.; Shah, S. I. *J. Appl. Phys.* **2010**, *107*, 013910–013917.

(130) Lee, J.H.; Jang, J.T.; Choi, J.S.; Moon, S. H.; Noh, S.H.; Kim, J.W.; Kim, J.G.; Kim, I.S.; Park, K. I.; Cheon, J. *Nat. Nanotechnol.* **2011**, *6*, 418–422.

(131) Yang, S.C.; Ahn, C.W.; Park, C.S.; Yang, Y.; Viehland, D.; Priya, S. *J. Mater. Sci.* **2010**, *45*, 1419–1424.

(132) Ge, J.; Hu, Y.; Biasini, M.; Beyermann, W. P.; Yin, Y. *Angew. Chem., Int. Ed.* **2007**, *46*, 4342–4345.

(133) Lartigue, L.; Hugounenq, P.; Alloyeau, D.; Clarke, S. P.; Levy, M.; Bacri, J.-C.; Bazzi, R.; Brougham, D. F.; Wilhelm, C.; Gazeau, F. *ACS Nano* **2012**, *6*, 10935–10949.

(134) Serantes, D.; Baldomir, D.; Martinez-Boubeta, C.; Simeonidis, K.; Angelakeris, M.; Natividad, E.; Castro, M.; Mediano, A.; Chen, D. X.; Sanchez, A.; Balcells, L. I.; Martinez, B. *J. Appl. Phys.* **2010**, *108*, 073918/073911–073918/073915.

(135) Poselt, E.; Kloust, H.; Tromsdorf, U.; Janschel, M.; Hahn, C.; Masslo, C.; Weller, H. *ACS Nano* **2012**, *6*, 1619–1624.

(136) Mani, V.; Chikkaveeraiah, B. V. *Expert Opin. Med. Diagn.* **2011**, *5*, 381–391.

(137) Baselt, D.R.; Lee, G.U.; Natesan, M.; Metzger, S. W.; Sheehan, P. E.; Colton, R.J. *Biosens. Bioelectron.* **1998**, *13*, 731–739.

(138) Shieh, R.; Ackley, D.E. 2000; Vol. 167, p 6057.

(139) Li, Y.; Srinivasan, B.; Jing, Y.; Yao, X.; Hugger, M. A.; Wang, J. P.; Xing, C. *J. Am. Chem. Soc.* **2010**, *132*, 4388–4392.

(140) Srinivasan, B.; Li, Y.; Jing, Y.; Xu, Y.-H.; Yao, X.; Xing, C.; Wang, J.-P. *Angew. Chem., Int. Ed.* **2009**, *48*, 2764–2767.

(141) Srinivasan, B.; Li, Y.; Jing, Y.; Xing, C.; Slaton, J.; Wang, J.P. *Anal. Chem.* **2011**, *83*, 2996–3002.

(142) Hall, D.A.; Gaster, R.S.; Lin, T.; Osterfeld, S. J.; Han, S.; Murmann, B.; Wang, S.X. *Biosens. Bioelectron.* **2010**, *25*, 2051–2057.

(143) Osterfeld, S. J.; Yu, H.; Gaster, R. S.; Caramuta, S.; Xu, L.; Han, S. J.; Hall, D. A.; Wilson, R. J.; Sun, S.; White, R. L.; Davis, R. W.; Pourmand, N.; Wang, S. X. *Proc. Natl. Acad. Sci.* **2008**, *105*, 20637–20640.

(144) Hall, D. A.; Wang, S. X.; Murmann, B.; Gaster, R. S. *Conf. Proc. (Midwest Symp Circuits Syst.)* **2010**, 1779–1782.

(145) Eadie, M. J.; Tyrer, J. H.; Kukums, J. R.; Hooper, W. D. *Histochemie* **1970**, *21*, 170–180.

(146) Altman, F. P. *Histochemie* **1974**, *38*, 155–171.

(147) Cacao, E. E.; Nasrullah, A.; Sherlock, T.; Kemper, S.; Kourentzi, K.; Ruchhoeft, P.; Stein, G. E.; Willson, R. C. *PLoS One* **2013**, *8*, e56835.

(148) Cacao, E.E. PhD Dissertation, University of Houston, Houston, TX, 2012.

(149) Wu, J.; Chumbimuni-Torres, K. Y.; Galik, M.; Thammakhet, C.; Haake, D. A.; Wang, J. *Anal. Chem.* **2009**, *81*, 10007–10012.

(150) Fanjul-Bolado, P.; Hernandez-Santos, D.; Gonzalez-Garcia, M. B.; Costa-Garcia, A. *Anal. Chem.* **2007**, *79*, 5272–5277.

Chapter 2

Cubic Silica-coated and Amine-functionalized FeCo Nanoparticles with High Saturation Magnetization

2.1 Motivation

The synthesis of spherical magnetic nanoparticles has been widely studied and continues to garner attention due to their use in biosensing and biomedical applications.[1–3] For certain applications, however, geometries other than spherical are preferred (e.g., for applications involving magnetic-based biosensing devices, where the larger contact area of cubic nanoparticles can lead to more robust binding to a sensing platform).[4] In addition, the increase in interfacial contacts and decrease in void fraction should lead to enhanced sensitivity and improved signal-to-noise ratios for cubic vs. spherical magnetic nanoparticles.[5] Furthermore, although it is known that the properties of magnetic nanoparticles are strongly influenced by their size and shape,[6] magnetization data for some of the more common nanoparticle shapes are sorely lacking, particular for particles that have been coated with a thin layer of silica, which not only protects the magnetic cores from degradation,[7-8] but also permits their facile surface functionalization.[9]

In the work reported here, we systematically varied the reaction parameters in a liquid-phase reduction reaction to generate three distinct sizes of magnetic nanocubes, which we then coated with a relatively thin layer of silica. Previous reports of cubic FeCo described the synthesis of 68 nm FeCo nanocubes and nanocages with edge lengths of 500 nm.[10] Our modified recipe yielded FeCo nanocubes with body diagonals of 175 nm

(edge length = ~100 nm), 350 nm (edge length = 200 nm), and 450 nm (edge length = 260 nm), respectively (*vide infra*). Further, we thoroughly characterized the magnetic properties (saturation magnetization and coercivity) of all of these unique cubic particles, and then demonstrated their (amine-) functionalization and binding to a model sensor platform (carboxylic-acid-terminated self-assembled monolayer (SAM) on gold).

Due to their high saturation magnetization and cubic shape, FeCo nanocubes are promising materials for use in magnetic biosensing applications.[11,12] However, for many sensing applications that rely on molecular recognition (e.g., ligand or antibody binding) the FeCo nanoparticles must be coated with a robust, biocompatible, and readily modifiable coating. For many nanoparticles, silica is often the coating of choice because it meets these requirements.[13] We note that several studies have focused on embedding FeCo particles within a silica matrix,[14-16] and Pradhan, A.K. *et al.* have reported the coating of FeCo spheres using the Stöber process.[17,18] To our knowledge, however, the coating of cubic FeCo nanoparticles with silica *while retaining the cubic morphology after the coating process* has remained an elusive goal until now.

2.2 Materials and Methods

2.2.1 FeCo Synthesis

We prepared FeCo nanocubes using a modification of a known liquid-phase reduction reaction.[10] The chemicals used in the synthesis were of analytical grade and were used without purification. Millipore water (resistivity higher than 18 MΩcm) was used in the synthesis and washing steps. The wet chemical precipitation/synthesis involved reduction of aqueous Fe^{+2} and Co^{+2} with hydrazine and was performed in the presence of poly(ethylene glycol) and cyclohexane. Ferrous sulfate (0.7 g $FeSO_4 \cdot 7H_2O$),

cobalt chloride (0.175 g $CoCl_2 \cdot 4H_2O$), poly(ethylene glycol) (8 mL PEG-440 g/mol), and cyclohexane (0.8 mL) were dissolved in 50 mL water. This mixture was sonicated for 1.5 h at rt and then heated to 78 °C using an oil bath. A solution of hydrazine (20 mL NH_2NH_2) and sodium hydroxide (2.5 g NaOH) was added to the heated mixture. After 30 min, a black precipitate was obtained, which was washed three times with water and then once with toluene and acetone before drying under vacuum at rt. The molar ratio of Fe^{+2}/Co^{+2} was held constant in all of the nanoparticle syntheses, but the reaction time was varied to obtain cubes of varying sizes; specifically, reaction times of 30, 40, and 45 min afforded FeCo nanocubes with body diagonals of 175 nm (edge length = ~100 nm), 350 nm (edge length = 200 nm), and 450 nm (edge length = 260 nm), respectively. The length dimension for nanocubes described refers to the body diagonal. The length of the body diagonal was calculated using the following geometric relationship: body diagonal, nm = √3(cube side, nm).

2.2.2 Silica Coating

The FeCo nanocubes were stabilized with poly(vinyl pyrrolidone) (PVP, MW 10,000 g/mol) prior to coating them with silica. An aliquot of black FeCo powder (0.045 g) was suspended in 0.2 to 0.4 mL of 1% PVP solution in 20 mL ethanol, sonicated for 3 hours at 69 °C, and then mechanically agitated at the same temperature overnight. The PVP-stabilized FeCo nanocubes were washed multiple times with water and ethanol, centrifuged, and dried in a vacuum oven overnight. We used a modified version of the Stöber process[9] to coat the PVP-functionalized FeCo nanocubes with silica. Approximately 10–25 mg of PVP-stabilized FeCo nanocubes were dispersed in 20 mL ethanol and 2.2 mL water, and the mixture was sonicated for 30 min. To this mixture, 1.3

mL of 30% ammonium hydroxide (NH_4OH) and 0.1 mL (TEOS) was added to initiate the reaction under mechanical agitation, which was continued for 4–5 h. The sample was separated using a bar magnet and washed multiple times with ethanol and water.

2.2.3 Amine Functionalization

We used (3-aminopropyl)trimethoxysilane (APTMS) to decorate the surface of the silica-coated nanocubes with amino groups. To a 20-mL suspension of silica-coated nanoparticles in ethanol, we added 0.2 mL APTMS and 0.1 mL water with mechanical agitation overnight.

2.2.4 Characterization

These nanocubes were characterized by transmission electron microscopy (TEM; JEOL-2000 FX operating at 200 kV with attached energy dispersive X-ray spectroscopy; EDX), scanning electron microscopy (SEM; LEO-1525 operating at 15 kV), X-ray photon spectroscopy (XPS; PHI 5700 XPS with an Al Kα X-ray source), vibrating sample magnetometry (VSM; LakeShore VSM 7300 Series with LakeShore 735 Controller and LakeShore 450 Gaussmeter Software Version 3.8.0), and X-ray diffraction (XRD; Siemens D5000 X-ray diffractometer). For the TEM analyses, the nanoparticles were deposited on a 300 mesh holey carbon-coated copper grid and allowed to dry, and for the SEM analyses, the nanoparticles were deposited on a silicon wafer and allowed to dry. The images were processed and the size histograms were generated via analysis of ~50 particles. The magnetic properties (saturation magnetization, residual magnetization, and coercivity) of a known mass of sample were measured using VSM. For additional compositional and structural confirmation, we used EDX and XRD to characterize the nanocubes. For the latter studies, a concentrated sample of FeCo in ethanol was

deposited on a piranha-cleaned glass slide, and XRD was carried out using Cu Kα radiation (λ = 1.540562 Å) in the 2θ range from 0 to 90°. We also used XPS both to confirm the presence of the silica coating on the FeCo nanocubes and to demonstrate the subsequent amino-functionalization with APTMS; for these studies, the nanocubes were dispersed in ethanol, deposited on a gold wafer, and allowed to dry.

2.3 Results and Discussion

Figure 2.1 shows TEM and SEM images of the PVP-stabilized FeCo nanocubes along with their microscopy-derived size distributions, which illustrate both their cubic morphology and their monodisperse nature (save for the sample containing the largest nanoparticles, which appear less uniform with regard to size and shape). We note that Kodama *et al.* reported that varying the relative concentrations of the iron and cobalt precursors can control the shape of FeCo nanoparticles; specifically, Fe-rich solutions afford FeCo nanoparticles with cubic shapes, and Co-rich solutions afford FeCo nanoparticles with spherical shapes.[19] As a complement to these published results, the images in Figure 1 demonstrate our ability to tune the dimensions of the nanocubes from ~175 nm to ~450 nm simply by adjusting the reaction time. Prior research[10] that afforded 68 to 110 nm nanocubes and nanocages were obtained at reactions times of 30 and 90 min where the morphology changed from polyhedron to cubic as the time was increased from 2 min to 30–90 min. Cubic morphology offers the advantage of increased interfacial contact and enhanced sensitivity as compared to spherical nanoparticles, we hence focused on the synthesis of cubic FeCo nanoparticles and varied the reaction times beyond 30 min.

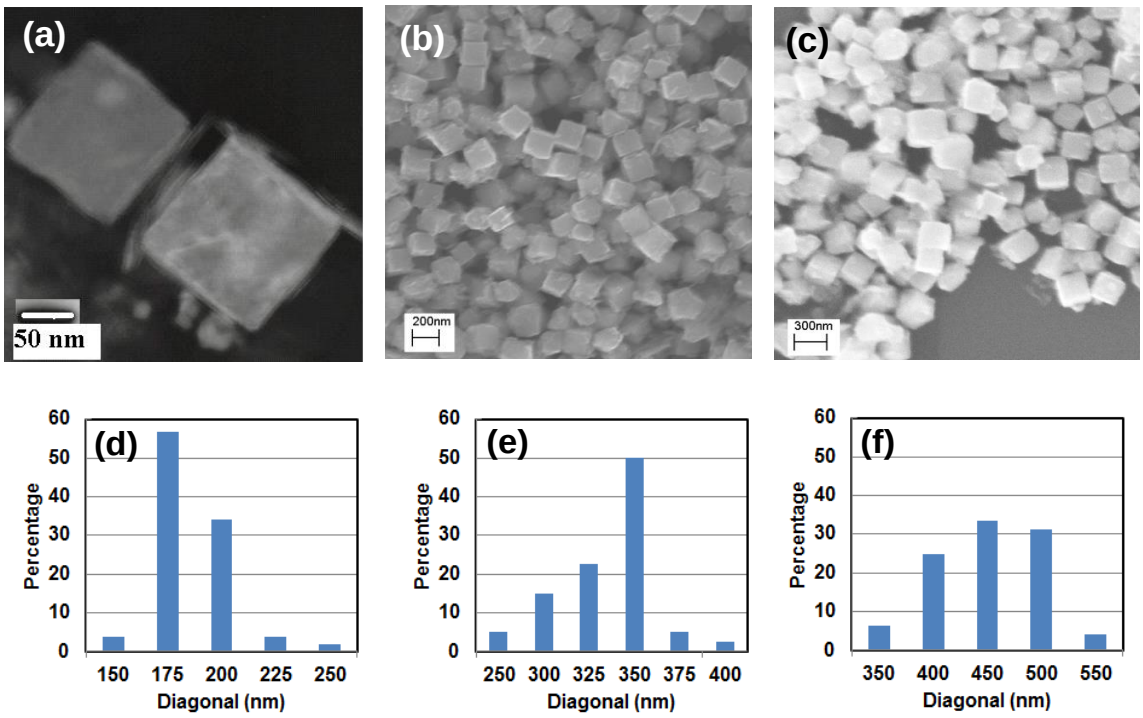

Figure 2.1 PVP-stabilized FeCo nanocubes: TEM image of (a) ~175 nm particles and SEM images of (b) ~350 nm, and (c) ~450 nm particles together with their microscopy-derived size distributions (d, e, f) based on 50 to 60 nanoparticles observed in an image. The sizes in nm correspond to the mean cubic body diagonal.

The nucleation rate is expected to be fast since hydrazine is a strong reducing agent for iron salts and cobalt salts; this was observed experimentally by the change is color from pink (Co(II) complex with hydrazine) to sea-green to black (nuclei) in less than 10 seconds. Other process parameters that affect the size distribution include temperature and agitation. It should be possible to sharpen the distribution in the case of ~450 nm FeCo nanoparticles. However, our main focus here was the silica coating and amine-functionalization; the reasonably narrow distributions obtained are satisfactory for these purposes. Figure 2.2 shows SEM and TEM images of the resultant silica-coated FeCo nanocubes, where the thickness of the silica coating is roughly 55 nm. Importantly, the SEM images confirm that the nanoparticles retain their cubic morphology after the

coating process. Due to the high residual magnetization (discussed later), the nanocubes have a high tendency to aggregate and it is very challenging to avoid aggregation and silica-coat them retaining the cubic shape.

The silica-coated FeCo nanocubes were further characterized by XRD and EDX (Figure 2.3). The XRD pattern in Figure 2.3a of the 450 nm FeCo nanocubes matched the simple cubic structure of FeCo alloy, with peaks assigned to its (011), (002), and (112) reflections (JCPDS No. 49-1568).[12] Further, the EDX data in Figure 2.3b show that composition of the FeCo nanocubes was $Fe_{72}Co_{28}$. Notably, the presence of Si and O peaks confirm that the nanocubes were coated with silica and the composition of silica was found to be $SiO_{1.4}$.

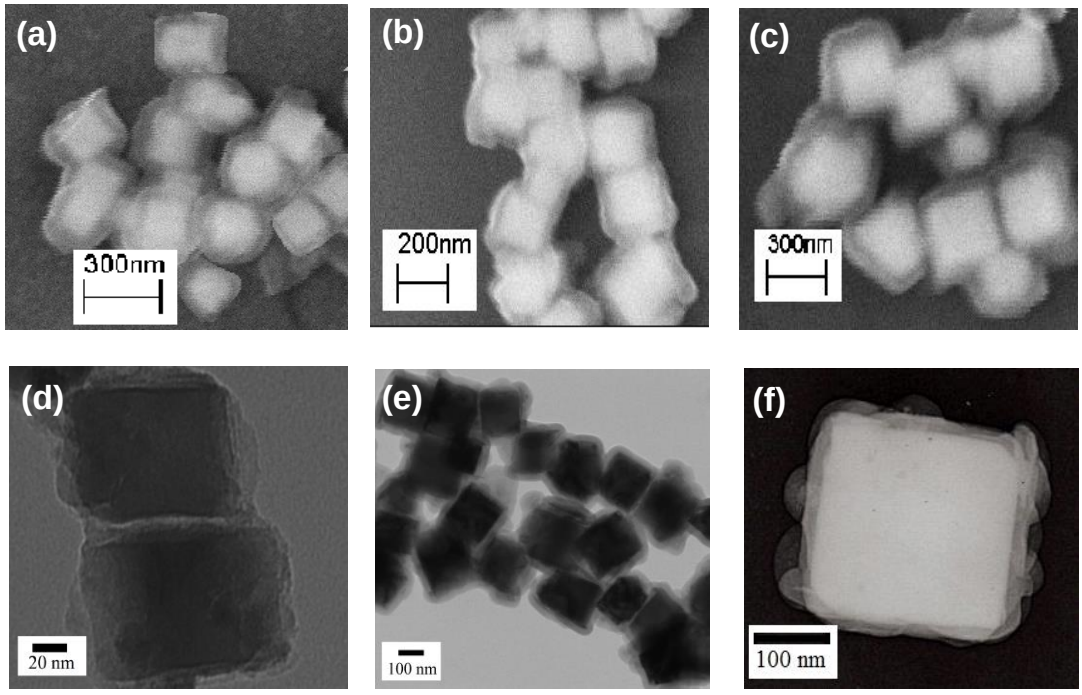

Figure 2.2 Top row: SEM images of silica-coated FeCo nanocubes (a) ~175 nm FeCo with 65 nm silica thickness, (b) ~350 nm FeCo with 45 nm silica thickness, and (c) ~450

nm FeCo with 45 nm silica thickness. Bottom row: the corresponding TEM images (d, e, f), respectively.

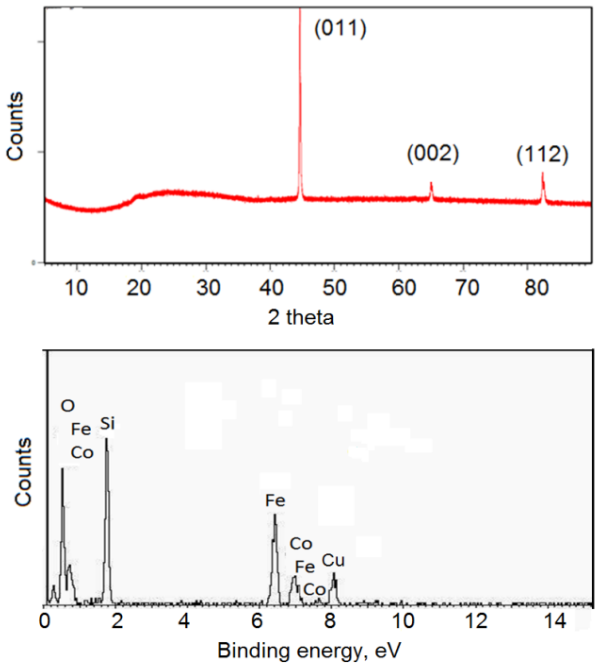

Figure 2.3 Silica-coated FeCo nanocubes (~450 nm FeCo core) analyzed by (a) XRD and (b) EDX.

The nanoparticles were functionalized with amine following which the amine-functionalized nanoparticles were electrostatically bound to the carboxylic acid functionalized sensor. The zeta potential of amine-functionalized nanoparticles in ethanol is highly negative and results in high colloidal stability of the nanoparticles.[20] However, due to the high saturation magnetization and coercivity, it is not possible to keep the nanoparticles completely separated during imaging. The amine-functionalization was demonstrated directly by XPS (Figure 2.4), where there is a clear peak at 400 eV indicating the presence of nitrogen. In the same figure, this is also confirmed by its comparison to no/low peak in the absence of amine-functionalization. The ratio of

atomic percentages of O (binding energy 533 eV) and Si (binding energy at 103 eV) was 2.3 ± 0.1 to 1, which is consistent with the expected stoichiometry.

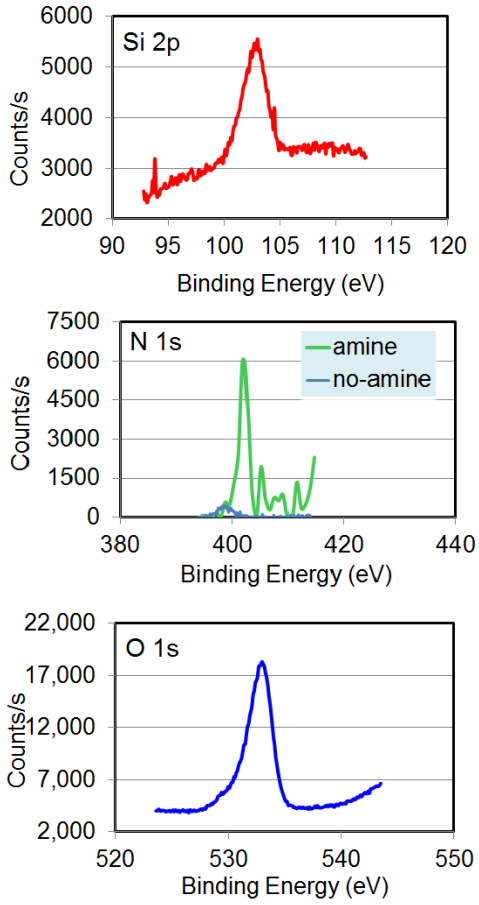

Figure 2.4 XPS analysis of amino-functionalized silica-coated FeCo nanocubes.

We used SEM to provide additional (albeit indirect) support for the amino functionalization by observing the binding of the amino-functionalized nanocubes to a carboxylic-acid-terminated self-assembled monolayer (SAM) on gold generated from 16-mercaptohexadecanoic acid (Figure 2.5).[21] Figure 2.5 demonstrates the binding of the amine-functionalized FeCo nanocubes to the surface of a carboxylic-functionalized sensor. The sensor was washed multiple times with ethanol and water to remove any non-specifically bound nanoparticles. For the latter study, the wafer was placed in a

suspension of amine-functionalized FeCo nanocubes in ethanol for 1 h at rt and then washed alternately with ethanol and water to remove any weakly bound nanoparticles from the SAM surface. The strongly bound nanoparticle arrays shown in Figure 2.5 provide a rudimentary demonstration of the type of sensing platform that is one of the ultimate goals of our studies.[22–24] The binding of the amine-functionalized nanoparticles to the carboxylic-functionalized wafer serves as a demonstration of the binding between nanoparticles and sensor in a sensor application.

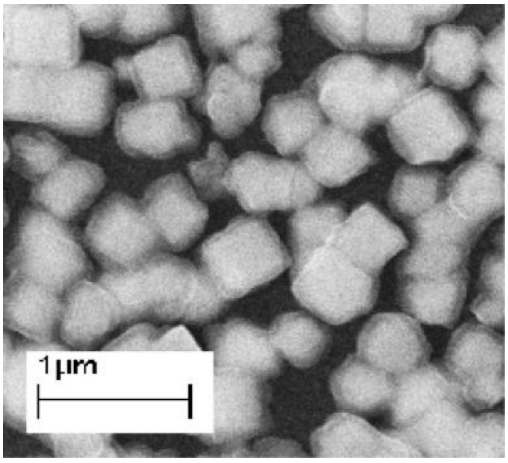

Figure 2.5 SEM image of 450 nm amino-functionalized FeCo nanocubes electrostatically bound to a carboxylic acid-terminated gold wafer.

Our magnetoresistance-based sensor consists of layers of Co/Cu/Co that are coated with alumina or silica and then functionalized with a molecular recognition element. Magnetic nanoparticles decorated with a target biomarker can bind to the sensor by direct or sandwich assays, and these magnetic nanoparticles are detected by a corresponding change in magnetoresistance.[25]

The magnetic properties of the PVP-stabilized and silica-coated FeCo nanocubes were characterized by VSM. Figure 2.6 shows the obtained magnetization curves, which indicate a saturation magnetization of 166 emu/g and coercivity (H) of 215 Oe for the

~450 nm PVP-stabilized FeCo nanocubes. Unsurprisingly, for both sets of the ~450 nm silica-coated FeCo nanoparticles, the saturation magnetization on a per gram basis is noticeably lower (as expected due to the mass of the non-magnetic silica coating). Further, as indicated by the bar graphs in Figure 2.7, the average saturation magnetization for all sizes of the PVP-stabilized FeCo nanocubes (having composition $Fe_{72}Co_{28}$ as noted above) was 168 ± 4 emu/g, which is similar in magnitude to the saturation magnetization of bulk $Fe_{70}Co_{30}$ (240 emu/g)[26] and bulk $Fe_{65}Co_{35}$ (245 emu/g).[27]

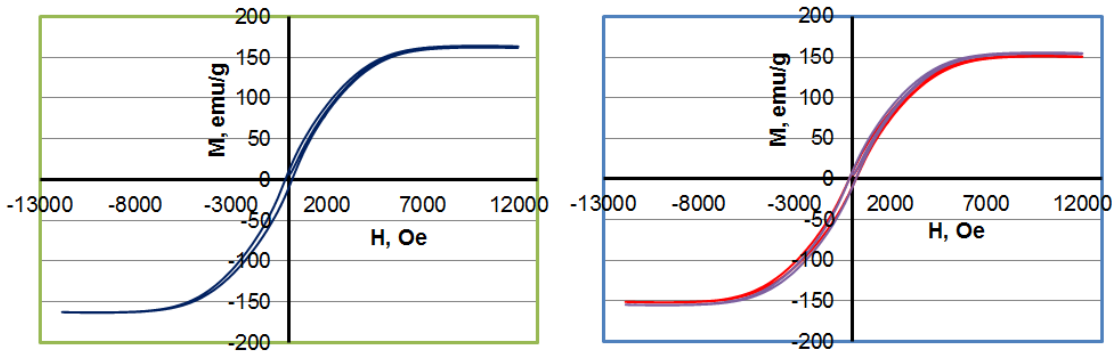

Figure 2.6 Magnetization curves for 450 nm FeCo nanocubes (a) PVP-stabilized particles and (b) silica-coated nanoparticles from two independent syntheses.

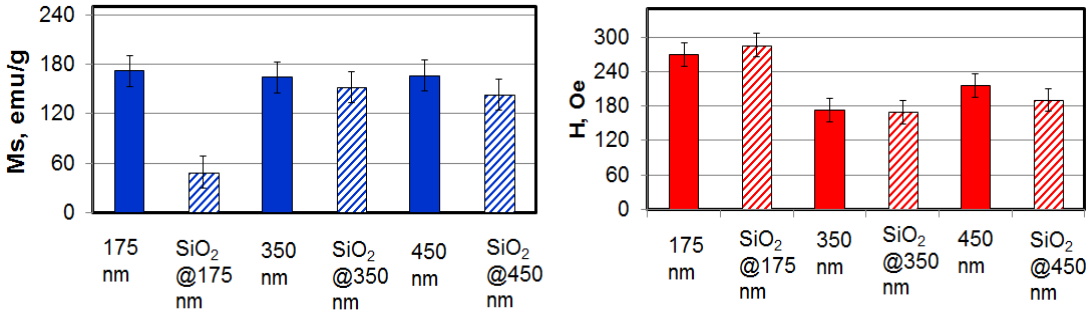

Figure 2.7 Magnetization curves for 450 nm FeCo nanocubes (a) PVP-stabilized particles and (b) silica-coated nanoparticles from two independent syntheses.

We note that Lu, H. M. *et al.*[27] studied the size-dependent saturation magnetization of γ-Fe_2O_3, $CoFe_2O_4$, and $MnFe_2O_4$ nanoparticles, and found that beyond a certain size unique for each material, the ratio of saturation magnetization of the sample

to that of the bulk value (Ms/Ms_{bulk}) is constant. In case the of our FeCo nanocubes, the Ms/Ms_{bulk} ratio was also found to be constant for the three sizes examined.

In contrast to the PVP-stabilized FeCo nanocubes, the saturation magnetization of the ~175 nm silica-coated FeCo nanocubes was 48 ± 1 emu/g for 175 nm, and that for both the ~350 and ~450 nm silica-coated FeCo nanocubes was 146 ± 13 emu/g. The decrease in magnetization on a per gram basis is due to the increase in the mass of the non-magnetic component (silica). Since the mass, for example, of each 175 nm nanocube increased from ~8 fg to ~33 fg upon coating with silica, the observed ~fourfold decrease in the Ms (172 emu/g vs. 48 emu/g) is attributed to the ~fourfold increase in the mass of nanoparticles. An analogous but less pronounced correlation can be drawn with the magnetization data for the ~350 and ~450 nm FeCo nanocubes.

Based on the magnetization curves obtained and the hysteresis trends observed in Figure 6, the FeCo nanocubes prepared here are not superparamagnetic. Nevertheless, they can be readily manipulated by an external magnetic field. Further, the observed strong saturation magnetization coupled with their facile functionalization and subsequent binding to a model sensor platform offers evidence that these silica-coated FeCo nanocubes warrant further investigation in magnetic biosensing applications.

2.4 Conclusions

By systematically varying the reaction parameters in a liquid-phase reduction reaction, large FeCo nanocubes with tunable body diagonal lengths of 175, 350, and 450 nm were synthesized. The nanocubes were initially stabilized with poly(vinyl pyrrolidone) (PVP) and then coated with a relatively thin layer of silica (55 nm thick),

which allowed them to retain their cubic shape. The magnetization curves showed that the PVP-stabilized nanocubes exhibited a high saturation magnetization of 167 ± 4 emu/g. The saturation magnetization decreased upon coating with silica to 146 ± 13 emu/g for the particles with 350 and 450 nm FeCo cores and 48 ± 1 emu/g for the particles with 175 nm FeCo cores. The silica-coated FeCo nanocubes were then functionalized with 3-(aminopropyl)-trimethoxysilane (APTMS), and a layer of surface-bound nanoparticle was generated by exposing the resultant amine-functionalized nanocubes to self-assembled monolayers (SAMs) on gold terminated with carboxylic-acid groups.

2.5 References

(1) Tran, N.; Webster, T. *J. Mater. Chem*. **2010**, *20*, 8760–8767.

(2) McBain, S.C.; Humphrey, H.P.Y.; Dobson, J. *Int. J. Nanomed*. **2008**, *3*, 169–180.

(3) Roca, A.G.; Costo, R.; Rebolledo, A.F.; Veintemillas-Verdaguer, S.; Tartaj, P.; Gonzalez-Carreno, T., Morales, M.P.; Serna, C. J. *J. Phys. D: Appl.* **2009**, *42*, 1–12.

(4) Sau, T.; Rogach, A. L. *Adv. Mater.* **2010**, *22*, 1781–1804.

(5) Dovgolevsky, E.; Haick, H. *Small* **2008**, *2*, 2059–2066.

(6) Treguer-Delapierre, M.; Majimel, J.; Mornet, S.; Duguet, E.; Ravaine, S. *Gold Bull*. **2008**, *41*, 195–207.

(7) Fei, Y.; Laurent, S.; Fornara, A.; Astolfi, L.; Qin, J.; Roch, A.; Martini, A.; Toprak, M.; Muller, R.; Muhammed, M. *Contrast Media Mol. Imaging* **2012**, 7, 460–468.

(8) Selvan, S.T. *Biointerphases* **2010**, *5*, FA10–15.

(9) Weichold, O.; Tigges, B.; Bertmer, M.; Moller, M. *J. Colloid Interf. Sci.* **2008**, *324*, 105–109.

(10) Wei, X.; Zhu, G.; Liu, Y.; Ni, Y.; Song, Y.; Xu, Z. *Chem. Mater*. **2008**, *20*, 6248–6253.

(11) Baselt, D.R.; Lee, G.U.; Natesan, M.; Metzger, S.T.; Sheehan, P.E.; Colton, R.J. *Biosensors & Bioelectronics* **1998**, *13*, 731–739.

(12) Koh, I.; Josephson, L. *Sensors* **2009**, 8130–8145.

(13) Guerrero-Martinez, A.; Perez-Juste, J.; Liz-Marzan, L. M. *Adv. Mater.* **2010**, *22*, 1182–1195.

(14) Thirumal, E.; Prabhu, D.; Chattopadhyay, K.; Ravichandran, V. *Phys. Status Solidi A* **2010**, *207*, 2505–2510.

(15) Carta, D.; Casula, M.F.; Bullita, S.; Falqui, A.; Corrias, A. *J. Nanopart. Res.* **2011**, *13*, 3489–3501.

(16) Falqui, A; Corrias, A.; Gass, M.; Mountjoy, G. *Microsc. Microanal.* **2009**, *15*, 114–124.

(17) Gao, J.; Gu, H.; Xu, B. *Acc. Chem. Res.* **2009**, *42*, 1097–1107.

(18) Harris, M.T.; Brunson, R.R.; Bryers, C.H. *J. Non-Cryst. Solids* **1990**, *121*, 397–403.

(19) Kodama, D.; Shinoda, K.; Sato, K.; Konno, Y.; Joseyphus, R.J.; Motomiya, K.; Takahashi, H.; Matsumoto, T.; Sato, Y.; Tohji, K.; Jeyadevan, B. *Adv. Mater*. **2006**, *18*, 3154–3159.

(20) Graf, C.; Qi Gao, Q.; Schutz, I.; Noufele, C.; Ruan, W.; Posselt, U.; Korotianskiy, E.; Nordmeyer, D.; Fiorenza, R.; Hadam, S.; Vogt, A.; Lademann, J.; Haucke, V.; Ruhl, E. *Langmuir* **2012**, *28*, 7598–7613.

(21) Chingwangso, P.; Jamison, A.C.; Lee, T.R. *Acc. Chem. Res.* **2011**, *44*, 511–519.

(22) Gaster, R.S.; Xu, Liang; Han, Shu-Jen; Wilson, R.J.; Hall, D. A.; Osterfeld, S. J.; Yu, H.; Wang, S.X. *Nat. Nanotechnol.* **2011**, *6*, 314–320.

(23) Dittmer, W.U.; Kievet, P.; Prins, M.W.J.; Vissers, J.L.M.; Mersch, M.E.C.; Martens, M. *J. Immunol. Methods* **2008**, *338*, 40–46.

(24) Osterberg, F.W.; Dalslet, B.T.; Damsgaard, C.D.; Freitas, S.C.; Freitas, P. P.; Hansen, M. F. *IEEE Sens. J.* **2009**, *9*, 682–688.

(25) Litvinov, D.; Willson, R. Patent application number 20100188075, **2010**.

(26) Wei, X.; Zhu, G.; Liu, Y.; Ni, Y.; Song, Y.; Xu, Z. *Chem. Mater.* **2008**, *20*, 6248–6253.

(27) Lu, H.M.; Zheng, W.T.; Jiang, Q. J. Phys. D: *Appl. Phys*. **2007**, *40*, 320–325.

Chapter 3

Morphology and Crystallinity as Tools for Tailoring Magnetic Properties: Comparison of Fe_3O_4 Nanocubes and Nanospheres

3.1 Motivation

Magnetic nanoparticles (MNPs) have tremendous potential for broad use in biomedical applications.[1-6] This range of possible applications is due in part to recent improvements in the understanding of how nanoparticle structure and magnetic properties are related.[7] The tuning of MNP properties can be challenging considering the interdependence of various factors in determining magnetic properties. Chapter 1 summarizes the key parameters (size, shape, composition, and shell-core design) that can be modulated to tailor the MNP properties for a particular application.

Extensive data exists on the effects of size,[8-10] composition,[11-13] and shell-core design;[14-16] however, defining the effect of shape on the magnetic properties continues to challenge the research community. There have been efforts at synthesizing MNPs exhibiting a variety of shapes: ferrite nanocubes,[17-19] maghemite nanorods,[20] NiFe nanowires,[21] cobalt nanodiscs,[22,23] magnetite tetrapods,[2] and Au-MnO nanoflowers.[24] There are also articles that describe the influence of particle shape on magnetic properties.[10,18,25-31] However, only a handful of studies[28-31] have focused on comparing the magnetic properties as a *function of shape* using a common basis (same volume, same diameter/body diagonal, or same surface area). These are summarized in Table 1.5. Further, the shape of an MNP has been shown to play an important role during particle

adhesion, distribution, and internalization in biosensing or drug delivery.[32] But can the correlation between magnetization and shape be attributed simply to geometry? How this question is being addressed can be seen in the research projects that have been recently pursued.

The effect of geometry on MNP magnetic properties continues to be evaluated for biosensing applications.[33,34] For such applications, the larger contact area of cubic nanoparticles can lead to a more robust binding to a sensing platform or cell surface.[35] In comparing spherical and disk-shaped nanoparticles, Ferrari *et al*. have reported a higher adhesion probability for an ellipsoidal nanoparticle due to the larger surface area available for contact as compared to a spherical nanoparticle of same volume.[33] Correspondingly, cubic Fe_3O_4 nanoparticles have a higher surface available for contact with a planar interface as compared to spherical Fe_3O_4 nanoparticles, and therefore a higher adhesion to the sensor is expected. The increased adhesion should lead to an enhanced sensitivity and an improved signal-to-noise ratio for these cubic MNPs. I used this hypothesis to underline the anticipated increase in sensitivity of my cubic FeCo MNPs for biosensing platform applications in Chapter 2. However, prior reports on biosensor applications have involved investigations that focus on the binding of the magnetic material to a contact surface, not necessarily on the inherent strength of the magnetic fields of the MNPs involved.

As shown in Table 1.5, the few studies that have provided an evaluation of the influence of nanoparticle shape on intrinsic magnetic properties have focused on sizes less than 25 nm.[28-31] The results from these studies do not conclusively show which

shape has a greater influence on magnetic properties. When comparing a set of $CoFe_2O_4$ cubes and spheres, Song *et al.* found a large difference only in the coercivity and they attributed lower coercivity for cubic nanoparticles to less surface pinning that resulted due to a reduction in the number of missing coordinating oxygen atoms.[28] Both Salazar-Alvarez *et al.* and Zhen *et al.* compared cubic and spherical Fe_3O_4 nanoparticles and observed a higher blocking temperature (T_B) for the spherical Fe_3O_4 MNPs.[29,30] Noh *et al.* corroborated this observation of a higher T_B in the case of spherical $Zn_{0.4}Fe_{2.6}O_4$ MNPs as compared to cubic $Zn_{0.4}Fe_{2.6}O_4$ ones.[36] These observations, when considered in terms of the linear relationship between T_B and the anisotropy constant,[36] are supported by the knowledge that the anisotropy constant for spherical nanoparticles is higher than cubic nanoparticles of the same volume. Zhen *et al.* also observed higher saturation magnetization (Ms) for cubic MNPs as compared to spherical MNPs of the same volume.[30] A more recent paper by Noh *et al.* examined the higher Ms in cubic nanoparticles as compared to spherical nanoparticles of the same volume by simulating the orientations of the magnetic spin structures using an object-oriented micromagnetic framework program (OOMMF).[36] They found that the disordered spins were 4% in cubic MNPs and 8% in spherical MNPs. Based on these simulations, they hypothesized that the lower disordered spins in 18 nm edge $Zn_{0.4}Fe_{2.6}O_4$ nanocubes gave rise to a higher Ms as compared to 22 nm diameter nanospheres of equivalent volume. MNPs store and dissipate external energy as heat and Noh *et al.* also showed that the amount of dissipated heat is directly proportional to the area of the hysteresis loop (higher coercivity).[36] Thus, in addition to better particle adhesion that might result in improved sensitivity in biosensing applications,[37] the higher saturation magnetization, higher coercivity and

associated higher heat dissipation observed for nanocubes also make them better candidates for optimizing magnetic hyperthermia applications.

While comparing magnetic properties of cubic and spherical Fe_3O_4 MNPs, Zhen, *et al.*[30] observed that the higher-magnetization cubic nanoparticles had a larger crystallite size and a higher degree of crystallinity. Several researchers[38-41] have noted a linear relationship between magnetization and crystallinity, and demonstrated an improvement in magnetic properties with a higher degree of crystallinity for cobalt, copper, and lithium ferrite nanoparticles. There have been no prior reports on the effect of crystallinity on the magnetic properties of Fe_3O_4 MNPs. Hence, I used a high-resolution transmission electron microscope (HR-TEM) and an X-ray diffractometer to evaluate the crystallinity of a series of cubic and spherical MNPs. The size ranges for the superparamagnetic, single-domain, and multi-domain regimes is unique for each type of nanoparticle; Fe_3O_4 nanoparticles less than ~25 nm are in the superparamagnetic regime, those in the 25–80 nm range correspond to the single-domain regime, and those beyond 80 nm are associated with the multi-domain regime.[42,43] Most of the shape-comparison studies have been performed on MNPs that fall in the superparamagnetic regime,[44] or at least in the single-domain regime.[44] For the analysis presented in this paper, I expanded the size range used for the comparison of Fe_3O_4 cubic (body diagonals of 135, 150, 175, 225 nm) and spherical (diameters of 100, 125, 135, 150, 175, 225 nm) nanoparticles to focus on the effect of shape and crystallinity on the magnetic properties of nanoparticles that would definitely lie within the multi-domain size range.[44]

The decision to focus on magnetite for these experiments was based upon the relative ease of syntheses of these iron oxide nanoparticles and the notable absence of an in-depth comparison of the effect of shape and crystallinity on the magnetic properties of the widely-used Fe_3O_4 nanoparticles in the multi-domain range.

3.2 Materials and Methods

The reaction parameters were varied using a modified solvothermal reaction[19,45] process and a liquid phase reduction process[46] to generate distinct sizes of Fe_3O_4 nanocubes and nanospheres, respectively. The chemicals used in the syntheses described below were of analytical grade and were used without further purification. Millipore water (resistivity higher than 18 MΩ) was used in the synthesis and washing steps.

3.2.1 Cubic Fe_3O_4 MNP Synthesis

Using a variation of a known solvothermal method,[19,45] I synthesized Fe_3O_4 nanocubes with body diagonals of 135, 150, 175, and 225 nm (edge length 78, 85, 100, and 130 nm, respectively). Iron acetylacetonate [$Fe(acac)_3$] and oleic acid were heated to 290 °C in benzyl ether as a solvent and stirred in a round bottom flask using a magnetic stirrer. After 30 min, a black precipitate was obtained, which was washed multiple times with ethanol and dried under vacuum at room temperature. By varying the reactant concentration and reaction time, Fe_3O_4 nanocubes with tunable body diagonal lengths were achieved.

3.2.2 Spherical Fe_3O_4 MNP Synthesis

I modified the recipe of the procedure reported by Deng *et al* [46] to yield spherical Fe_3O_4 nanoparticles with diameters of 100, 125, 135, 150, 175, and 275 nm. This involved charging a round bottom flask with iron chloride (1.4 g, $FeCl_3.6H_2O$) and 15 mL of ethylene glycol, followed sequentially by the addition of sodium acetate (3.6 g), which rapidly turned the orange $FeCl_3 \cdot 6H_2O$ solution to a brown color. The solution was stirred for 30 min and then injected at once into a round-bottom flask containing a vigorously stirred solution of PVP (0.40 g) in 35 mL of ethylene glycol heated to 180 °C. This mixture was then vigorously stirred at 180 °C for 4–24 hours during which a black precipitate was obtained. The black precipitate was washed multiple times with ethanol, Millipore water, and dried under vacuum at room temperature. Agitation (stirrer speed), temperature, and reaction time were the process parameters that were varied to obtain Fe_3O_4 nanospheres of diameters that either matched the body diagonal of the synthesized nanocubes or had the same volume of the synthesized nanocubes.

3.2.3 Characterization

The nanocubes were characterized by transmission electron microscopy (TEM; JEOL-2000 FX operating at 200 kV with attached energy dispersive X-ray spectroscopy; EDS), scanning electron microscopy (SEM; LEO-1525 operating at 15 kV), and X-ray diffraction (XRD; Siemens D5000 X-ray diffractometer). For the TEM analyses, the nanoparticles were deposited on a 300 mesh holey carbon-coated-copper grid and allowed to dry. For the SEM analyses, the nanoparticles were deposited on a silicon wafer and allowed to dry. The size distribution for each sample was generated by

analysis of 50-60 nanoparticles. XRD was used for compositional and crystal structure determination. For XRD analysis, a concentrated sample in ethanol was deposited on a piranha-cleaned glass slide, with XRD being carried out using Cu Kα radiation (λ = 1.540562 Å) at the 2θ range from 0 to 90°. In addition to imaging, TEM was also used to obtain diffraction patterns that enabled analysis of the crystallinity and compositional purity of the sample. The magnetic properties (saturation magnetization, residual magnetization, and coercivity) of a known mass of the sample were measured using a vibrating sample magnetometer (VSM; LakeShore VSM 7300 Series with LakeShore 735 Controller and LakeShore 450 Gaussmeter. Software Version 3.8.0).

3.2.4 Preliminary Experiments Using a GMR Sensor

A basic GMR usually includes ferromagnetic layers interspersed with non-ferromagnetic layers and an antiferromagnetic exchange coupling generates the alternating opposing magnetizations required for the GMR effect.[47] As described in Chapter 2, the magnetoresistance-based sensor (1μm x 400 nm) used for this study consists of layers of Co/Cu/Co that are coated with alumina or silica and then functionalized with a molecular recognition element. On binding to the sensor, the MNPs are detected by a corresponding change in peak-to-peak distance (Delta x as shown in Figure 3.4) on the plot of resistance versus field. In my preliminary experiment, I deposited 0.25 mL of 1 mg/mL (that is same number of same-volume cubic and spherical MNPs) on each sensor and noted the change in peak-to-peak distance for each sample on each sensor.

3.3.5 Preliminary Experiments Using Force-Induced Remnant Magnetization (FIRMS)

The recently reported FIRMS technique, in which a change in magnetic signal is measured as a function of increasing mechanical force, was used to differentiate between the binding of the cubic and spherical MNPs to the sensor surface.[48-50] The MNPs were functionalized with silane, as described in Chapter 2, and then electrostatically bound to COOH-terminated biotin. The sensor surface was functionalized with streptavidin. The MNPs were allowed to bind to the surface and then subjected to increasing speeds of centrifugation (centrifugal force) to compare the speed/force that removed the same number of cubic and spherical MNPs from the surface.

3.3 Results and Discussion

Based on the synthetic method by Kim *et al.*[19] that afforded magnetite nanocubes in the body diagonal size range of 35 to 275 nm (~20 to 160 nm sides), I prepared oleic-acid stabilized Fe_3O_4 nanocubes with body diagonals in the range 135 to 225 nm by controlling the reaction time and agitation. Similarly, I varied the same process parameters (reaction time and agitation) in a method developed by Deng *et al.*[46] that yielded nanospheres of 200 to 800 nm diameter, and obtained Fe_3O_4 nanospheres in the size range 100 to 275 nm. Figures 3.1 and 3.2 show the scanning electron microscope (SEM) images for the resulting series of nanocubes and nanospheres, and the associated size distributions.

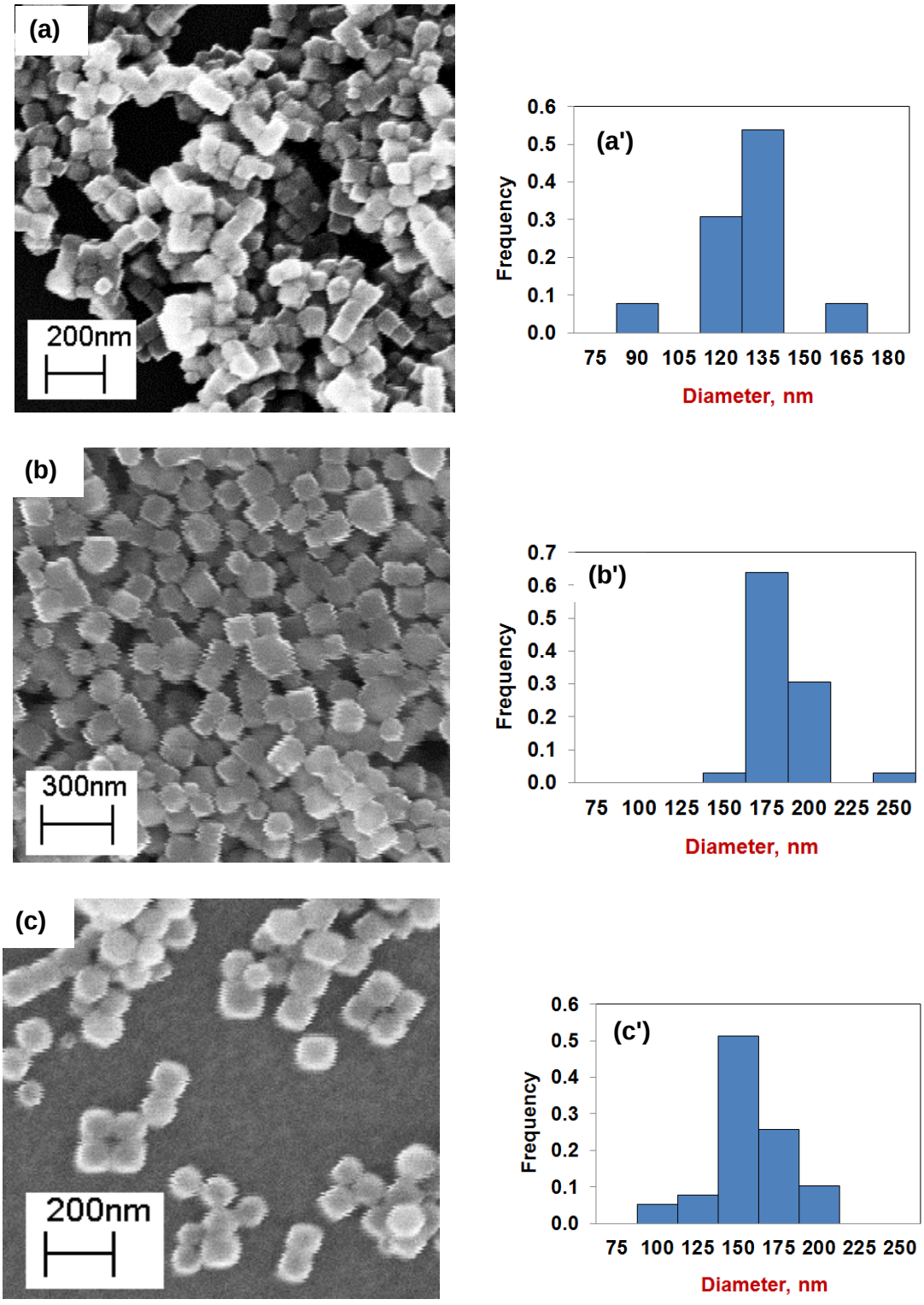

Figure 3.1 SEM images of cubic Fe_3O_4 nanoparticles of body diagonals (a) 135 nm, (b) 150 nm, (c) 175 nm, and (d) 225 nm. The corresponding size distributions for these nanoparticles are shown in bar graphs a'-d'. (Continued on next page.)

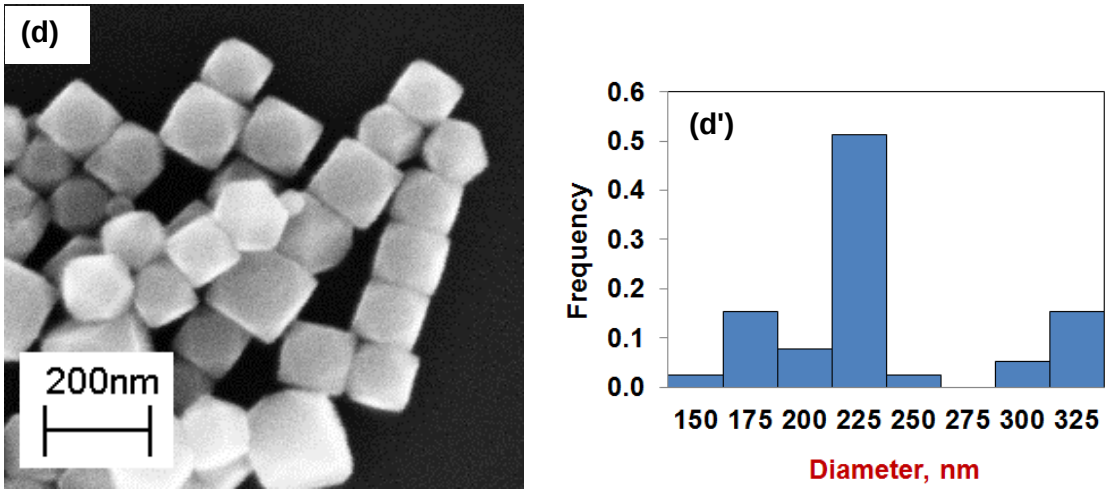

Figure 3.1 - Continued SEM images of cubic Fe_3O_4 nanoparticles of body diagonals (a) 135 nm, (b) 150 nm, (c) 175 nm, and (d) 225 nm. The corresponding size distributions for these nanoparticles are shown in bar graphs a'-d'.

For the same-body diagonal/diameter basis, nanocubes and nanospheres of 135, 150, and 175 nm were compared. The same-volume pairs included nanocubes of 150, 175, and 225 nm body diagonal and nanospheres of 100, 125, and 150 nm diameter, respectively. The magnetic properties of saturation magnetization (Ms) and coercivity (H) were obtained for each sample using VSM. Both shapes exhibited ferrimagnetic behavior as described in Figures 1.2 and 1.3 in Chapter 1.

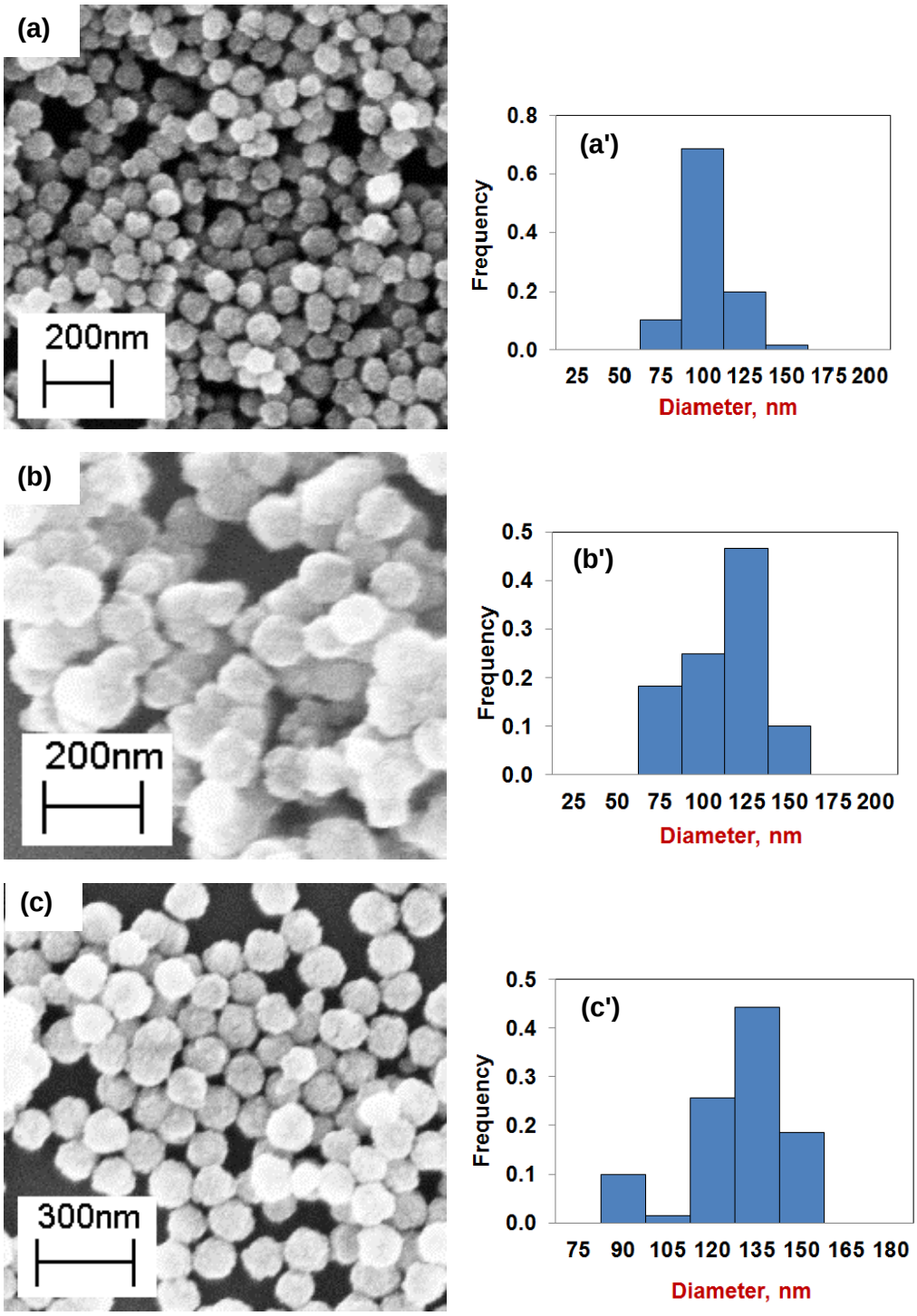

Figure 3.2 SEM images of spherical Fe_3O_4 nanoparticles of diameters (a) 100 nm, (b) 125 nm, (c) 135 nm, (d) 150 nm, (e) 175 nm, and (f) 275 nm. The corresponding size distributions for these nanoparticles are shown in bar graphs a'-f'. (Continued on the next page.)

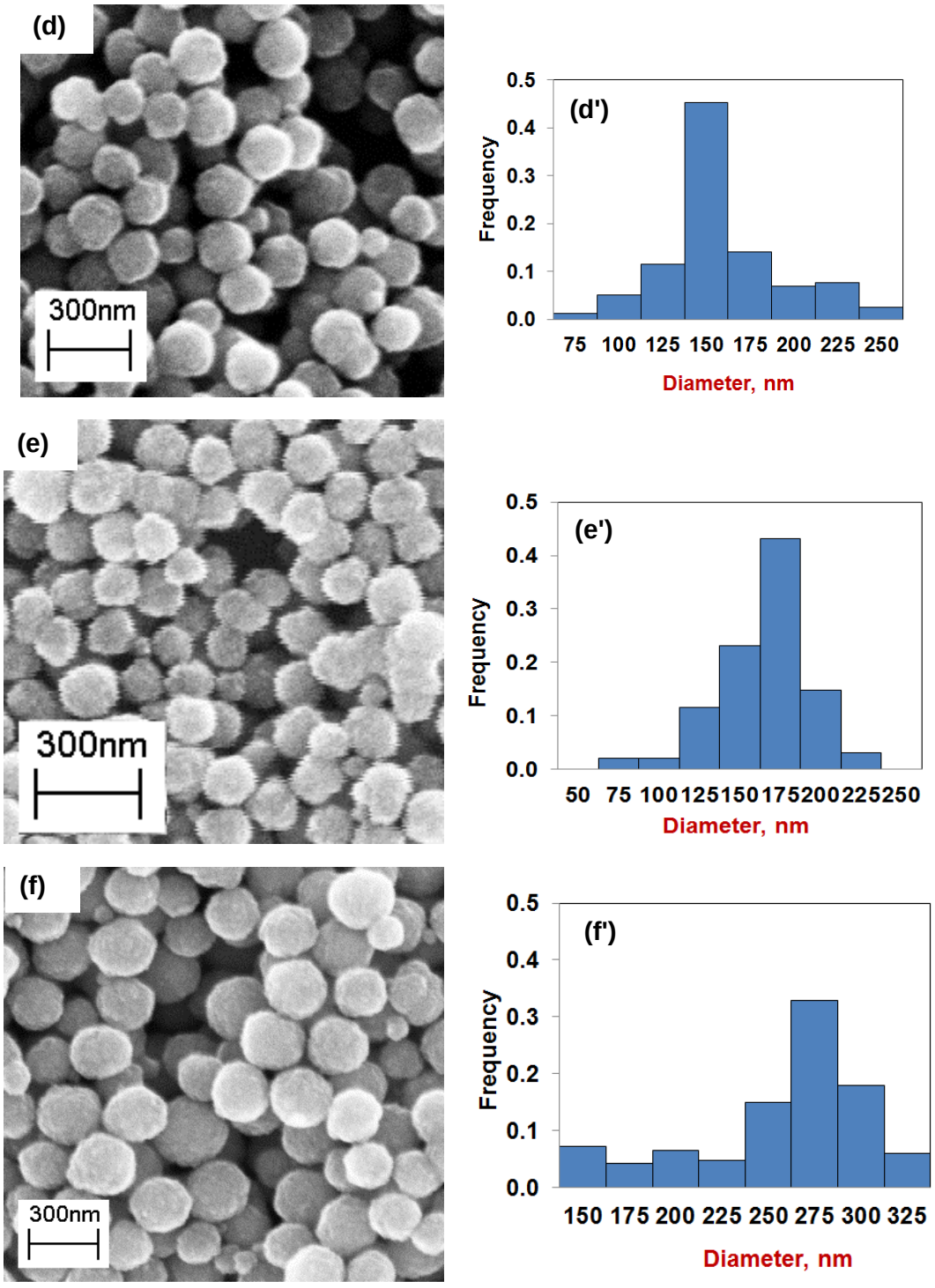

Figure 3.2 - Continued SEM images of spherical Fe_3O_4 nanoparticles of diameters (a) 100 nm, (b) 125 nm, (c) 135 nm, (d) 150 nm, (e) 175 nm, and (f) 275 nm. The corresponding size distributions for these nanoparticles are shown in bar graphs a'-f'.

The saturation magnetization and coercivity data for the synthesized nanocubes and nanospheres is summarized in Figure 3.3 and the comparison of properties on a same-volume and same-body diagonal/diameter basis is shown in Tables 3.1 and 3.2. In the 100-275 nm size range, the average Ms of the nanospheres was 60 ± 15 emu/g and in the 125-225 nm size range, the average Ms of the nanocubes was 90 ± 7 emu/g. Overall, the magnetic data consistently showed that the cubic Fe_3O_4 MNPs were better than spherical Fe_3O_4 MNPs in terms of saturation magnetization, a parameter important for sensing applications. The coercivity – a parameter important in hyperthermia applications – also produced higher values for the nanocubes during these comparisons.

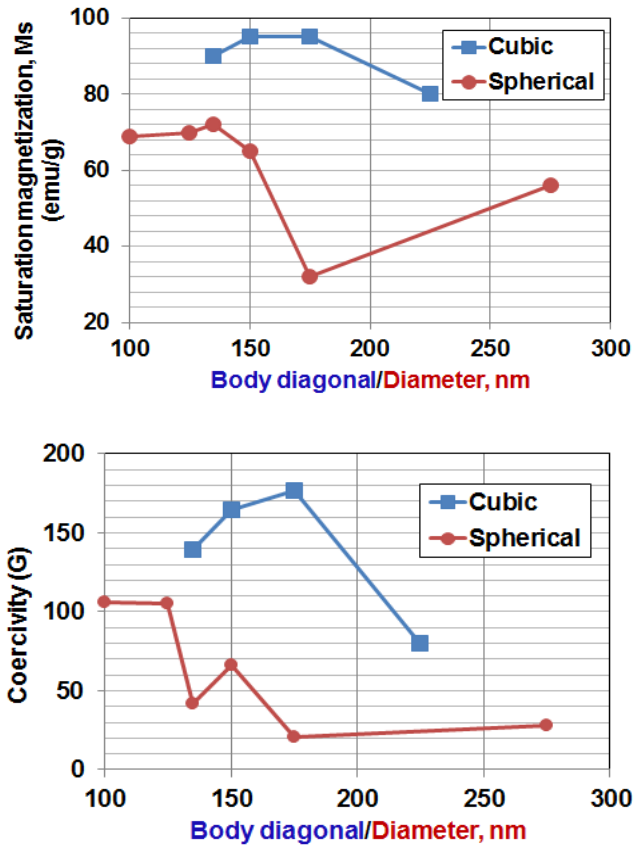

Figure 3.3 Graphs of the magnetic properties of cubic and spherical Fe_3O_4 MNPs as a function of MNP size for (a) saturation magnetization and (b) coercivity.

Table 3.1 Comparison of Magnetic Properties for Fe_3O_4 Nanocubes and Nanospheres of Same-Body Diagonal/Diameter

MNP Shape	**Size (nm)**	**Ms ratio[1] (emu/g)**	**H ratio[2] (G)**
Cube Sphere	135 135	1.3	3.3
Cube Sphere	150 150	1.5	2.1
Cube Sphere	175 175	3.0	8.4

[1]Ms ratio = $(Ms)_{nanocubes}/(Ms)_{nanospheres}$
[2]H ratio = $(H)_{nanocubes}/(H)_{nanospheres}$

Table 3.2 Comparison of Magnetic Properties for Fe_3O_4 Nanocubes and Nanospheres of Same-Volume

MNP Shape	**Size (nm)**	**Ms ratio[1] (emu/g)**	**H ratio[2] (G)**
Cube Sphere	150 100	1.4	1.6
Cube Sphere	175 125	1.4	1.7
Cube Sphere	225 150	1.2	1.2

[1]Ms ratio = $(Ms)_{nanocubes}/(Ms)_{nanospheres}$
[2]H ratio = $(H)_{nanocubes}/(H)_{nanospheres}$

For the collection of the GMR data, ~4.9×10^{10} MNPs were deposited on the GMR sensor and the change in peak-to-peak distance was recorded. A typical sensor response is illustrated in Figure 3.4 showing the peak-to-peak distance (Delta x) in the absence and presence of MNPs. For cubic MNPs, Delta x was ~18 ± 9 Oe and was

observed to be higher than the ~4 ± 5 Oe obtained for the spherical MNPs of same volume. Data from five sensors were used to calculate the average in each case. The experiment was carried out with the same particle count for both cubic and spherical MNPs, but since this is not specific binding, the same coverage on each sensor could not be confirmed. However, it is likely that the cubic shape improves sensor surface contact.

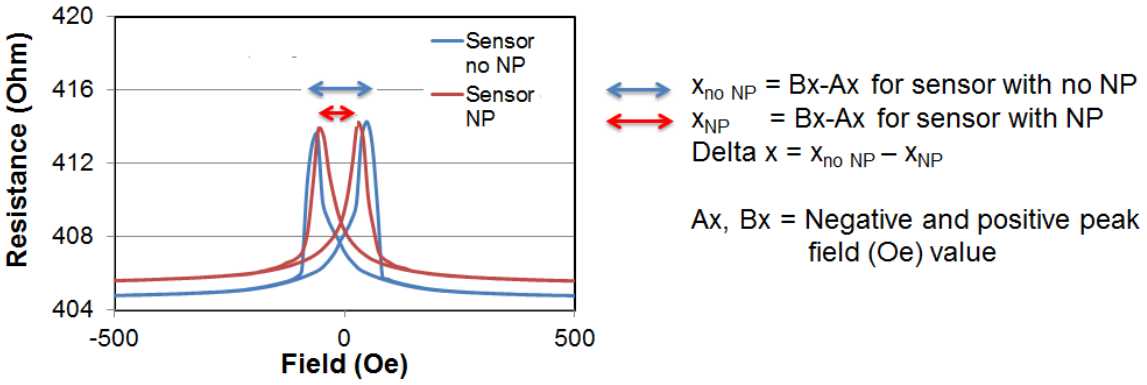

Figure 3.4 Plot of a typical response of a GMR sensor in the absence and presence of magnetic nanoparticles. The data shown is for 135 nm cubic Fe_3O_4 on one sensor.

In the FIRMS technique, the non-bound nanoparticles were removed from the surface at increasing centrifuge speeds (that is increasing force). The magnetization on the y-axis corresponds to the number of nanoparticles that are present on the surface. Figure 3.5a shows that at every speed tested, the magnetization of the nanocubes left on the surface is higher than that of the nanospheres. The samples chosen were of the same body diagonal/diameter; a higher volume and mass for each nanocube as compared to the nanospheres and hence a lower number of cubic nanoparticles as compared to spherical.

Figure 3.5b demonstrates that although the initial number of nanocubes was lower (2.1×10^{10}) than that of the nanospheres (4.2×10^{10}), the number of nanocubes after centrifugation at 3000 and 5000 rpm is about 1.75 times higher than that of the

nanospheres. More nanocubes than nanospheres remained on the surface after application of a force corresponding to 3000 and 5000 rpm (~15 and 25 fN, respectively). At 9000 rpm (~46 fN), the apparent binding advantage of the nanocubes, though marginal, was still evident. This preliminary study demonstrates that the nanocubes require a stronger force to break them away from the surface as compared to the nanospheres.

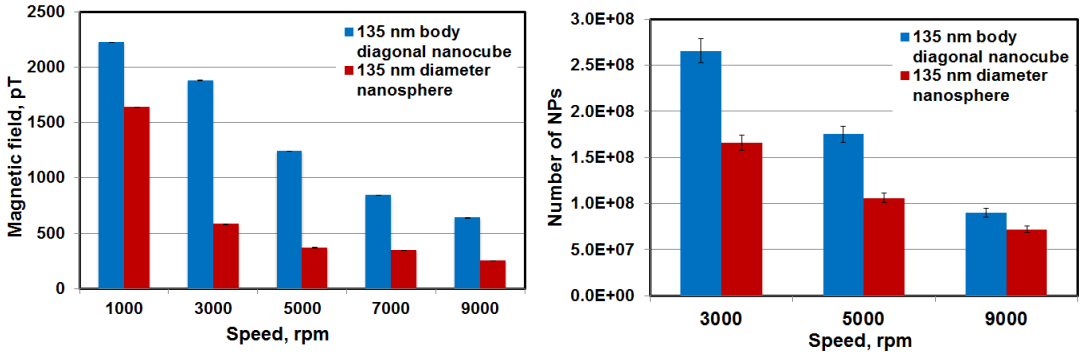

Figure 3.5 (a) Magnetization profiles in pico-Tesla versus centrifuge speed in revolutions per minute (rpm) for nanocubes and nanospheres of 135 nm (body diagonal and diameter, respectively) (b) Number of particles on the sensor after centrifugation at 3000, 5000, and 9000 rpm. Initial number of particles are in the text.

As a component part of the nanoparticle characterization process, I examined the TEM images of one pair of same-volume MNPs and one pair of same-body diagonal/diameter MNPs. These images are shown in Figure 3.6 and they reveal that the nanocubes (a,c) are monocrystalline and the nanospheres (b,d) are polycrystalline.

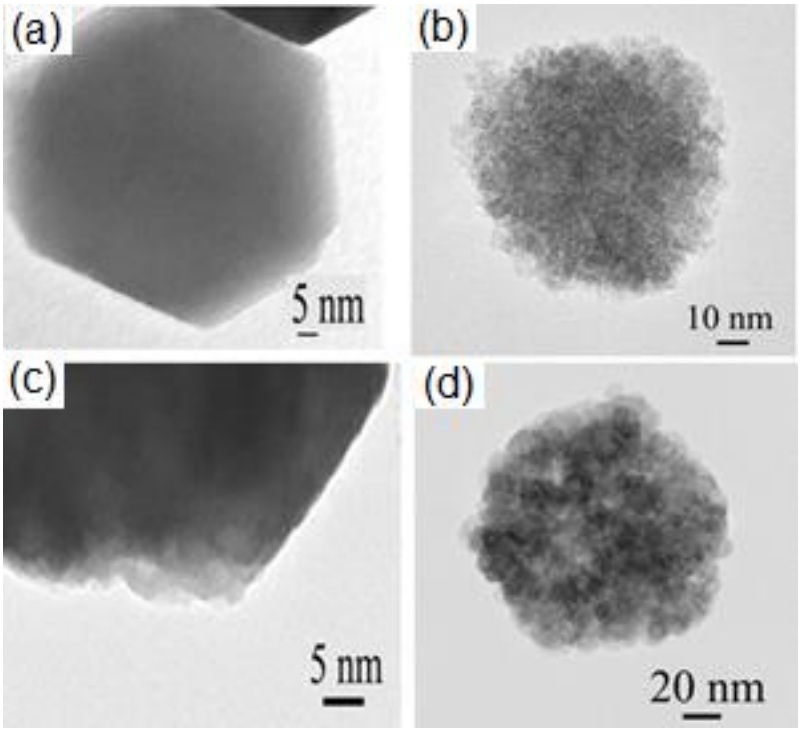

Figure 3.6 TEM images of (a) 150 nm cubic Fe_3O_4 MNPs, (b) 100 nm spherical Fe_3O_4 MNPs, (c) 135 nm cubic Fe_3O_4 MNPs, and (d) 135 nm spherical Fe_3O_4 MNPs.

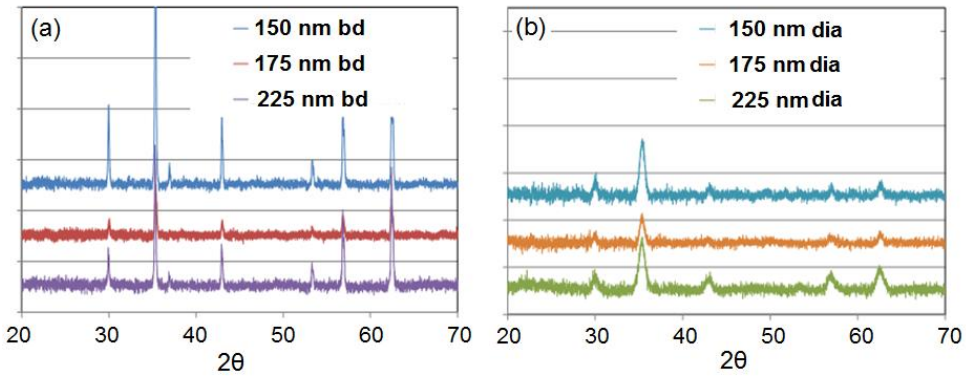

Figure 3.7 XRD patterns for Fe_3O_4 (a) nanocubes and (b) nanospheres.

In order to develop quantitative data for the degree of crystallinity for these samples, I evaluated and compared the XRD patterns of the cubic and spherical Fe_3O_4 MNPs. Figure 3.7 shows that the cubic MNPs exhibited much sharper peaks as

compared to the broad peaks associated with the spherical MNPs. To evaluate the crystallinity of the MNPs on a quantitative basis, I calculated the crystallite size. This parameter is inversely proportional to the peak width based upon Scherrer's formula, as shown in Equation 3.1.[51]

$$\text{Crystallite size} = (K.\ \lambda)/(\beta \cos 2\theta) \quad (3.1)$$

where K = shape factor
λ = wavelength (0.154 nm)
β = line broadening at ½ the maximum intensity (rad)
θ = Bragg angle

The broad peaks of the spherical MNPs as compared to the sharp peaks for the cubic MNPs indicate that the crystallite size of the cubic sample is larger as compared to the spherical samples. The crystallinity index (IC) value was calculated for the nanocubes and nanospheres using Equation 3.2.[52]

$$\text{IC} = [(\text{MNP size by SEM/TEM})/(\text{Crystallite size})] \times 100 \quad (3.2)$$

The crystallite size and the crystallinity index of one pair each of the same-volume and same-body-diagonal/diameter Fe_3O_4 MNPs are listed in Table 3.3. The XRD data complemented the TEM images and showed that the cubic Fe_3O4 MNPs had a higher degree of crystallinity as compared to the spherical Fe_3O_4 MNPs. A crystallinity index close to 1 indicates a completely monocrystalline crystal.

Table 3.3 Comparison of the Crystallite Size and the Crystallinity Index for the Fe_3O_4 Nanocubes and Nanospheres Shown in Figure 3.4

MNP Shape	Size (nm)	Basis	Crystallite Size (nm)	Crystallinity Index
Cube	150	Same volume	56	3
Sphere	100		15	7
Cube	175	Same body diagonal/diameter	83	2
Sphere	125		12	11

This difference in the crystallinity of the synthesized nanocubes and nanospheres led to an effort to generate additional MNPs. I varied the surfactant (oleic acid) concentration and carried out liquid reduction synthesis at temperatures matching the solvothermal process (290 °C) in order to obtain spherical MNPs with a high degree of crystallinity, but these efforts have thus far been unsuccessful. Cubic nanoparticles have a higher magnetization and coercivity than their spherical counterparts in this size range, considered both on a same-volume and same-body diagonal/diameter basis. However, unless the comparison is made on cubic and spherical MNPs of equivalent crystallinity, the enhanced magnetic properties of the nanocubes, as compared to the nanospheres, cannot be attributed to shape alone.

3.4 Conclusions

For applications relying on both higher contact area and higher magnetization and coercivity, monocrystalline Fe_3O_4 nanocubes offer a distinct advantage over

polycrystalline Fe_3O_4 nanospheres of the same-volume or same-body diagonal/diameter. Preliminary data using a GMR sensor and the FIRMS technique confirm this advantage for the nanocubes over the nanospheres. The reason for the advantage has not been clearly established, with this current report showing that both shape and crystallinity play a role in defining the magnetic properties of MNPs. Additionally, the ability to synthesize magnetic nanospheres of equivalent crystallite size to nanocubes (MNPs in the multi-domain range) has been brought into question. These results should be taken into consideration when planning research projects where larger magnetic nanoparticles are required.

3.5 References

(1) Tran, N.; Webster, T. J. *J. Mater. Chem.* **2010**, *20*, 8760–8767.

(2) Roca, A. G.; Costo, R.; Rebolledo, A. F.; Veintemillas-Verdaguer, S.; Tartaj, P.; Gonzalez-Carreno, T.; Morales, M. P.; Serna, C. J. *J. Phys. D: Appl. Phys.* **2009**, *42*, 224002–224011.

(3) Thiesen, B.; Jordan, A. *Int. J. Hyperthermia* **2008**, *24*, 467–474.

(4) Arruebo, M.; Fernandez-Pacheco, R.; Ibarra, M.; Santamaria, J. *Nanotoday* **2007**, *2*, 22–32.

(5) Neuberger, T.; Schoepf, B.; Hofmann, H.; Hofmann, M.; Von, R. B. *J. Magn. Magn. Mater.* **2005**, *293*, 483–496.

(6) Huang, S.; Juang, R. *J. Nanopart. Res.* **2011**, *13*, 4411–4430.

(7) Moerup, S.; Frandsen, C.; Hansen, M. F.; The Oxford Handbook of NanoScience and Technology, Oxford University Press, **2010**; *2*, 713–744.

(8) Mueller, R.; Dutz, S.; Neeb, A.; Cato, A. C. B.; Zeisberger, M. *J. Magn. Magn. Mater.* **2013**, *328*, 80–85.

(9) Caruntu, D.; Caruntu, G.; O'Connor, C. J. *J. Phys. D: Appl. Phys.* **2007**, *40*, 5801–5809.

(10) Guardia, P.; Labarta, A.; Batlle, X. *J. Phys. Chem. C* **2011**, *115*, 390–396.

(11) Lu, H. M.; Zheng, W. T.; Jiang, Q. *J. Phys. D: Appl. Phys.* **2007**, *40*, 320–325.

(12) Chinnasamy, C.; Herr, J.; Pai, R.; Cui, B.; Li, W.; Liu, J. *J. Appl. Phys.* **2012**, *111*, 07B539/531–533.

(13) Gabal, M. A.; Angari, A. Y. M.; Kadi, M. W. *Polyhedron* **2011**, *30*, 1185–1190.

(14) Kuhn, L. T.; Bojesen, A.; Timmermann, L.; Fauth, K.; Goering, E.; Johnson, E.; Nielson, M. M.; Morup, S. *J. Magn. Magn. Mater.* **2004**, *272*, 1485–1486.

(15) Luis, F.; Bartolome, F.; Petroff, F.; Bartolome, J.; Garcia, L. M.; Deranlot, C.; Jaffres, H.; Martinez, M. J.; Bencok, P.; Wilhelm, F.; Rogalev, A.; Brookes, N. B. *Europhys. Lett.* **2006**, *76*, 142–148.

(16) Singh, V.; Srinivas, V.; Ranot, M.; Angappane, S.; Park, J.-G. *Phys. Rev. B: Condens. Matter Mater. Phys.* **2010**, *82*, 054417–054419.

(17) Gao, G.; Liu, X.; Shi, R.; Zhou, K.; Shi, Y.; Ma, R.; Takayama-Muromachi, E.; Qiu, G. *Cryst. Growth Des.* **2010**, *10*, 2888–2894.

(18) Leem, G.; Sarangi, S.; Zhang, S.; Rusakova, I.; Brazdeikis, A.; Litvinov, D.; Lee, T. R. *Cryst. Growth Des.* **2009**, *9*, 32–34.

(19) Kim, D.; Lee, N.; Park, M.; Kim, B. H.; An, K.; Hyeon, T. *J. Am. Chem. Soc.* **2009**, *131*, 454–455.

(20) Yan, M.; Fresnais, J.; Berret, J. F. *Condens. Matter* **2010**, 1–15.

(21) Wu, C.-G.; Lin, H. L.; Shau, N.-L. *J. Solid State Electrochem.* **2006**, *10*, 198–202.

(22) Srikala, D.; Singh, V. N.; Banerjee, A.; Mehta, B. R.; Patnaik, S. *J. Nanosci. Nanotechnol.* **2009**, *9*, 5627–5632.

(23) Comesana-Hermo, M.; Ciuculescu, D.; Li, Z.-A.; Stienen, S.; Spasova, M.; Farle, M.; Amiens, C. *J. Mater. Chem.* **2012**, *22*, 8043–8047.

(24) Schladt, T. D.; Shukoor, M. I.; Schneider, K.; Tahir, M. N.; Natalio, F.; Ament, I.; Becker, J.; Jochum, F. D.; Weber, S.; Kohler, O.; Theato, P.; Schreiber, L. M.; Sonnichsen, C.; Schroder, H. C.; Muller, W. E. G.; Tremel, W. *Angew. Chem. Int. Ed. Engl.* **2010**, *49*, 3976–3980.

(25) Dovgolevsky, E.; Haick, H. *Small* **2008**, *4*, 2059–2066.

(26) He, X.; Shi, H. *Particuology* **2012**, *10*, 497–502.

(27) Montferrand, C. d.; Hu, L.; Milosevic, I.; Russier, V.; Bonnin, D.; Motte, L.; Brioude, A.; Lalatonne, Y. *Acta Biomater.* **2013**, *9*, 6150–6157.

(28) Song, Q.; Zhang, Z. J. *J. Am. Chem. Soc.* **2004**, *126*, 6164–6168.

(29) Salazar-Alvarez, G.; Qin, J.; Sepelak, V.; Bergmann, I.; Vasilakaki, M.; Trohidou, K. N.; Ardisson, J. D.; Macedo, W. A. A.; Mikhaylova, M.; Muhammed, M.; Baro, M. D.; Nogues, J. *J. Am. Chem. Soc.* **2008**, *130*, 13234–13239.

(30) Zhen, G.; Muir, B. W.; Moffat, B. A.; Harbour, P.; Murray, K. S.; Moubaraki, B.; Suzuki, K.; Madsen, I.; Agron-Olshina, N.; Waddington, L.; Mulvaney, P.; Hartley, P. G. *J. Phys. Chem. C* **2011**, *115*, 327–334.

(31) Chou, S.-W.; Zhu, C.-L.; Neeleshwar, S.; Chen, C.-L.; Chen, Y.-Y.; Chen, C.-C. *Chem. Mater.* **2009**, *21*, 4955–4961.

(32) Liu, Y.; Tan, J.; Thomas, A.; Ou-Yang, D.; Muzykantov, V. R. *Ther. Delivery* **2012**, *3*, 181–194.

(33) Decuzzi, P.; Ferrari, M. *Biomaterials* **2006**, *27*, 5307–5314.

(34) Decuzzi, P.; Pasqualini, R.; Arap, W.; Ferrari, M. *Pharm. Res.* **2009**, *26*, 235–243.

(35) Sau, T. K.; Rogach, A. L. *Adv. Mater.* **2010**, *22*, 1781–1804.

(36) Noh, S.H.; Na, W.; Jang, J.T.; Lee, J.H.; Lee, E.J.; Moon, S.H.; Lim, Y.; Shin, J.S.; Cheon, J. *Nano Lett.*, *12*, 3716–3721.

(37) Kolhatkar, A. G.; Nekrashevich, I.; Litvinov, D.; Willson, R. C.; Lee, T. R. *Chem. Mater.* **2013**, *25*, 1092–1097.

(38) Jovic, N.; Prekajski, M.; Kremenovic, A.; Jancar, B.; Kahlenberg, V.; Antic, B. *J. Appl. Phys.* **2012**, *111*, 034313–034315.

(39) Deraz, N. M. *J. Alloys Compd.* **2010**, *501*, 317–325.

(40) Chia, C. H.; Zakaria, S.; Yusoff, M.; Goh, S. C.; Haw, C. Y.; Ahmadi, S.; Huang, N. M.; Lim, H. N. *Ceram. Int.* **2010**, *36*, 605–609.

(41) Mozaffari, M.; Manouchehri, S.; Yousefi, M. H.; Amighian, J. *J. Magn. Magn. Mater.* **2009**, *322*, 383–388.

(42) Kolhatkar, A. G.; Jamison, A. C.; Litvinov, D.; Willson, R. C.; Lee, T. R. *Int. J. Mol. Sci.* **2013**, *14*, 1–34.

(43) Krishnan, K. M. *IEEE Trans. Magn.* **2010**, *46*, 2523–2558.

(44) Jeong, U.; Teng, X.; Wang, Y.; Yang, H.; Xia, Y. *Adv. Mater*. **2007**, *19*, 33–60.

(45) Yang, H.; Ogawa, T.; Hasegawa, D.; Takahashi, M. *J. Appl. Phys.* **2008**, *103*, 07D526/521–507D526/523.

(46) Deng, H.; Li, X.; Peng, Q.; Wang, X.; Chen, J.; Li, Y. *Angew. Chem., Int. Ed.* **2005**, *44*, 2782–2785.

(47) Litvinov, D.; Willson, R.; Wolfe, J.C.; WO2007014322A3, University of Houston, USA . 2007.

(48) Yao, L.; Xu, S. *Angew. Chem., Int. Ed.* **2011**, *50*, 4407–4409.

(49) Yu, D.; Ruangchaithaweesuk, S.; Yao, L.; Xu, S. *J. Nanopart. Res.* **2012**, *14*, 1135/1131–1135/1139.

(50) Yao, L.; Xu, S. *J. Phys. Chem. B* **2012**, *116*, 9944–9948.

(51) Kose, H.; Aydin, A.O.; Akbulut, H. *Acta Phys. Pol. A* **2014**, *125*, 345–347.

(52) Sahai, A.; Goswami, N. *Phys. E* **2014**, *58*, 130–137.

Chapter 4

Enzymatic Conversion of Magnetic Nanoparticles to a Non-magnetic Precipitate

4.1 Motivation

Magnetic nanoparticles (MNPs) are commonly used in off-line sample capture, cleanup, and concentration, and as labels for sensitive biomolecule detection.[1] In contrast to optical labels, magnetic labels eliminate concerns about photobleaching and can be potentially more sensitive even in the presence of turbidity due to the absence of magnetic background in biological samples. The application of giant magnetoresistive (GMR) sensors to biomolecular recognition was pioneered by Baselt *et al.* in 1998.[2] In a GMR sensor, magnetic particles are functionalized, attached to biomarkers, and detected by the change in resistance of the magnetoresistive elements of the GMR. There are several research groups[4-10] that have focused on development of magnetic sensor technologies at the micrometer scale. Commercial magnetic immunoassays include MagArray (GMR-based - utilizing 50 nm magnetic nanotags),[11] MagniSense (reader that registers nonlinear particle magnetization signature - utilizing 50 nm paramagnetic particles),[12] and MagnaBiosciences (lateral flow assays utilizing 60-380 nm paramagnetic particles).[13]

Conventional enzyme-linked immunosorbent assays (ELISA) using alkaline phosphatase (AP) as the reporter rely on dephosphorylation of the substrate to form a product that can be detected by its absorbance, fluorescence, or luminescence. In cases

where an insoluble colored product is required for detection, bromochloroindoyl phosphate-nitroblue tetrazolium (BCIP-NBT), which forms a blue precipitate/chromophore on dephosphorylation, can be used as a substrate.[14,15] Based on the widely used silver enhancement ("silver staining"), AP has been used to produce metallic silver by reduction of silver ions utilizing a reducing agent that is only formed after the AP-catalyzed dephosphorylation of a substrate (e.g., phosphorylated L-ascorbic acid,[16] *p*-aminophenyl phosphate,[17] or 3-indoxyl phosphate[18]).[19-21] Using a similar approach, our group recently demonstrated the enzymatic synthesis of MNPs in which AP catalyzed the dephosphorylation of phosphorylated L-ascorbic acid to L-ascorbic acid, which then served as a reducing agent for salts of iron, gadolinium, and holmium, and formed magnetic precipitates of $Fe_{45\pm14}Gd_{5\pm2}O_{50\pm15}$ and $Fe_{42\pm4}Ho_{6\pm4}O_{52\pm5}$. These studies will be described in detail in Chapter 5. These MNPs demonstrate the potential for structuring assays that produce a magnetic signal in response to the presence of a specific enzymatic response.

L-ascorbic acid has also been used to reduce other salts such as Ag, Au, Pt, Pd, Cu, Co, Fe, and Mo to yield nanoparticles of Ag, Au, Pt, Pd, Cu, Co_3O_4, Fe_2O_3, and MoO_2, respectively.[19-22] However, these other reports do not indicate the development of magnetic products. For example, during the synthesis of Fe_3O_4 nanoparticles via reduction of ferric chloride by L-ascorbic acid, Lv *et al.* serendipitously observed that an excess of L-ascorbic acid did not result in the formation of Fe_3O_4 MNPs since the excess L-ascorbic acid likely reduced the Fe^{+3} in the synthesized-Fe_3O_4 as well.[23] The fate of the elemental components in this effort to produce MNPs does point to the possible

development of a system where the magnetic component loses its magnetism through a reduction process.

Concurrently, albeit in another area, there is a focus on studying iron availability and cycling and parallel research to study the fate of iron oxides in the environment is ongoing. Nanoscale iron oxides (e.g., ferrihydrite, hematite, goethite) are ubiquitous in nature and their fate in the environment is a result of their chemical reactivity. Several studies used ascorbic acid as a model compound to study reductive dissolution of these nanoparticles in the environment.[24-26] In all cases (varying size, pH, morphology), insoluble Fe^{+3} was reduced to soluble Fe^{+2} in the presence of ascorbic acid. We wanted to confirm the reducing ability of L-ascorbic acid to reduce pre-synthesized Fe_3O_4 MNPs chemically (using L-ascorbic acid as purchased from a chemical supplier) and enzymatically (using L-ascorbic acid formed *in situ*). In our system, AP catalyzes the dephosphorylation of L-ascorbic-2-phosphate to L-ascorbic acid, which then serves as a reducing agent for Fe_3O_4 MNPs. In this chapter, we report the first use of enzymes to convert MNPs to a non-magnetic precipitate, with the aim of changing/reducing the resistance that is registered using a GMR – an elegant approach that should prove to be useful in biosensing.

4.2 Materials and Methods

The chemicals used in the syntheses outlined below were of analytical grade and were used as received from the supplier without further purification. Purified water (resistivity of >18 MΩ-cm) from a Milli-Q water system was used in the synthesis and washing steps.

4.2.1 Chemical and Enzymatic Reduction of Fe_3O_4 MNPs

The ascorbic acid (aa) utilized in these experiments was either a purchased chemical ("chemical synthesis" approach) or an enzymatically produced chemical via dephosphorylation of L-ascorbic acid 2-phosphate sesquimagnesium salt hydrate (p-aa) by alkaline phosphatase (AP) ("enzymatic synthesis" approach). Samples of AP were obtained from Sigma (catalog # P6774; 0.049 ml; 3531 units/mg protein and 13 mg protein/ml). One unit activity of AP is defined to hydrolyze 1 μmole of substrate (4-nitrophenyl phosphate) per minute at pH 9.8 at 37 °C. Zeba desalting columns (7K MWCO from Thermo Fisher Scientific) were used to remove more than 95% (column specification) of the salts (5 mM $MgCl_2$ and 0.2 mM $ZnCl_2$) present in the AP solution. The enzyme was then resuspended in 100 μL diethanolamine buffer (pH 9.8) containing 5 mM $MgNO_3$ and 0.25 mM $ZnNO_3$ to give a final concentration of 60 units AP/mL. In a 50-mL centrifuge tube, 0.25 ml of 1 mg/ml 100-nm Fe_3O_4 MNPs was added to 5 ml of purified water. For chemical or enzymatic conversion, 0.1 g (0.6 mmol) of aa or 0.1 g (0.3 mmol) of p-aa, respectively, were added to the salt solution. In the case of enzymatic conversion, 5 μL of 60 units/mL AP enzyme was added to the centrifuge tube containing the metal salts. The experiment was carried out at 20 °C (room temperature).

4.2.2 Synthesis of Spherical Fe_3O_4 MNPs

Our modified recipe of the procedure reported by Deng *et al.*[27] yielded spherical Fe_3O_4 nanoparticles with diameters of 100 nm. This synthesis involved sequentially dissolving iron chloride (1.4 g, $FeCl_3 \cdot 6H_2O$) and sodium acetate (3.6 g) in 15 mL of ethylene glycol. The solution was stirred for an additional 30 min and then injected at once

into a round-bottomed flask containing a vigorously stirred solution of PVP (0.40 g) in 35 mL of ethylene glycol heated to and kept at 180 °C. The mixture was then vigorously stirred for 4–24 hours during which a black precipitate was obtained. The black precipitate was washed multiple times with ethanol and purified water and dried under vacuum at room temperature.

4.2.3 Characterization by SEM, XRD, EDX, and VSM

MNPs and the non-magnetic precipitate were characterized by scanning electron microscopy (SEM; LEO-1525 operating at 15 kV and equipped with an energy-dispersive X-ray spectrometer, EDX), vibrating sample magnetometry (VSM PPMS, Quantum Design EverCool II), and X-ray diffractometry (XRD; Siemens D5000 X-ray diffractometer). For the SEM analyses, we deposited the MNPs or non-magnetic precipitate on a silicon wafer and allowed the samples to dry. We used EDX and XRD to confirm the composition of the samples. For the XRD studies, a concentrated sample of nanoparticles in ethanol was deposited on a piranha-cleaned glass slide, and XRD was carried out using Cu Kα radiation ($\lambda = 1.540562$ Å) in the 2θ range from 0 to 90°. The magnetic properties (saturation magnetization, residual magnetization, coercivity, and blocking temperature) of a known mass of sample were measured using VSM. Saturation magnetization and coercivity were obtained from an analysis of the hysteresis loop for data collected at 300 K.

4.3 Results and Discussion

In our initial efforts, prior to evaluating the enzymatic conversion of MNPs to a non-magnetic precipitate, we used L-ascorbic acid (as supplied) to evaluate the efficiency

of the reduction of the Fe_3O_4 MNPs. In the presence of L-ascorbic acid, the black-brown colored Fe_3O_4 MNP solution (0.25 ml of 0.001 g/ml Fe_3O_4 MNPs suspended in 5 mL purified water) became completely clear in about 2 hours. In the enzymatic process, the solution did not become clear and a white precipitate was observed. The white precipitate was characterized using the various methods described below. The SEM images of the Fe_3O_4 MNPs and enzymatically-converted-to-non-magnetic NPs are shown in Figure 4.1. When the chemical L-ascorbic acid was used as purchased for the MNP reduction, Fe^{+3} was reduced to soluble Fe^{+2} producing a particle decomposition with no precipitate, therefore there is no image to report for the chemically-converted Fe_3O_4 MNPs. The elemental composition of the non-magnetic precipitate from the enzymatic procedure was obtained using SEM/EDX and the composite EDX spectrum is shown in Figure 4.2. This SEM/EDX spectrum was the average of data collected for 5 samples. The EDX data shows that the non-magnetic nanoparticles obtained from enzymatic conversion of the 100 nm Fe_3O_4 MNPs were composed of $Fe_{27\pm5}O_{73\pm5}$.

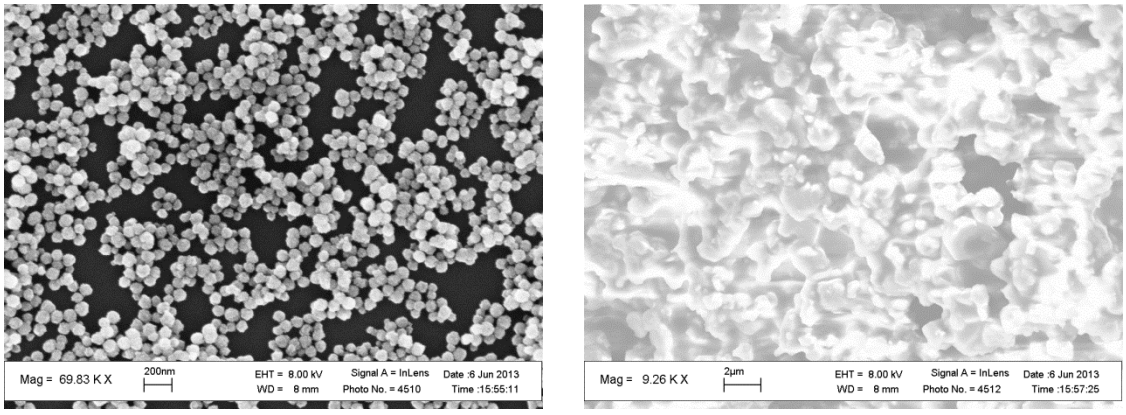

Figure 4.1 SEM Images of (a) the 100-nm Fe_3O_4 MNPs and (b) the non-magnetic precipitate obtained from enzymatic conversion of the 100 nm Fe_3O_4 MNPs

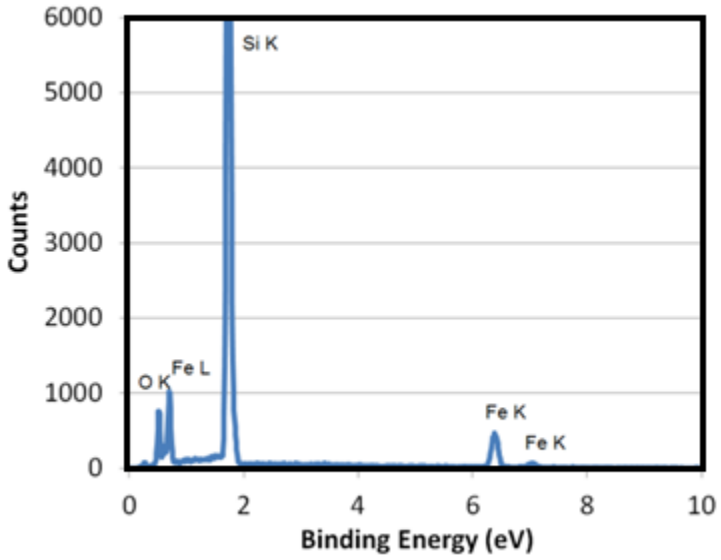

Figure 4.2 Composition of the nanoparticles using SEM-EDX for the enzymatically formed non-magnetic precipitate from the 100-nm Fe_3O_4 MNPs.

Figure 4.3 compares the XRD patterns of the Fe_3O_4 MNPs and the enzymatically-synthesized non-magnetic precipitate. The MNP XRD pattern confirms that the MNP samples are Fe_3O_4 based upon comparison to the Fe_3O_4 pattern in the Inorganic Crystal Structure Database (ICSD). We characterized the non-magnetic precipitate using XRD and compared it to the magnetic Fe_3O_4, as shown in Figure 4.3. Comparison of the XRD patterns confirms that the non-magnetic precipitate is distinctly different from the Fe_3O_4 MNPs before reduction.

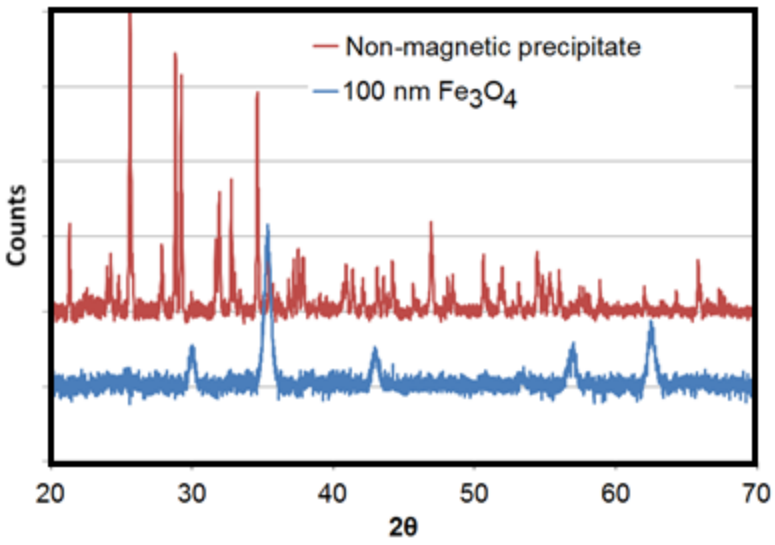

Figure 4.3 Comparison of XRD patterns of the non-magnetic precipitate by enzymatic reduction of 100 nm Fe_3O_4 MNPs as compared to the 100 nm Fe_3O_4 MNPs.

We also calculated elemental mass balances on the conversion process. Based on the experimental protocol described previously, 27 µg of 0.9 units of AP protein (Sigma catalog # P6774: 0.049 ml containing 13 mg protein/ml and 3531 units/mg protein) dephosphorylated phosphorylated L-ascorbic acid to yield L-ascorbic acid that reduced 100-nm Fe_3O_4 MNPs (weight % ratio of Fe:O of 72:28) to obtain 0.0005 g non-magnetic $Fe_{27\pm5}O_{73\pm5}$ with weight % ratio of Fe:O of 56±5:44±5.

Figure 4.4 shows the magnetic properties of the Fe_3O_4 MNPs obtained using VSM. The saturation magnetization and coercivity of the 100 nm Fe_3O_4 MNPs were 70 emu/g and 23 G, respectively. The MNPs were enzymatically reduced to yield a precipitate that was not magnetic at room temperature (not attracted to a bar magnet) and exhibited no measurable saturation magnetization.

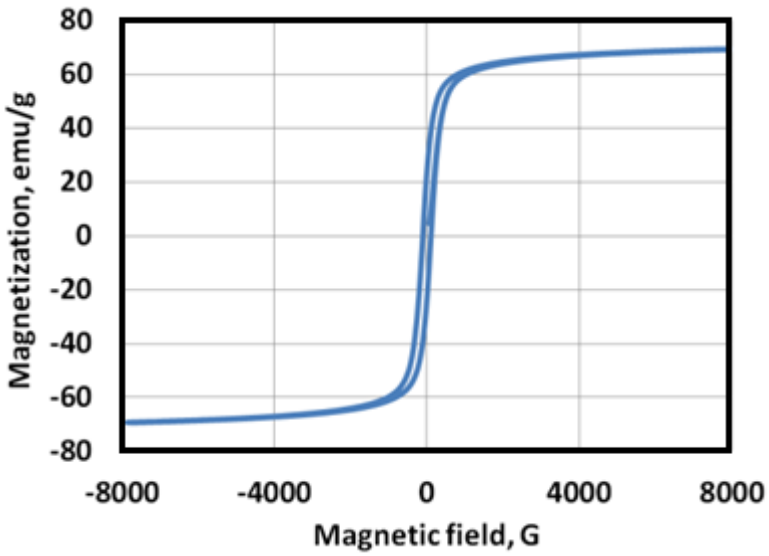

Figure 4.4 Magnetization curves recorded at 300 K for the 100 nm Fe_3O_4 MNPs.

The precipitated particles can be readily detected as "loss of signal" on our in-house giant magnetoresistive sensor (GMR), which with a sensitivity of 10^{-13} emu is designed to detect one Fe_3O_4 MNP possessing a saturation magnetization of 70 emu/g.[2,28,29]

4.4 Conclusions

The strategy outlined in this chapter offers a novel approach to magnetic sensing in which dephosphorylation of phosphorylated L-ascorbic acid by AP yields L-ascorbic acid that converts magnetic Fe_3O_4 MNPs to a non-magnetic product *in situ* in the course of the assay, thus providing a "loss of signal" option in a sensing device.

4.5 References

(1) Mani, V.; Chikkaveeraiah, B. V. *Expert Opin. Med. Diagn.* **2011**, *5*, 381–391.

(2) Baselt, D. R.; Lee, G. U.; Natesan, M.; Metzger, S. W.; Sheehan, P. E.; Colton, R. J. *Biosens. Bioelectron.* **1998**, *13*, 731–739.

(3) Li, Y.; Srinivasan, B.; Jing, Y.; Yao, X.; Hugger, M. A.; Wang, J. P.; Xing, C. *J. Am. Chem. Soc.* **2010**, *132*, 4388–4392.

(4) Srinivasan, B.; Li, Y.; Jing, Y.; Xu, Y.-H.; Yao, X.; Xing, C.; Wang, J.-P. *Angew. Chem., Int. Ed.* **2009**, *48*, 2764–2767.

(5) Srinivasan, B.; Li, Y.; Jing, Y.; Xing, C.; Slaton, J.; Wang, J.-P. *Anal. Chem.* **2011**, *83*, 2996–3002.

(6) Hall, D. A.; Gaster, R. S.; Lin, T.; Osterfeld, S. J.; Han, S.; Murmann, B.; Wang, S. X. *Biosens. Bioelectron.* **2010**, *25*, 2051–2057.

(7) Osterfeld, S. J.; Yu, H.; Gaster, R. S.; Caramuta, S.; Xu, L.; Han, S. J.; Hall, D. A.; Wilson, R. J.; Sun, S.; White, R. L.; Davis, R. W.; Pourmand, N.; Wang, S. X. *Proc. Natl. Acad. Sci.* **2008**, *105*, 20637–20640.

(8) Hall, D. A.; Wang, S. X.; Murmann, B.; Gaster, R. S. *Conf. Proc. (Midwest Symp Circuits Syst.)* **2010**, 1779–1782.

(9) Gaster, R. S.; Hall, D. A.; Nielsen, C. H.; Osterfeld, S. J.; Yu, H.; Mach, K. E.; Wilson, R. J.; Murmann, B.; Liao, J. C.; Gambhir, S. S.; Wang, S. X. *Nature Medicine* **2009**, *15*, 1327–1332.

(10) Xu, L.; Yu, H.; Akhras, M. S.; Han, S.-J.; Osterfeld, S.; White, R. L.; Pourmand, N.; Wang, S. X. *Biosens. Bioelectron.* **2008**, *24*, 99–103.

(11) Orlov, A. V.; Khodakova, J. A.; Nikitin, M. P.; Shepelyakovskaya, A. O.; Brovko, F. A.; Laman, A. G.; Grishin, E. V.; Nikitin, P. I. *Anal. Chem.* **2013**, *85*, 1154–1163.

(12) Peck, R. B.; Schweizer, J.; Weigl, B. H.; Somoza, C.; Silver, J.; Sellors, J. W.; Lu, P. S. *Clin. Chem.* **2006**, *52*, 2170–2172.

(13) Eadie, M. J.; Tyrer, J. H.; Kukums, J. R.; Hooper, W. D. *Histochemie* **1970**, *21*, 170–180.

(14) Altman, F. P. *Histochemie* **1974**, *38*, 155–171.

(15) Cacao, E.E. PhD Dissertation, University of Houston, Houston, TX, 2012.

(16) Wu, J.; Chumbimuni-Torres, K. Y.; Galik, M.; Thammakhet, C.; Haake, D. A.; Wang, J. *Anal. Chem.* **2009**, *81*, 10007–10012.

(17) Fanjul-Bolado, P.; Hernandez-Santos, D.; Gonzalez-Garcia, M. B.; Costa-Garcia, A. *Anal. Chem.* **2007**, *79*, 5272–5277.

(18) Khorasani-Motlagh, M.; Noroozifar, M.; Shahroosvand, H. *J. Iran. Chem. Soc.* **2010**, *7*, S113–S122.

(19) Murugadoss, A.; Pasricha, R.; Chattopadhyay, A. *J. Colloid Int. Sci.* **2007**, *311*, 303–310.

(20) Nadagouda, M. N.; Varma, R. S. *Cryst.Growth Des.* **2007**, *7*, 2582–2587.

(21) Yu, W.; Xie, H.; Chen, L.; Li, Y.; Zhang, C. *Nanoscale Res. Lett.* **2009**, *4*, 465–470.

(22) Lv, Y.; Wang, C.; Wang, X.; Bai, J. *J. Cryst. Growth* **2009**, *311*, 3445–3450.

(23) Debnath, S.; Hausner, D.; Strongin, D.; Kubicki, J. *J. Colloid Int. Sci.* **2010**, *341*, 215–223.

(24) Lanzl, C.; Baltrusaitis, J.; Cwiertny, D. M. *Langmuir* **2012**, *29*, 15797−15808.

(25) Echigo, T.; Aruguete, D. M.; Murayama, M.; Hochella, M. F. *Geochimica et Cosmochimica Acta* **2012**, *90*, 149–162.

(26) Deng, H.; Li, X.; Peng, Q.; Wang, X.; Chen, J.; Li, Y. *Angew. Chem., Int. Ed.* **2005**, *44*, 2782–2785.

(27) Kolhatkar, A. G.; Nekrashevich, I.; Litvinov, D.; Willson, R. C.; Lee, T. R. *Chem. Mater.* **2013**, *25*, 1092–1097.

(28) Wirix-Speetjens, R.; Reekmans, G.; De, P. R.; Liu, C.; Laureyn, W.; Borghs, G. *Sens. Actuators B* **2007**, *128*, 1–4.

Chapter 5

Enzymatic Synthesis of Magnetic Nanoparticles

5.1 Motivation

Interest in magnetic biosensing has increased over the past decade. Magnetic nanoparticles (MNPs), commonly used in sample capture, clean-up, and concentration, now also are evaluated as labels for sensitive biomolecule detection[1] since they are not affected by photobleaching or turbidity and magnetic background in complex biological samples is absent. The application of giant magnetoresistive (GMR) sensors and MNP labels to bioassays and diagnostics was first suggested by Shieh & Ackley in 1996 and then described by Baselt *et al.* in 1998.[2,3] This approach is attractive because of the solid-state and potentially low-cost nature of the sensors, and the absence of concerns associated with photobleaching, scattering, and fouling. Research groups at the University of Minnesota [4-6] and at Stanford University,[7-10] have reported micrometer-scale magnetic sensors for ultrasensitive protein detection in complex samples. Moreover, several magnetic immunoassays integrated with proprietary readers have been commercialized, including those from MagArray,[11] MagniSense,[12] and MagnaBiosciences.[13]

Conventional enzyme-linked immunosorbent assays (ELISAs) rely on modification of the substrate to form a detectable product that absorbs, fluoresces, or luminesces. For example, p-nitrophenyl phosphate is dephosphorylated by alkaline phosphatase (AP) to form a soluble yellow product (p-nitro phenol) detected at 405 nm

using a spectrophotometer. The substrates 4-methylumbelliferyl phosphate (4-MUP) and 3-(2'-spiroadamantane)-4-methyl-4-(3'-phosphoryloxyphenyl-1, 2-dioxetane, disodium salt (AMPPD) are likewise dephosphorylated by AP to their fluorescent and luminescent products, respectively. Where an insoluble colored product is necessary, AP dephosphorylation of bromochloroindoyl phosphate-nitroblue tetrazolium (BCIP-NBT) leads to formation of a blue precipitate/chromophore.[14,15] Enzymes also can produce silver, as in silver staining using the redox chemistry upon which black and white photography has been based. Silver ions are reduced to elemental silver in the presence of a reducing agent such as hydroquinone. The recent application of such staining technology includes the enzyme-mediated formation of silver nanoparticles.[16-19] AP can produce metallic silver by dephosphorylation of a substrate (e.g., L-ascorbic-2-phosphate,[19] *p*-aminophenyl phosphate,[20] and 3-indoxyl phosphate[21]) that acts as a reducing agent.

In this chapter, we report the first use of enzymes to synthesize an insoluble magnetic material that might prove useful in biosensing and also in materials synthesis. In our system, AP catalyzes the dephosphorylation of L-ascorbic-2-phosphate, which then serves as a reducing agent for iron, gadolinium, and holmium chlorides to yield paramagnetic MNPs at room temperature. Our strategy offers a novel approach to magnetic sensing in which the magnetic reporter can be enzymatically synthesized in situ, and demonstrates for the first time the enzymatic synthesis of (weakly) magnetic materials. This approach is inexpensive and circumvents the substantial mass-transfer concerns associated with pre-synthesized magnetic reporter particles while preserving the advantages of magnetic sensing,

including the use of inexpensive solid-state detectors and the elimination of optical sensing challenges.

5.2 Materials and Methods

The chemicals used in the syntheses outlined below were of analytical grade and were used as received from the supplier without further purification. Millipore water (resistivity of >18 MΩ-cm) from a Milli-Q water system was used in the synthesis and washing steps.

5.2.1 Preliminary Experiments of Reduction of Different Metal Salts Using L-ascorbic Acid

In initial efforts to obtain Fe-Gd-O and Fe-Ho-O precipitates through enzymatic means, we first explored the chemical reduction of ferric chloride, ferric nitrate, cobalt nitrate, nickel sulfate, platinic acid, and copper sulfate. In each experiment, 0.1 to 2.0 mmol of the salt were dissolved in 5 mL Millipore water and evaluated to determine whether a magnetic precipitate was formed upon the addition of L-ascorbic acid. Using this reduction procedure, we obtained precipitates under various experimental conditions of pH (from 6 to 10), temperature (4 °C, 20 °C, 37 °C), and magnetic field conditions during synthesis (presence or absence of a strong bar magnet).

5.2.2 Synthesis of $Fe_xGd_yO_z$ and $Fe_xHo_yO_z$ Nanoparticles

Ascorbic acid (aa) was used either as purchased ("chemical synthesis" approach) or was produced enzymatically via dephosphorylation of L-ascorbic

acid 2-phosphate sesquimagnesium salt hydrate (p-aa) by alkaline phosphatase (AP) ("enzymatic synthesis" approach). Samples of AP were obtained from Sigma (catalog # P6774; 0.049 ml; 3531 units/mg protein and 13 mg protein/ml). One unit activity of AP is defined to hydrolyze 1 μmole of substrate (4-nitrophenyl phosphate) per minute at pH 9.8 at 37 °C. Zeba desalting columns (7K MWCO from Thermo Fisher Scientific) were used to remove more than 95% (column specification) of the salts (5 mM $MgCl_2$ and 0.2 mM $ZnCl_2$) present in the AP solution. The enzyme was then resuspended in 100 μL diethanolamine buffer (pH 9.8) containing 5 mM $MgNO_3$ and 0.25 mM $ZnNO_3$ to give a final concentration of 60 units AP/mL. In a 50-mL centrifuge tube, 0.16 g (0.60 mmol) of $FeCl_3.6H_2O$ and 0.05 g (0.10 mmol) $GdCl_3.6H_2O$ were dissolved in 5 mL of Millipore water. For chemical or enzymatic synthesis of $Fe_xGd_yO_z$, 0.1 g (0.6 mmol) of aa or 0.1 g (0.3 mmol) of p-aa, respectively, were added to the salt solution. In case of enzymatic synthesis, 15 μL of 60 units/mL AP enzyme to the centrifuge tube containing the metal salts. For the synthesis of $Fe_xHo_yO_z$, we used a similar procedure with 0.16 g (0.6 mmol) of $FeCl_3.6H_2O$, 0.05 g (0.1 mmol) of $HoCl_3.6H_2O$, 0.1 g (0.6 mmol) of aa (chemical synthesis) or 0.1 g (0.3 mmol) of p-aa (enzymatic synthesis), and 15 μL of 60 units/mL AP enzyme (enzymatic synthesis). The synthesis was carried out at 20 °C.

5.2.3 Characterization of Nanoparticles by SEM, TEM, XRD, EDX, and VSM

Nanoparticles were characterized by transmission electron microscopy (TEM; JEOL-2000 FX operating at 200 kV and equipped with energy dispersive

spectrometer; EDX), scanning electron microscopy (SEM; LEO-1525 operating at 15 kV), vibrating sample magnetometry (VSM PPMS, Quantum Design EverCool II), and X-ray diffraction (XRD; Siemens D5000 X-ray diffractometer). For the TEM analyses, we deposited the nanoparticles suspended in ethanol on a holey carbon film coating a 300-mesh copper grid and allowed to dry. For the SEM analyses, we deposited them on a silicon wafer and allowed them to dry. We used EDX, XRD, and SAED (selected area electron diffraction, a TEM crystallographic technique) to confirm the composition and phases of the nanoparticles. For the latter studies, a concentrated sample of nanoparticles in ethanol was deposited on a piranha-cleaned glass slide, and XRD was carried out using Cu Kα radiation ($\lambda = 1.540562$ Å) in the 2θ range from 0 to 90°.

The magnetic properties (saturation magnetization, residual magnetization, coercivity, and blocking temperature) of a known mass of sample were measured using VSM. Saturation magnetization and coercivity were obtained from the hysteresis loop analysis at 300 K and at 5 K. Measurements were recorded with uniform spacing in log field by sweeping the field 100 Oe/sec with a maximum applied field up to ±90 kOe. Zero-field-cooling (ZFC) and field-cooling (FC) magnetization curves were measured in the temperature range of 1.9-300 K using a field of 100 Oe. Data were obtained by first cooling the sample from 300 K to 1.9 K without applying any magnetic field. To obtain the ZFC curve, a small field of 100 Oe was applied after reaching 1.9 K, and the magnetization was measured at 0.5 K intervals while heating the sample to 300 K with a heating rate of 2 K/min.

The FC curve was obtained by cooling the sample from 300 K to 1.9 K while keeping the same applied field.

5.3 Results and Discussion

In nature, magnetotactic bacteria[22] possessing specialized organelles (magnetosomes) have the ability to synthesize ferrimagnetic crystals of either magnetite (Fe_3O_4) or the iron sulfide greigite (Fe_3S_4). However, translating this natural synthesis approach to the bench has been challenging, since these bacteria are difficult to culture in the laboratory and the synthesis of these magnetic particles is encoded by at least 28 different genes.[23]

SEM and TEM images of the chemically and enzymatically synthesized MNPs are shown in Figures 5.1 and 5.2, respectively. The chemically synthesized nanoparticles were found to be $Fe_{43\pm18}Gd_{2\pm0}O_{55\pm18}$ and $Fe_{3\pm1}Ho_{11\pm2}O_{85\pm3}$, while the enzymatically synthesized nanoparticles were composed of $Fe_{45\pm14}Gd_{5\pm2}O_{50\pm15}$ and $Fe_{42\pm4}Ho_{6\pm4}O_{52\pm5}$.

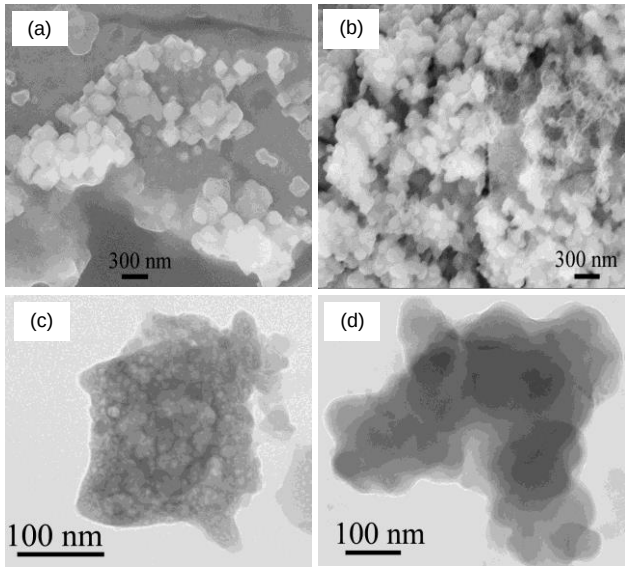

Figure 5.1 Images of chemically synthesized magnetic nanoparticles: (a) Fe-Gd-O SEM, (b) Fe-Ho-O SEM, (c) Fe-Gd-O TEM, and (d) Fe-Ho-O TEM.

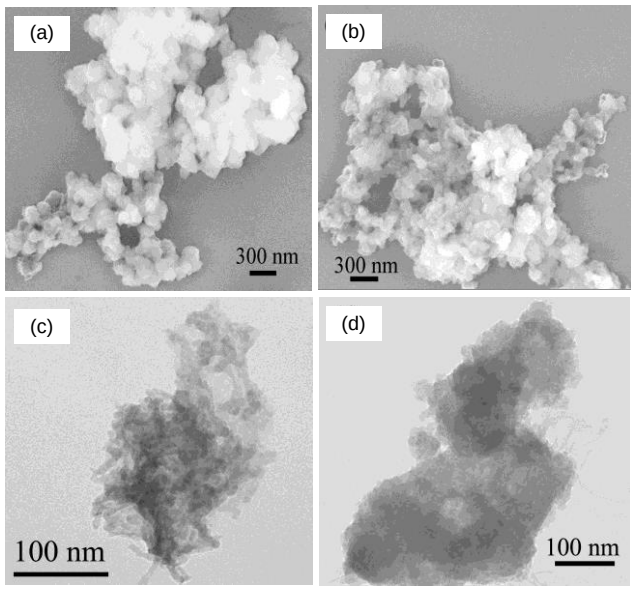

Figure 5.2 Images of enzymatically synthesized magnetic nanoparticles: (a) Fe-Gd-O SEM, (b) Fe-Ho-O SEM, (c) Fe-Gd-O TEM and (d) Fe-Ho-O.

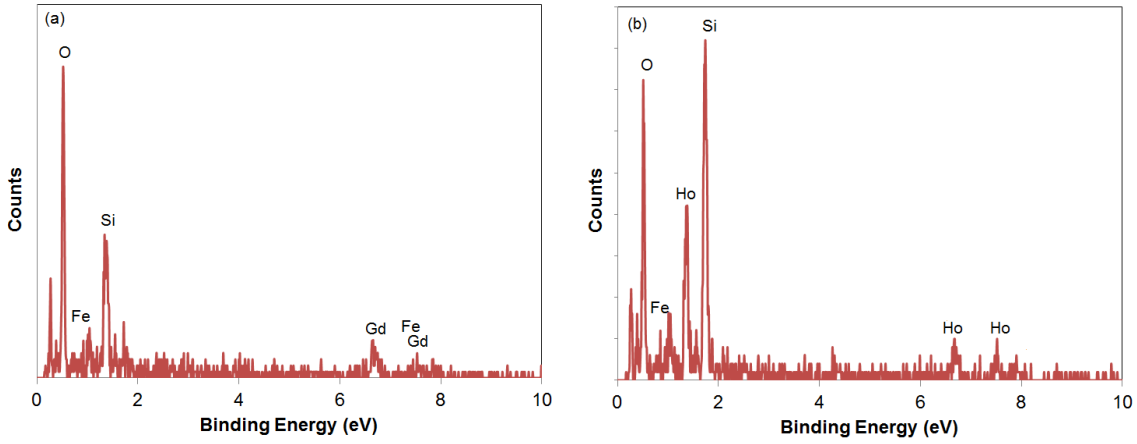

Figure 5.3 SEM/EDX of the chemically synthesized (a) $Fe_{43\pm18}Gd_{2\pm0}O_{55\pm18}$ and (b) $Fe_{3\pm1}Ho_{11\pm2}O_{85\pm3}$ magnetic nanoparticles.

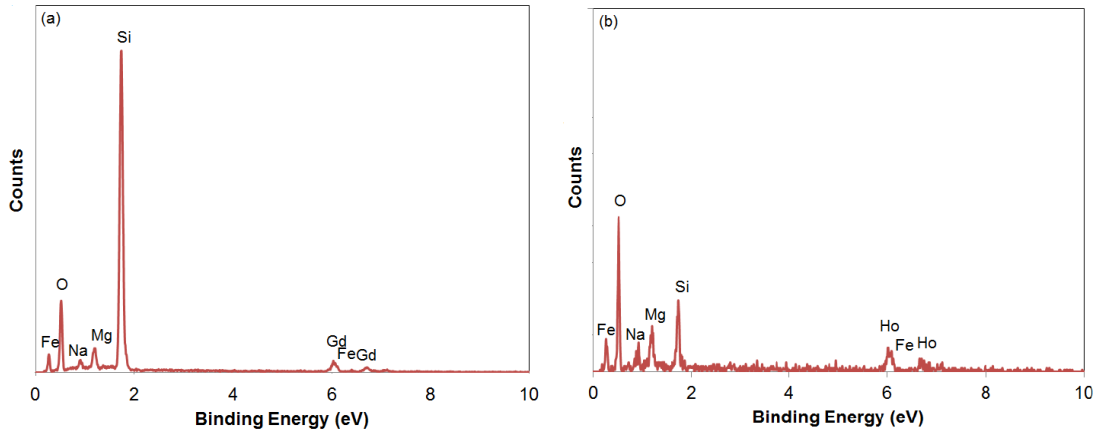

Figure 5.4 SEM/EDX of the enzymatically synthesized (a) $Fe_{45\pm14}Gd_{5\pm2}O_{50\pm15}$ and (b) $Fe_{42\pm4}Ho_{6\pm4}O_{52\pm5}$ magnetic nanoparticles.

SEM/EDX was used to obtain the composition of the chemically and enzymatically synthesized Fe-Gd-O and Fe-Ho-O precipitates to be $Fe_{45\pm14}Gd_{5\pm2}O_{50\pm15}$ and 90 mg $Fe_{42\pm4}Ho_{6\pm4}O_{52\pm5}$. Each SEM/EDX spectrum is an average of over 5 samplings and the average composition with standard deviation was calculated using at least 3 spectra for each sample. An example of the spectrum obtained for each precipitate is given in Figures 5.3 and 5.4.

Using TEM/EDX, we were able to further analyze the composition of each nanoparticle. We analyzed 5-15 nanoparticles and plotted the atomic % of Fe, Gd, and O or Fe, Ho, and O in each nanoparticle on an x-y-z graph to evaluate if there was a dominant composition cluster area. Figures 5.5 and 5.6 provide the analyses of the Fe-Gd-O and Fe-Ho-O magnetic nanoparticles synthesized chemically (Figure 5.5) and enzymatically (Figure 5.6).

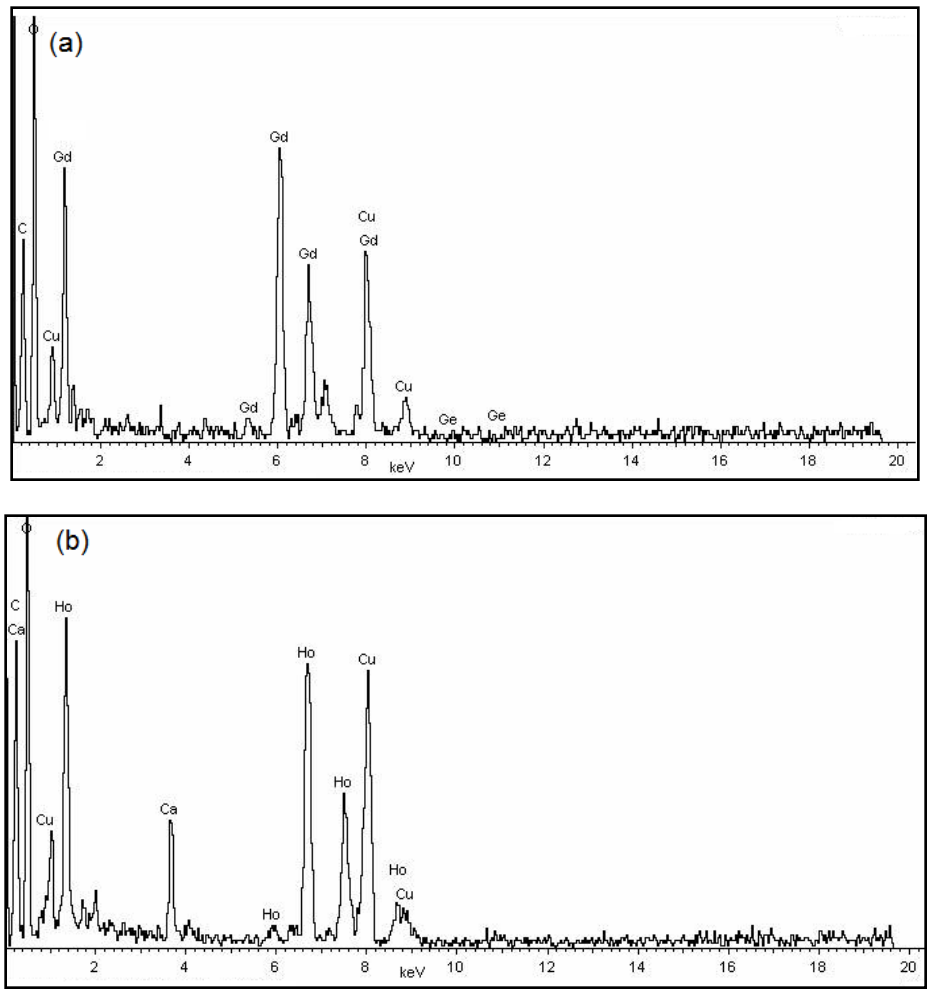

Figure 5.5 TEM/EDX of the chemically synthesized (a) Fe-Gd-O and (b) Fe-Ho-O magnetic nanoparticles.

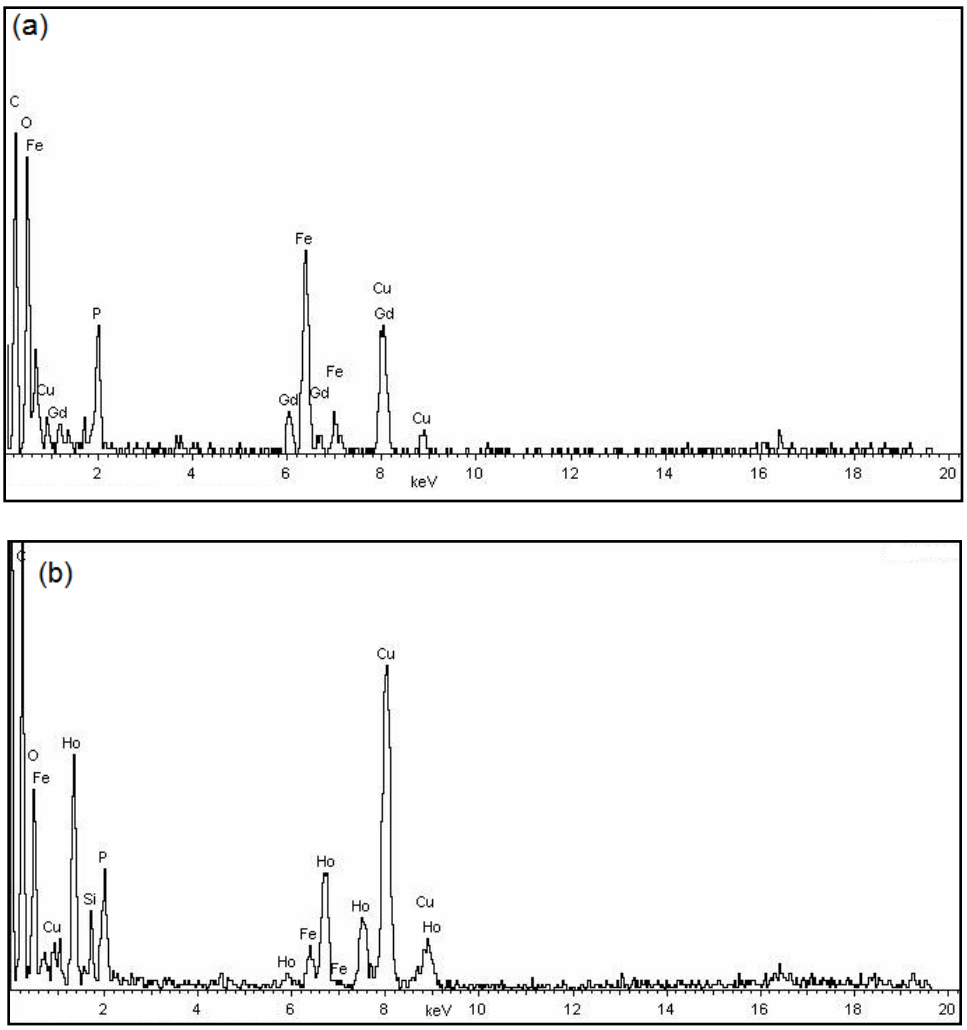

Figure 5.6 TEM/EDX of the enzymatically synthesized (a) Fe-Gd-O and (b) Fe-Ho-O magnetic nanoparticles.

The deviation of x, y, and z for $Fe_xGd_yO_z$ and $Fe_xHo_yO_z$ produced by the two procedures (chemical and enzymatic) might be a reflection of a variation in composition for the individual particles as observed in the TEM/EDX data discussed below. The TEM diffraction data showed that in each sample, some of the nanoparticles were crystalline and some were amorphous (data not shown). The diffraction patterns gathered by the TEM showed a crystalline selected area electron diffraction (SAED) that pointed to the presence of FeO in some and matched CaO in some nanostructures; the rest of the nanoparticles in each sample revealed amorphous SAED patterns. The varied diffraction

patterns observed in each sample indicated that the samples were inhomogeneous with respect to composition, which led us to study the composition of these nanoparticles further. To accomplish this task, we isolated about 15 particles of each of the chemically and enzymatically synthesized Fe-Gd-O and the enzymatically synthesized Fe-Ho-O, and 5 particles of chemically synthesized Fe-Ho-O. Figure 5.7 gives the clusters of compositions found in the 4 samples using an x, y, z scatter plot. The graphic shows that out of the chemically synthesized nanoparticles analyzed, most of them cluster around single-element oxides, and there are only a few nanoparticles that consist of all three elements (Fe, Gd, O or Fe, Ho, O). Additionally, none of the chemically synthesized nanoparticles contained all three components (Fe, Gd, and O or Fe, Ho, and O). However, in the case of the enzymatically synthesized nanoparticles, although not a major population, some of the particles contained all three elements, suggesting increased synthetic potential of the enzymatic approach.

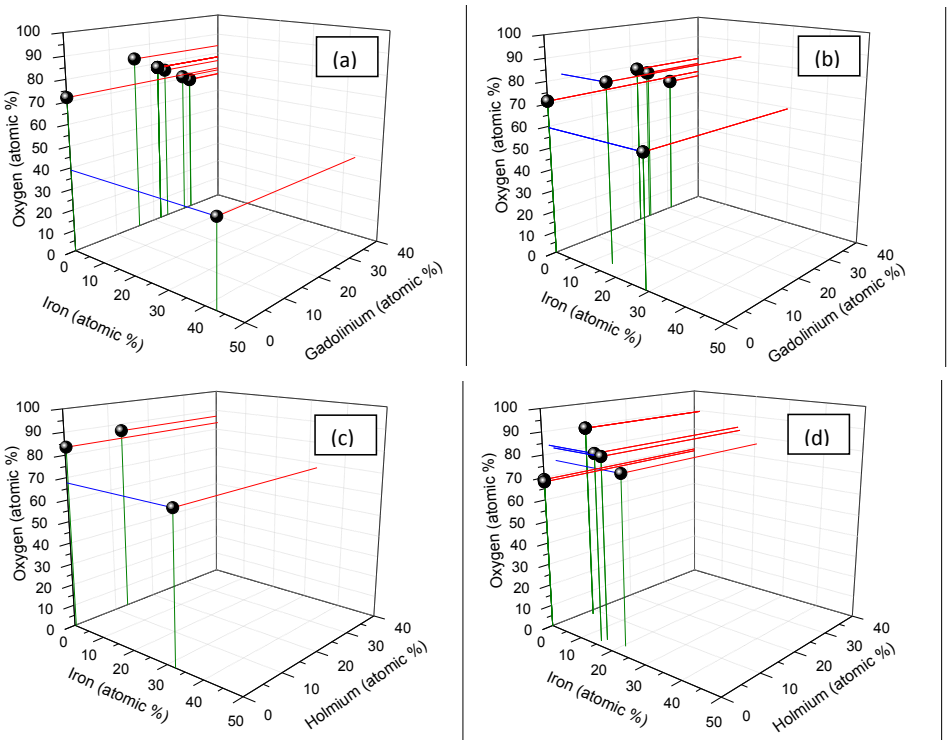

Figure 5.7 Composition of the nanoparticles using TEM-EDX for (a) the chemically synthesized Fe-Gd-O, (b) the enzymatically synthesized Fe-Gd-O, (c) the chemically synthesized Fe-Ho-O, and (d) the enzymatically synthesized Fe-Ho-O.

Elemental mass balances on the synthetic process were estimated. An aliquot of 80 µg of 0.9 units of AP protein gave magnetic precipitates of 80 mg $Fe_{45\pm14}Gd_{5\pm2}O_{50\pm15}$ and 90 mg $Fe_{42\pm4}Ho_{6\pm4}O_{52\pm5}$ (i.e., 1 µg protein used for ~1 mg NP synthesized). Based on the EDX data, the weight % ratio of Fe:Gd and Fe:Ho was 59 ± 14 : 20 ± 2 and 57 ± 9 : 23 ± 12, respectively. The initial mass of Fe, Gd, Ho was 0.04 g, 0.02 g, and 0.02 g. Taking a mass balance with respect to iron, gadolinium, and holmium, recovery was estimated at 118 ± 28% and 80 ± 8% for Fe and Gd in the Fe-Gd-O precipitate and 128 ± 20% and 100 ± 54% for Fe and Ho in Fe-Ho-O, where the non-homogeneous composition likely led to significant deviations in the recovery.

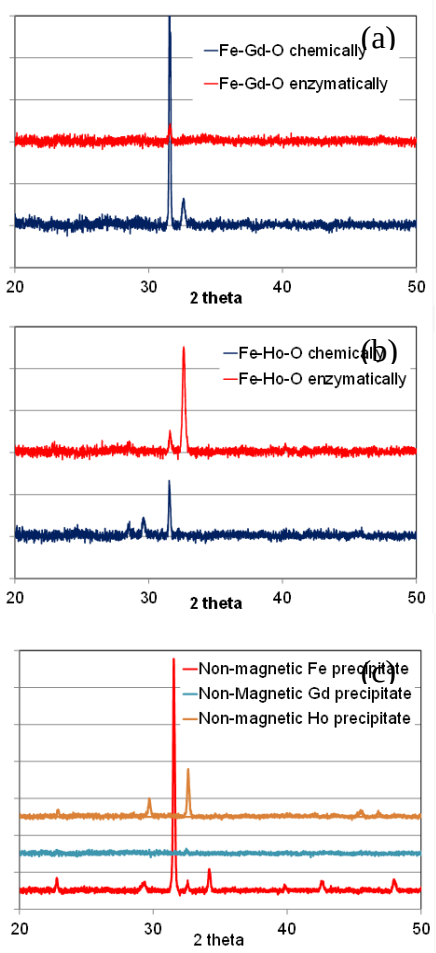

Figure 5.8 XRD patterns of (a) the Fe-Gd-O MNPs, (b) the Fe-Ho-O MNPs, and (c) the non-magnetic precipitates obtained by reduction of the chlorides of iron, gadolinium, and holmium.

Figure 5.8 compares the XRD patterns of the chemically and enzymatically synthesized Fe-Gd-O and Fe-Ho-O nanoparticles, respectively. These XRD patterns fail to match any of the XRD patterns of the existing Fe-Gd-O and Fe-Ho-O compounds in the Inorganic Crystal Structure Database (ICSD). As noted above, the reduction of the individual iron, gadolinium, and holmium salts using L-ascorbic acid failed to yield magnetic precipitates. However, we characterized the non-magnetic precipitate using XRD and compared it to the magnetic precipitate, as shown in Figure 5.8. Comparison of

the XRD patterns confirm that the magnetic precipitate obtained by using gadolinium and holmium as dopants is distinctly different from the non-magnetic precipitate obtained via reduction of the individual salts.

The nanoparticles were characterized using VSM and the magnetization curves at 300 K for chemically synthesized and enzymatically synthesized nanoparticles are shown in Figure 5.9. In all these cases, the particles exhibit paramagnetic behavior, since the magnetization increases linearly with increasing magnetic field. At low temperature, 5 K, the nanoparticles maintained strong magnetic behavior (Figure 5.10) and exhibited a significantly higher saturation magnetization of 45 and 30 emu/g for $Fe_{45\pm14}Gd_{5\pm2}O_{50\pm15}$ and $Fe_{42\pm4}Ho_{6\pm4}O_{52\pm5}$, respectively, for enzymatically synthesized particles and of 100 and 50 emu/g for $Fe_{45\pm14}Gd_{5\pm2}O_{50\pm15}$ and $Fe_{42\pm4}Ho_{6\pm4}O_{52\pm5}$, respectively, for chemically synthesized particles.

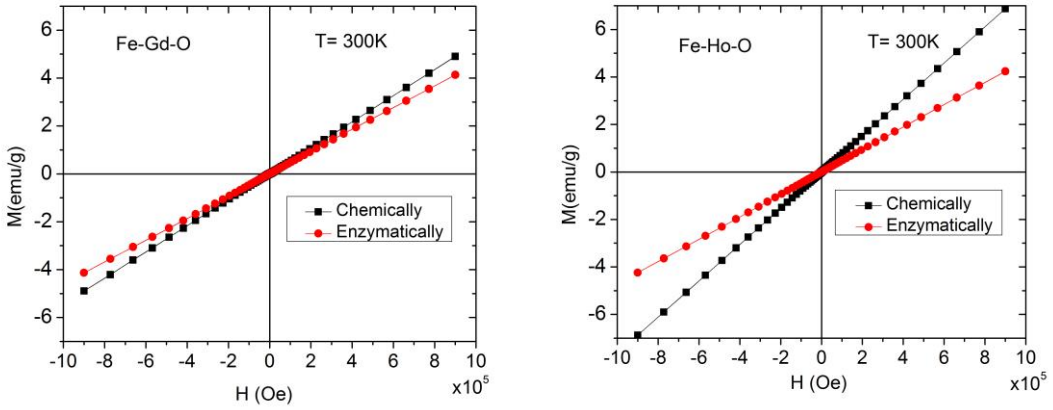

Figure 5.9 Magnetization curves recorded at 300 K for (a) the chemically synthesized $Fe_{45\pm14}Gd_{5\pm2}O_{50\pm15}$ MNPs and the enzymatically synthesized $Fe_{43\pm18}Gd_{2\pm0}O_{55\pm18}$ MNPs and (b) the chemically synthesized $Fe_{42\pm4}Ho_{6\pm4}O_{52\pm5}$ MNPs and the enzymatically synthesized $Fe_{3\pm1}Ho_{11\pm2}O_{85\pm3}$ MNPs.

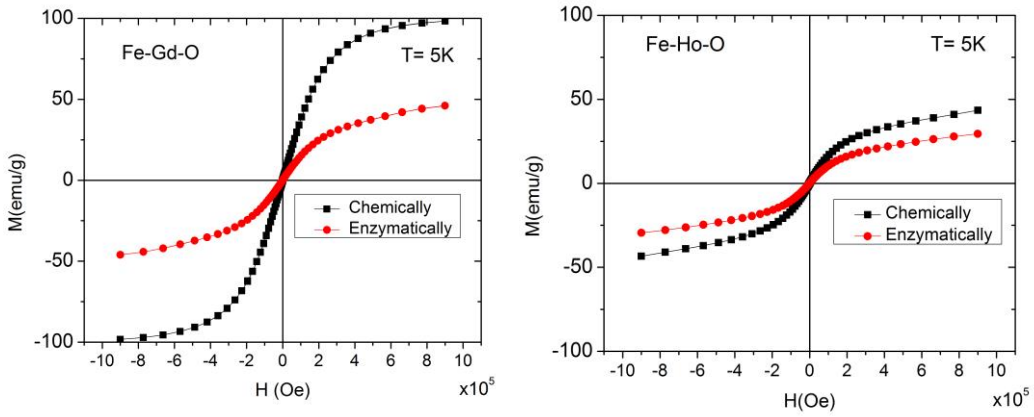

Figure 5.10 Magnetization curves recorded at 5 K for (a) the chemically synthesized $Fe_{43\pm18}Gd_{2\pm0}O_{55\pm18}$ MNPs and the enzymatically synthesized $Fe_{45\pm14}Gd_{5\pm2}O_{50\pm15}$ MNPs and (b) the chemically synthesized $Fe_{3\pm1}Ho_{11\pm2}O_{85\pm3}$ MNPs and the enzymatically synthesized $Fe_{42\pm4}Ho_{6\pm4}O_{52\pm5}$ MNPs.

As shown in Figure 5.11, as the temperature decreases from 300 K to 1.9 K, the magnetic behavior of the nanoparticles transforms from paramagnetic to antiferromagnetic with a Néel temperature around 15-25 K.

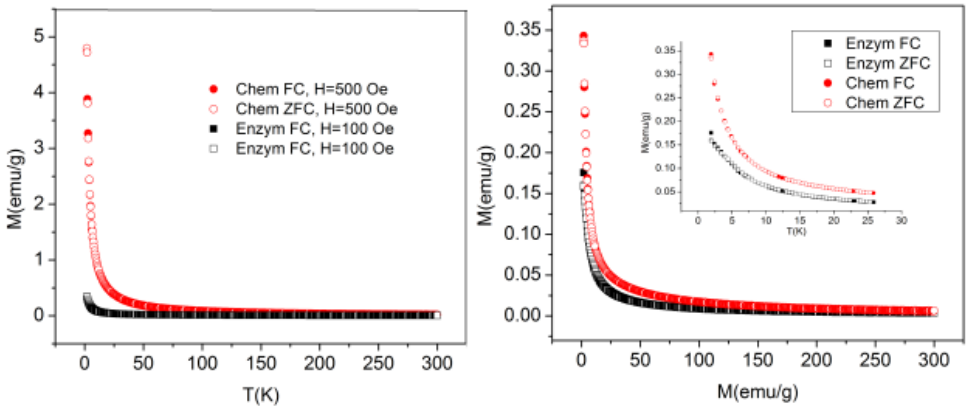

Figure 5.11 Zero Field Cooling (ZFC, open symbols) and Field Cooling (FC, solid symbols) curves for Fe-Gd-O and Fe-Ho-O systems. Inset: maximum magnetization 4.8 emu/g of nanoparticles.

The introduction of dopants during the chemical synthesis of MNPs has been previously demonstrated.[24-26] Johnson *et al.* found that ZnO nanoparticles lacking a

doping metal exhibited weak or no magnetic properties, but when Fe was used as a dopant, the resultant $Zn_{1-x}Fe_xO$ product showed noticeable levels of magnetization that increased as Fe was increased from 0 to 10%.[25] During our screening experiments, we observed that 6:1 molar ratio mixtures of ferric chloride and either gadolinium chloride or holmium chloride gave precipitates that were attracted to a bar magnet. We then enzymatically converted L-ascorbic-2-phosphate to L-ascorbic acid and found it could serve as a reducing agent for iron, gadolinium, and holmium salts. The resultant precipitates were magnetic. In our novel enzymatic process, gadolinium and holmium are incorporated in the products as dopants, producing measurable magnetic properties as compared to the non-magnetic iron oxide precipitate formed in the absence of these dopants.

On doping with the rare earth elements Gd and Ho, the resultant enzymatically-synthesized nanoparticles were found to be weakly magnetic (~5 emu/g) at 300 K, but with a comparatively higher saturation magnetization of 45 emu/g for $Fe_{45\pm14}Gd_{5\pm2}O_{50\pm15}$ and 30 emu/g for $Fe_{42\pm4}Ho_{6\pm4}O_{52\pm5}$ at 5 K. Both chemically and enzymatically synthesized MNPs, were observed to be paramagnetic at 300 K and antiferromagnetic under 25 K. Although Gd and Ho possess a higher number of unpaired f electrons as compared to the unpaired d electrons in Fe, enhancement of the magnetic properties by the coupling of these electrons is observed only at low temperature.

The saturation magnetization of the samples synthesized might be reduced by the significant presence of non-magnetic precipitates of single-element oxides (as noted earlier, the reduction of individual salts failed to form a magnetic precipitate) with only a small percentage of the MNPs of Fe-Gd-O or Fe-Ho-O present. As previously reported

in the case of $LnFeO_3$ (Ln=rare earth), phase-selective or homogeneous composition is difficult to achieve even during chemical syntheses. The hydrothermal and co-precipitation synthesis of $GdFeO_3$ gave an amorphous precipitate, and the combustion route yielded a crystalline powder.[27,28] In another study, the reactant ratios were varied to obtain mono-phasic $HoFeO_3$.[29] Further, a recent hydrothermal synthesis optimized the process conditions (alkalinity, reaction temperature, and reaction time) to afford pure phases of $GdFeO_3$ and $HoFeO_3$; however, they exhibited a weak magnetization of 0.03 emu/g and 0.3 emu/g, respectively.[30] In all of these syntheses, consistent with the chemically and enzymatically synthesized nanoparticles described in this chapter, the nanoparticles were paramagnetic at room temperature and antiferromagnetic at low temperature. Importantly, the room-temperature magnetization of the nanoparticles described here is significantly greater than that of analogous chemically synthesized $Ln_xFe_yO_z$ (Ln = Gd, Ho) samples reported previously.[27-29]

5.4 Conclusions

In summary, we have demonstrated a novel alternative to optical/electrochemical reporters by enzymatically synthesizing MNPs with higher saturation magnetization than similar nanoparticles ($LnFeO_3$ (Ln = Gd, Ho)) synthesized by other routes. This first *in vitro* enzymatic synthesis of magnetic nanoparticles opens a novel approach to magnetic sensing in which the magnetic reporter is enzymatically synthesized *in situ* thus circumventing any mass-transfer limitations. The enzymatically synthesized nanoparticles, paramagnetic at 300 K and antiferromagnetic below 25 K, exhibited a strong saturation magnetization, up

to 45 emu/g at 5K. Optimization of reaction conditions could lead to a homogeneous composition that eliminates/reduces the non-magnetic components. With further optimization of the process parameters, the precipitated particles can be readily integrated with GMR sensors as the one in-house with a reported sensitivity of 10^{-13} emu.[2,31,32]

5.5 References

(1) Mani, V.; Chikkaveeraiah, B. V. *Expert Opinion on Medical Diagnostics* **2011**, *5*, 381-391

(2) Baselt, D. R.; Lee, G. U.; Natesan, M.; Metzger, S. W.; Sheehan, P. E.; Colton, R. J. *Biosens. Bioelectron.* **1998**, *13*, 731-739.

(3) Shieh, R.; Ackley, D. E. U.S. Pat. No. 6,057,167, **1996**.

(4) Li, Y.; Srinivasan, B.; Jing, Y.; Yao, X.; Hugger, M. A.; Wang, J. P.; Xing, C. *J. Am. Chem. Soc.* **2010**, *132*, 4388-4392.

(5) Srinivasan, B.; Li, Y.; Jing, Y.; Xu, Y.-H.; Yao, X.; Xing, C.; Wang, J.-P. *Angew. Chem., Int. Ed.* **2009**, *48*, 2764-2767.

(6) Srinivasan, B.; Li, Y.; Jing, Y.; Xing, C.; Slaton, J.; Wang, J.-P. *Anal. Chem.* **2011**, *83*, 2996-3002.

(7) Hall, D. A.; Gaster, R. S.; Lin, T.; Osterfeld, S. J.; Han, S.; Murmann, B.; Wang, S. X. *Biosens. Bioelectron.* **2010**, *25*, 2051-2057.

(8) Osterfeld, S. J.; Yu, H.; Gaster, R. S.; Caramuta, S.; Xu, L.; Han, S. J.; Hall, D. A.; Wilson, R. J.; Sun, S.; White, R. L.; Davis, R. W.; Pourmand, N.; Wang, S. X. *Proc. Natl. Acad. Sci.* **2008**, *105*, 20637-20640.

(9) Hall, D. A.; Wang, S. X.; Murmann, B.; Gaster, R. S. *Conf. Proc. (Midwest Symp Circuits Syst.)* **2010**, 1779-1782.

(10) Gaster, R. S.; Hall, D. A.; Nielsen, C. H.; Osterfeld, S. J.; Yu, H.; Mach, K. E.; Wilson, R. J.; Murmann, B.; Liao, J. C.; Gambhir, S. S.; Wang, S. X. *Nature Medicine* **2009**, *15*, 1327-1332.

(11) Xu, L.; Yu, H.; Akhras, M. S.; Han, S.-J.; Osterfeld, S.; White, R. L.; Pourmand, N.; Wang, S. X. *Biosens. Bioelectron.* **2008**, *24*, 99-103.

(12) Orlov, A. V.; Khodakova, J. A.; Nikitin, M. P.; Shepelyakovskaya, A. O.; Brovko, F. A.; Laman, A. G.; Grishin, E. V.; Nikitin, P. I. *Anal. Chem.* **2013**, *85*, 1154-1163.

(13) Peck, R. B.; Schweizer, J.; Weigl, B. H.; Somoza, C.; Silver, J.; Sellors, J. W.; Lu, P. S. *Clin. Chem.* **2006**, *52*, 2170-2172.

(14) Eadie, M. J.; Tyrer, J. H.; Kukums, J. R.; Hooper, W. D. *Histochemie* **1970**, *21*, 170-180.

(15) Altman, F. P. *Histochemie* **1974**, *38*, 155-171.

(16) Cacao, E. E.; Nasrullah, A.; Sherlock, T.; Kemper, S.; Kourentzi, K.; Ruchhoeft, P.; Stein, G. E.; Willson, R. C. *PLoS One* **2013**, *8*, e56835.

(17) Hacker, G.W.; Graf, A.H.; Hauser-Kronberger, C.; Wirnsberger, G.; Schiechl, A.; Bernatzky, G.; Wittauer, U.; Su, H.; Adam, H.; Thurner, J.; Danscher, G.; Grimelius, L. *Chinese Med. J.* **1993**, *106*, 83-92.

(18) Hainfeld, J.F.; Liu, W. WO2008109617, 2008.

(19) Cacao, E.E. PhD Dissertation, University of Houston, Houston, TX, 2012.

(20) Wu, J.; Chumbimuni-Torres, K. Y.; Galik, M.; Thammakhet, C.; Haake, D. A.; Wang, J. *Anal. Chem.* **2009**, *81*, 10007-10012.

(21) Fanjul-Bolado, P.; Hernandez-Santos, D.; Gonzalez-Garcia, M. B.; Costa-Garcia, A. *Anal. Chem.* **2007**, *79*, 5272-5277.

(22) Blakemore, R. *Science* **1975**, *190*, 377-379.

(23) Schuler, D. *FEMS Microbiology Reviews* **2008**, *32*, 654-672.

(24) Dohcevic-Mitrovic, Z. D.; Paunovic, N.; Radovic, M.; Popovic, Z. V.; Matovic, B.; Cekic, B.; Ivanovski, V. *Appl. Phys. Lett.* **2010**, *96*, 203104/203101-203104/203103.

(25) Johnson, L. M.; Thurber, A.; Anghel, J.; Sabetian, M.; Engelhard, M. H.; Tenne, D. A.; Hanna, C. B.; Punnoose, A. *Phys. Rev. B: Condens. Matter Mater. Phys.* **2010**, *82*, 054419/054411-054419/054415.

(26) Pool, V. L.; Klem, M. T.; Chorney, C. L.; Arenholz, E. A.; Idzerda, Y. U. *J. Appl. Phys.* **2011**, *109*, 07B529/521-507B529/523.

(27) Bedekar, V.; Jayakumar, O. D.; Manjanna, J.; Tyagi, A. K. *Mater. Lett.* **2008**, *62*, 3793-3795.

(28) Zhang, Y.; Zheng, A.; Yang, X.; He, H.; Fan, Y.; Yao, C. *CrystEngComm* **2012**, *14*, 8432-8439.

(29) Jiang, L.; Liu, W.; Wu, A.; Xu, J.; Liu, Q.; Qian, G.; Zhang, H. *Ceram. Int.* **2012**, *38*, 3667-3672.

(30) Zhou, Z.; Guo, L.; Yang, H.; Liu, Q.; Ye, F. *J. Alloys Compd.* **2014**, *583*, 21-31.

(31) Kolhatkar, A. G.; Nekrashevich, I.; Litvinov, D.; Willson, R. C.; Lee, T. R. *Chem. Mater.* **2013**, *25*, 1092-1097.

(32) Wirix-Speetjens, R.; Reekmans, G.; De, P. R.; Liu, C.; Laureyn, W.; Borghs, G. *Sens. Actuators, B* **2007**, *128*, 1-4.

Chapter 6

Dissertation Summary and Future Work

6.1 Dissertation Summary

The tremendous interest in magnetic nanoparticles (MNPs) is reflected in published research that ranges from novel methods of synthesis of unique nanoparticle shapes and composite structures to a large number of MNP characterization techniques, and finally to their use in a variety of biomedical and nanotechnology-based applications. The knowledge gained from this vast body of research can be made more useful when it is summarized in a review format. In Chapter 1, I organized the published research results to correlate key magnetic properties with the parameters that influence them. Tuning these properties when synthesizing MNPs allows us to tailor nanoparticles for specific applications, thus increasing their effectiveness. The complex magnetic behavior exhibited by MNPs is governed by many factors; these factors can either improve or adversely affect the desired magnetic properties. In this chapter, I outlined a matrix of parameters that can be varied to tune MNP magnetic properties. For practical utility, Chapter 1 was limited to the effect of size, shape, composition, and shell-core structure on saturation magnetization, coercivity, blocking temperature, and relaxation time.

In the work described in Chapter 2, I systematically varied the reaction parameters in a liquid-phase reduction reaction and synthesized large FeCo nanocubes with body diagonal lengths of 175, 350, and 450 nm. The nanocubes were initially stabilized with poly(vinyl pyrrolidone) (PVP) and then coated with a relatively thin layer

of silica (~55 nm thick), while ensuring that they retained their cubic shape. The magnetization curves showed that the PVP-stabilized nanocubes exhibited a high saturation magnetization of 167 ± 4 emu/g. The saturation magnetization, however, decreased upon coating with silica to 146 ± 13 emu/g for the particles with 350 and 450 nm FeCo cores and 48 ± 1 emu/g for the particles with 175 nm FeCo cores. The silica-coated FeCo nanocubes were then functionalized with 3-(aminopropyl)-trimethoxysilane (APTMS), and a layer of surface-bound nanoparticles was generated by exposing the resultant amine-functionalized nanocubes to self-assembled monolayers (SAMs) on gold terminated with carboxylic-acid groups. This project is a component part of our effort to show how MNP shape can play an important role in the sensitivity of biosensors through an increase in the surface contact area of the MNP.

In the work described in Chapter 3, I synthesized Fe_3O_4 nanocubes and nanospheres having tunable body diagonals and diameters via solvothermal and thermal decomposition synthesis methods, respectively, and compared the magnetic properties of these two shapes. The dimensions of the spherical MNPs were tuned to obtain samples such that (i) the volume was equivalent to that of analogous cubic MNPs, or (ii) the diameter was equivalent to the body diagonal of analogous cubic MNPs. Vibrating sample magnetometry (VSM) was used to compare the magnetic properties of the synthesized spherical and cubic Fe_3O_4 MNPs on a same-volume and same-diameter/body diagonal basis. The saturation magnetization and coercivity of cubic MNPs is higher than that of spherical MNPs for nanoparticles ranging from ~100 to 225 nm for both the "same volume" basis and "same body diagonal/diameter". Higher saturation magnetization and higher

coercivity make the nanocubes more attractive for sensing and hyperthermia (where the heat generated varies with coercivity). However, the superior magnetic properties of the nanocubes could not be attributed to their shape alone. Data from TEM and EDX confirmed that the nanocubes were monocrystalline while the nanospheres were polycrystalline. The conclusion drawn from this analysis was that the degree of crystallinity is a significant contributor to the higher magnetization. Thus, this project demonstrated that shape and crystallinity are both important parameters that can be used to manipulate nanoscale magnetism in Fe_3O_4 MNPs to tailor them for a particular application.

Magnetic nanoparticles (MNPs) also have significant potential as labels for biomolecule detection due to the absence of magnetic background in biological samples. Based on the known enzymatic generation of L-ascorbic acid catalyzed by peroxidase or alkaline phosphatase (AP) followed by its use as a reducing agent, the work presented in Chapter 4 demonstrates the conversion of 100-nm Fe_3O_4 MNPs to non-magnetic precipitates using L-ascorbic acid formed by the AP-catalyzed dephosphorylation of phosphorylated L-ascorbic acid. The Fe_3O_4 MNPs and the resulting non-magnetic precipitate were characterized using scanning electron microscopy, energy-dispersive X-ray spectroscopy, and vibrating sample magnetometry. Conventional enzyme-linked immunosorbent assays (ELISA) using AP as the reporter rely on dephosphorylation of the substrate to form a product that can be detected by its absorbance, fluorescence, or luminescence. Our strategy offers a novel approach to magnetic sensing in which dephosphorylation of phosphorylated L-ascorbic acid by AP yields L-ascorbic acid that

converts magnetic Fe_3O_4 MNPs to a non-magnetic product *in situ* in the course of the assay, thus providing a "loss of signal" in the sensing device.

Chapter 5 reports the first *in vitro* enzymatic synthesis of paramagnetic and antiferromagnetic nanoparticles, toward magnetic ELISA reporting. Using this procedure, AP catalyzes the dephosphorylation of L-ascorbic-2-phosphate, which then serves as a reducing agent for salts of iron, gadolinium, and holmium, forming magnetic precipitates of $Fe_{45\pm14}Gd_{5\pm2}O_{50\pm15}$ and $Fe_{42\pm4}Ho_{6\pm4}O_{52\pm5}$. The MNPs contained in this precipitate were found to be paramagnetic at 300 K and antiferromagnetic under 25 K. Although weakly magnetic at 300 K, the room-temperature magnetization of the nanoparticles described here is significantly greater than that of analogous chemically-synthesized $Ln_xFe_yO_z$ (Ln=Gd, Ho) samples reported previously. At 5 K, for example, our samples showed a significantly higher saturation magnetization of 45 and 30 emu/g for $Fe_{45\pm14}Gd_{5\pm2}O_{50\pm15}$ and $Fe_{42\pm4}Ho_{6\pm4}O_{52\pm5}$, respectively. This example of *in vitro* enzymatic synthesis of magnetic nanoparticles is a novel approach to magnetic sensing; such *in situ* synthesis of magnetic labels might reduce cost and avoid mass-transfer concerns associated with pre-synthesized magnetic reporter particles.

6.2 Future Work

As with any research endeavor, there are always further studies that can be conducted that might help clarify or extend the initial results. Given the background and findings in Chapters 1 and 2, the research in Chapter 3 led to the conclusion that both shape and crystallinity influence the properties of magnetic nanoparticles. Additional studies that seek to obtain either polycrystalline cubes or

monocrystalline nanospheres are warranted to allow comparisons to be made on the basis of crystallinity alone.

With regard to Chapter 4, it would be useful to confirm "loss of signal" using a model system. The functionalized MNPs could be bound to the sensor to provide a baseline signal in the GMR sensor. On addition of the test fluid that contained the AP enzyme, the reducing agent would convert the MNPs to a non-magnetic precipitate that would reduce the resistance in the GMR sensor.

Finally, in Chapter 5 we demonstrated the enzymatic synthesis of weakly magnetic nanoparticles. Optimization of reaction conditions could lead to a homogeneous composition that eliminates/reduces the non-magnetic components, boosting the signal strength of the resulting MNPs. With further optimization of the process parameters, the precipitated particles can be readily integrated with GMR sensors such as the one developed in-house with a reported sensitivity of 10^{-13} emu.